主論文

Polarization transfer observables for proton inelastic scattering from ^{12}C at zero degrees

Atsushi Tamii

Doctoral Dissertation

Department of Physics

Kyoto University

September, 1999

Abstract

Polarization transfer (PT) observables in the $^{12}C(p,p')$ reaction at 0° for 392 MeV protons have been measured using a high resolution magnetic spectrometer *Grand Raiden*, and a newly constructed focal plane polarimeter (FPP).

The strength of the isoscalar spin-dependent interaction (V_σ) was experimentally deduced from the PT observables for the excitation of the 1^+, T=0 state. The obtained PT observables for excitation of the 0^+, T=0, the 1^+, T=0, and the 1^+, T=1 states are compared with the predictions of microscopic distorted wave impulse approximation calculations using the Franey and Love interaction and the Paris interactions. The strength of the isovector tensor, the isoscalar tensor, and the isoscalar spin-dependent interactions are studied.

It is demonstrated that the PT observables are powerful probes to study the spin-isospin structure of excitation strengths in the continuum region as well as discrete states. The excitation strengths are decomposed into the spin-flip and the non-spin-flip parts by using a quantity "total spin transfer" (Σ). The total spin transfer is defined by a linear combination of the PT observables. The ratio of the spin-flip strengths to the non-spin-flip strengths increase in the region above the giant resonances when the excitation energy increase. It is shown that the measured quantity S_{LL}-S_{SS} is sensitive to the isospin structure of spin-flip resonances and is useful to extract the isospin information of excitation strengths.

Contents

List of Tables

List of Figures

Chapter 1

INTRODUCTION

1.1 Nucleon-nucleus scattering at the intermediate energy region

Over the past decades nuclear reaction mechanism and nuclear structures have been extensively studied via nucleon-nucleus scattering in the intermediate energy region (100 $\leq E_p \leq$ 500 MeV). In this energy region, single-step processes are dominant and distortion effects are minimum since the isoscalar spin-independent interaction, which mainly contributes in the nucleon-nucleon (NN) scattering, is minimum (see V_0 in Fig. 1.1). Therefore, distorted wave impulse approximation (DWIA) provides a good base to describe nucleon-nucleus scattering.

In the recent high precision measurements of polarization phenomena in nucleon-nucleus reactions, two equipments are essential. One is a polarized ion source and the other is a polarimeter of reaction products. The polarized ion source provides highly polarized proton or deuteron beams with high intensity. Historically the first polarized ion source was developed in 1950's and has been continuously upgraded. The polarized ion source at the Research Center for Nuclear Physics (RCNP) provides proton beams up to 100 μA with a polarization of 70–80%.

As a polarimeter of the reaction products, the first prototype of a focal plane polarimeter was developed in the end of 1970's [1, 2]. By using the focal plane polarimeter,

polarization of the scattered particles can be measured with high efficiency from the scattering asymmetry at a scatterer target. Study of the spin-isospin degrees of freedom in nuclear system have been proceeded by using this equipment, at many facilities, *e.g.* LAMPF, TRIUMF, IUCF, RCNP, and RIKEN. In the 1980s, a focal plane polarimeter *MUSASHI* [3] was built for the spectrometer *DUMAS* [4] at the RCNP. The *MUSASHI* was dedicated for the measurement of the polarization of protons between 20 and 84 MeV by detecting the asymmetries during p+C elastic scattering. A new focal plane polarimeter (FPP) for *Grand Raiden* spectrometer has been developed for the study of reaction mechanism and spin-isospin excitations in nuclei in the intermediate energy region. The proton polarization is measured by detecting the asymmetries during p+C inclusive scattering, *i.e.* p+C elastic, inelastic, and quasi-free scatterings. A part of the system was constructed in 1993 and was tested by measuring spin rotation parameters for ^{58}Ni(p,p) elastic scattering at forward angles [5]. Now the total system has been completed. The FPP is capable of measuring the polarization of scattered protons with an efficiency of up to 5% and with an effective analyzing power of 0.2–0.5 depending on the proton energy (100–400 MeV). The overall FPP system was first used in the experiment of this work.

1.2 Properties of the NN interaction

The NN interaction has been studied via nucleon-nucleus scattering by using the new equipments. There are two types of approaches to construct the NN effective interaction. One is based on the phenomenological free NN scattering amplitudes (*e.g.* Franey and Love interaction), and the other is derived from the NN potentials based on meson-exchange model (*e.g.* Paris interaction). In both approaches, the effective interaction between the projectile (1) and the target nucleon (2) is described by the following form:

$$\begin{aligned} V_{12}(r) &= V_0(r) + V_\sigma(r)\boldsymbol{\sigma_1}\cdot\boldsymbol{\sigma_2} + V_\tau(r)\boldsymbol{\tau_1}\cdot\boldsymbol{\tau_2} + V_{\sigma\tau}(r)\boldsymbol{\sigma_1}\cdot\boldsymbol{\sigma_2}\boldsymbol{\tau_1}\cdot\boldsymbol{\tau_2} \\ &+ V_0^{LS}(r)\boldsymbol{L}\cdot(\boldsymbol{s_1}+\boldsymbol{s_2}) + V_\tau^{LS}(r)\boldsymbol{L}\cdot(\boldsymbol{s_1}+\boldsymbol{s_2})\boldsymbol{\tau_1}\cdot\boldsymbol{\tau_2} \\ &+ V_0^{rT}(r)S_{12} + V_\tau^{rT}(r)S_{12}\boldsymbol{\tau_1}\cdot\boldsymbol{\tau_2}\ , \end{aligned} \tag{1.1}$$

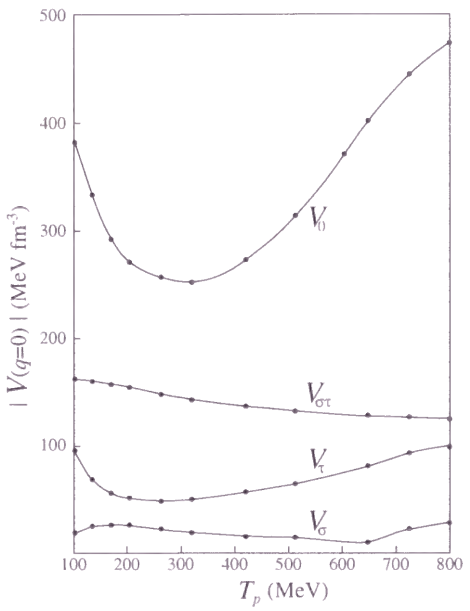

Figure 1.1: Energy dependence of the central NN interactions at the momentum transfer q=0 derived by Love *et al.* from Ref. 6.

where $\boldsymbol{L}$ is the relative angular momentum operator, S_{12} is the usual tensor operator written by

$$S_{12}(\boldsymbol{r}) \equiv 3\,\frac{(\boldsymbol{\sigma_1}\cdot\boldsymbol{r})(\boldsymbol{\sigma_2}\cdot\boldsymbol{r})}{\boldsymbol{r}^2} - (\boldsymbol{\sigma_1}\cdot\boldsymbol{\sigma_2})\ . \tag{1.2}$$

The interactions involving the spin operators, $\boldsymbol{\sigma_1}\cdot\boldsymbol{\sigma_2}$, $(\boldsymbol{s_1}+\boldsymbol{s_2})$, or S_{12}, mediate spin-flip (ΔS=1) transitions, and those involving the isospin operators $\boldsymbol{\tau_1}\cdot\boldsymbol{\tau_2}$ mediate isospin-flip (ΔT=1) transitions.

The central interactions of the free NN interaction deduced by Franey and Love (FL) are plotted in Fig. 1.1. The isoscalar spin-independent interaction (V_0) is dominating the isovector spin-dependent ($V_{\sigma\tau}$), the isovector spin-independent (V_τ), and the isoscalar spin-dependent (V_σ) interactions. In the intermediate energy region, V_0 becomes weak. Therefore, $V_{\sigma\tau}$ which mediates spin-isospin-flip transitions becomes relatively large, while V_τ is suppressed. V_σ is predicted to be quite weak at all energies.

The properties of V_0 has been studied by using proton elastic scattering [7, 8, 9, 10]. $V_{\sigma\tau}$ and V_τ have been investigated by (p,n) reactions [11, 12, 13, 14, 15] as describe in

the next section. Until now the strength of V_σ has not been well determined due to the lack of suitable probes.

1.3 Nucleon-nucleus scattering experiments at 0°

Among many experiments, observables at the scattering angle of 0° are very useful probes to study the nuclear reaction. In the 1980's, differential cross sections of (p, n) reactions at 0° were measured at the IUCF for various targets. The ratio of the cross sections between Gamow-Teller (GT) states and isobaric analog states was obtained [12, 13]. The transitions to the GT states (GT transition) and to the isobaric analog states (Fermi transition) are mediated by $V_{\sigma\tau}$ and V_τ, respectively. The interactions are related to the differential cross sections by the following simple equation [13]:

$$d\sigma_\alpha/d\Omega(q) = K_\alpha(E_p) \cdot N_\alpha(q) \cdot |J_\alpha(q)|^2 \cdot B(a, q) \ , \tag{1.3}$$

where K_α is a kinematical factor, N_α is a distortion factor, J_α is the Fourier transform of the NN interaction, $B(\alpha, q)$ is a nuclear structure factor, and a denotes the spin-isospin channel of the reaction. The strength ratio of $V_{\sigma\tau}$ and V_τ at the small momentum transfer region has been determined from the measured cross sections.

In addition to the differential cross sections, polarization transfer (PT) observables at 0° are useful to study the nuclear reaction. One of the PT observables, D_{NN}, for the excitation of the GT states via $(\vec{p}, \vec{n})$ reactions at 0° was measured for various targets [16, 17]. As is described in Sec. 1.4, plane wave impulse approximation (PWIA) calculations predict a D_{NN} value of $-\frac{1}{3}$ at 0° if the GT transition is mediated only by $V_{\sigma\tau}$. The deviation of the measured D_{NN} value from the prediction has been attributed to the contribution from the isovector tensor interaction (V_τ^T).

In parallel to the study of the (p, n) reactions, (p, p') measurements at very forward angles have been tried by many groups [18, 19, 20]. But it has taken a long time to succeed in measuring the (p, p') reactions at 0° because the scattered protons and the beam itself have nearly the same magnetic rigidity, and huge background particles come to

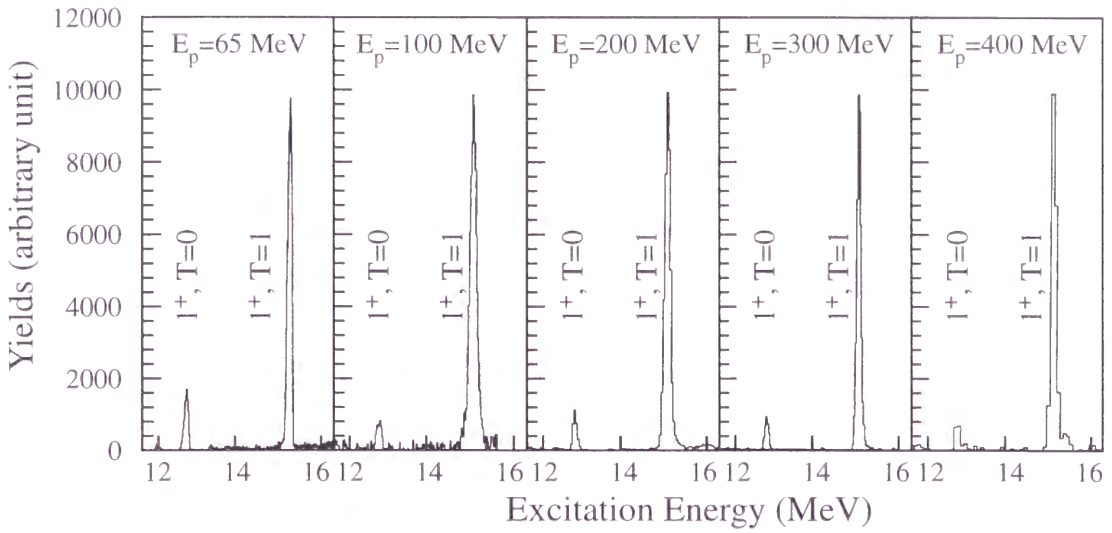

Figure 1.2: Excitation energy histogram in the ^{12}C(p,p') reaction at 0° from Ref. 21. Background events were subtracted assuming a flat distribution.

the counter system from the beam halo and the radiations from the beam stop. Recently our group have tuned an extremely low halo beam in a good stability, and have succeeded in measuring relative cross sections in the ^{12}C(p,p') reaction at 0° at the RCNP. The ratio of the cross sections for the excitation of the 1^+, T=0 state at 12.7 MeV to the 1^+, T=1 state at 15.1 MeV was obtained for incident proton energies of 65, 100, 200, 300, and 400 MeV (see Fig. 1.2 and 1.3). The 1^+, T=0 state is mainly excited by V_τ^T through knock-on exchange process, and the 1^+, T=1 state is mainly excited by $V_{\sigma\tau}$. The energy dependence of the strength of V_τ^T relative to that of $V_{\sigma\tau}$ was investigated [21]. The differential cross sections in (p,p') reactions at 0° have been also measured at the IUCF for an incident proton energy of 200 MeV [22, 23].

1.4 PT observables at 0° and the effective interaction

As a new probe to study the nuclear reaction mechanism and the nuclear structure, we have planned to measure the PT observables in (p,p') reactions at 0° by using the FPP system and the *Grand Raiden* spectrometer at the RCNP.

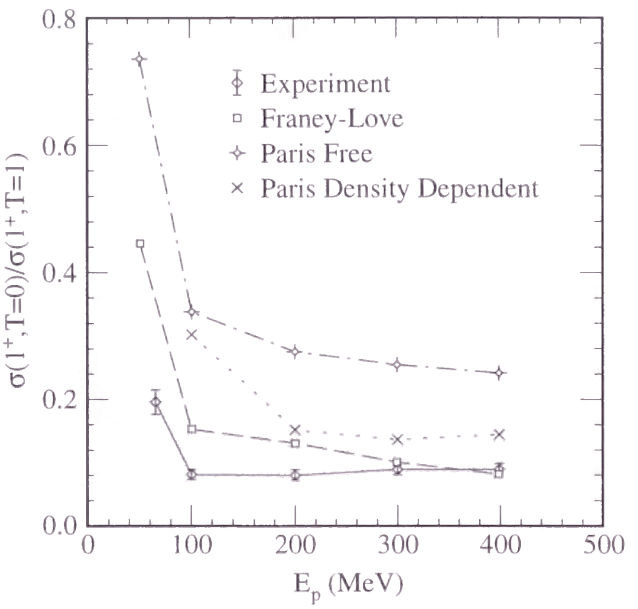

Figure 1.3: Measured ratio of the cross sections for the 1^+, T=0 state and the 1^+, T=1 state and DWIA calculations using various effective interactions. The figure is taken from Ref. 21.

We briefly consider in the PWIA the relation between the effective interactions and the PT observables for spin-flip transitions at 0°. The PWIA is expected to be a good starting point to describe the reaction mechanism for the present experiment, since single-step reactions are dominant in the nucleon-nucleus scattering at the intermediate energies, and distortion effects to the PT observables are small [24], especially at 0°.

In the following discussion, we assume a 0^+ ground state of an N=Z target nucleus (T_0=0) and consider spin-flip (ΔS=1) transitions via the (p, p') reaction. Transitions with small orbital angular momentum transfer (ΔL) are strongly enhanced at 0°. Therefore, the following two spin-flip transitions with ΔL=0 play an important role.

- isoscalar $M1$ transitions (ΔL=0, ΔS=1, ΔT=0, and ΔT_z=0).
- isovector $M1$ transitions (ΔL=0, ΔS=1, ΔT=1. and ΔT_z=0).

Since we are considering a 0^+ target nucleus. the spin-parity of the final state is 1^+.

In the PWIA, NN scattering amplitude can be expressed [25] as

$$M(q) = A + B\sigma_{1n}\sigma_{2n} + C(\sigma_{1n} + \sigma_{2n}) + E\sigma_{1q}\sigma_{2q} + F\sigma_{1p}\sigma_{2p} \ . \tag{1.4}$$

Each coefficient consists of isoscalar and isovector terms as

$$\begin{aligned} A &= A_0 + A_\tau \boldsymbol{\tau}_1 \cdot \boldsymbol{\tau}_2 \ , \\ B &= B_0 + B_\tau \boldsymbol{\tau}_1 \cdot \boldsymbol{\tau}_2 \ , \\ &\cdots \\ F &= F_0 + F_\tau \boldsymbol{\tau}_1 \cdot \boldsymbol{\tau}_2 \ , \end{aligned} \tag{1.5}$$

where A_0, A_τ, ..., and F_τ are C-numbers. The equation can be modified as

$$\begin{aligned} M(q) &= A + \frac{1}{3}(B + E + F)\boldsymbol{\sigma}_1 \cdot \boldsymbol{\sigma}_2 + C(\boldsymbol{\sigma}_1 + \boldsymbol{\sigma}_2) \cdot \hat{\boldsymbol{n}} \\ &\quad + \frac{1}{3}(E - B)S_{12}(\hat{\boldsymbol{q}}) + \frac{1}{3}(F - B)S_{12}(\hat{\boldsymbol{Q}}). \end{aligned} \tag{1.6}$$

The unit vectors are defined by the equations

$$\hat{\boldsymbol{q}} = \frac{\boldsymbol{k}_f - \boldsymbol{k}_i}{|\boldsymbol{k}_f - \boldsymbol{k}_i|} \ , \ \hat{\boldsymbol{Q}} = \frac{\boldsymbol{k}_i + \boldsymbol{k}_f}{|\boldsymbol{k}_i + \boldsymbol{k}_f|} \ , \text{ and } \hat{\boldsymbol{n}} = \hat{\boldsymbol{Q}} \times \hat{\boldsymbol{q}} \ , \tag{1.7}$$

where $\boldsymbol{k}_i$ and $\boldsymbol{k}_f$ is the initial and the final momentum vectors, respectively. The central spin-independent component (A) vanishes for spin-flip transitions. The spin-orbit component (C) and the direct tensor component (E-B) vanish in the case of ° scattering. Then the PT observables are written [26, 27] as

$$\begin{aligned} D_{SL} &= D_{LS} = 0 \ , \\ D_{SS} &= D_{NN} = \frac{(|B_i|^2 - |F_i|^2)X_T^2 - |B_i|^2 X_L^2}{(|B_i|^2 + |F_i|^2)X_T^2 + |B_i|^2 X_L^2} \ , \\ D_{LL} &= \frac{(-3|B_i|^2 + |F_i|^2)X_T^2 + |B_i|^2 X_L^2}{(|B_i|^2 + |F_i|^2)X_T^2 + |B_i|^2 X_L^2} \ , \end{aligned} \tag{1.8}$$

where X_T and X_L denote spin-transverse and spin-longitudinal form factors, respectively. The suffix, i, is taken as 0 for isoscalar transitions and as τ for isovector transitions. The PT observable D_{NN} is equal to D_{SS} due to the rotational symmetry. The form factors are related to the total angular momentum transfer ΔJ as

$$\frac{X_L^2}{X_T^2} = \begin{cases} \frac{2\Delta J}{\Delta J+1} & \text{for } \Delta J = \Delta L + 1 \\ \frac{2(\Delta J+1)}{\Delta J} & \text{for } \Delta J = \Delta L - 1 \end{cases} \tag{1.9}$$

Since small ΔL reactions are highly enhanced at 0°, we can suppose that the contribution from the smaller ΔL (=$\Delta J - 1$) is dominant and the contribution from the larger ΔL (=$\Delta J + 1$) is negligible for a specified $\Delta J > 0$.

Let us consider the PT observables for the isoscalar and isovector $M1$ transitions. In this case X_T^2 is equal to X_L^2 and we obtain

$$\begin{aligned} D_{SS} &= \frac{-F_i^2}{F_i^2 + 2B_i^2} , \\ D_{LL} &= \frac{F_i^2 - 2B_i^2}{F_i^2 + 2B_i^2} . \end{aligned} \tag{1.10}$$

We define α_i as the strength ratio of the spin-dependent central component ($B_i + E_i + F_i$) to the knock-on exchange tensor component ($F_i - B_i$):

$$\alpha_i = \frac{B_i + E_i + F_i}{F_i - B_i} = \frac{F_i + 2B_i}{F_i - B_i} . \tag{1.11}$$

The PT observables, D_{SS} and D_{LL}, are expressed by α_i in the forms

$$\begin{aligned} D_{SS} &= -\frac{1}{3} - \frac{2}{3} \cdot \frac{1 + 2Re(\alpha_i)}{2 + |\alpha_i|^2} , \\ D_{LL} &= -\frac{1}{3} + \frac{4}{3} \cdot \frac{1 + 2Re(\alpha_i)}{2 + |\alpha_i|^2} . \end{aligned} \tag{1.12}$$

Therefore, the PT observables are determined by the strength ratio of the spin-dependent central and the knock-on exchange tensor components which contribute to the transition.

The isovector $M1$ transitions are mainly mediated by the isovector central spin-dependent interaction ($V_{\sigma\tau}$) [28]. If the contributions from the knock-on exchange tensor interactions are neglected ($\alpha_\tau \to \infty$) as an extreme case, we obtain the following values from Eq. 1.12:

$$D_{SS} = -\frac{1}{3} \quad \text{and} \quad D_{LL} = -\frac{1}{3} \quad (\text{when } \alpha_\tau \to \infty) . \tag{1.13}$$

In actual, the isovector tensor interaction (V_τ^T) contributes to the transitions through the knock-on exchange amplitudes, and the PT observables deviate from the above values depending on the strength ratio of V_τ^T to $V_{\sigma\tau}$. Since the strength of $V_{\sigma\tau}$ has been well studied via the (p, n) and (p, p') reactions, the strength of V_τ^T can be determined by measuring the PT observables for the isovector $M1$ transitions at 0°.

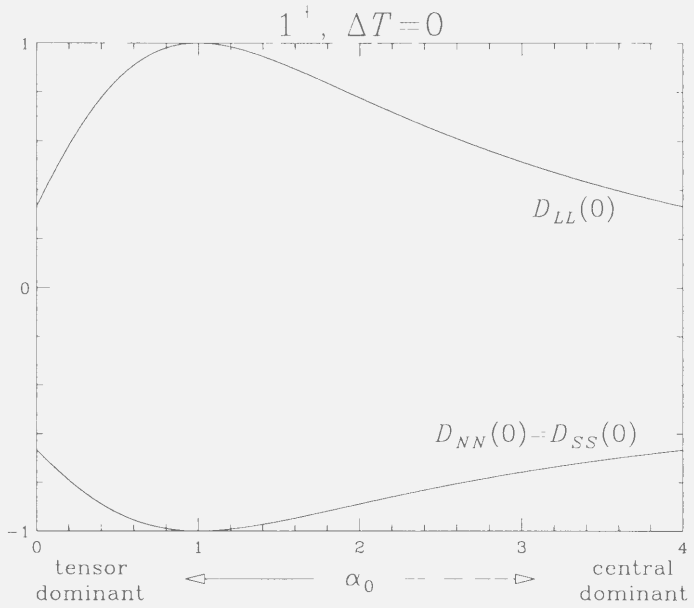

Figure 1.4: The dependence of the PT observables on pure real α_0 values, where α_0 represents the relative strength of the isoscalar spin-dependent interaction (V_σ) to the exchange tensor interaction (V_τ^T).

The isoscalar $M1$ transitions are mainly mediated by V_τ^T through the knock-on exchange amplitudes [28, 29]. If we neglect the contributions from the central interactions ($\alpha_0 \to 0$) as an extreme case, we obtain

$$D_{SS} = -\frac{2}{3} \quad \text{and} \quad D_{LL} = +\frac{1}{3} \quad (\text{when } \alpha_0 \to 0) \ . \tag{1.14}$$

But in reality, the isoscalar central spin-dependent interaction (V_σ) also contributes to the transitions. By measuring the PT observables for the isoscalar $M1$ transitions, the strength of V_σ can be deduced relative to that of V_τ^T which is determined from the study of the isovector $M1$ transitions. The dependence of the PT observables on pure real α_0 is plotted in Fig. 1.4. One of the purposes of this work is to empirically determine the strength of V_σ.

1.5 Study of spin-isospin excitations in nuclei

At the scattering angle of 0°, ΔL=0 excitations are strongly enhanced. That is one of the reasons why proton and light ion reactions at 0° have discovered various collective excitations such as GT states, isobaric analog states, and giant monopole resonances. The observables in nucleon-nucleus scattering at 0° are powerful probes to study spin-isospin excitations in nuclei.

The GT transitions in the (p,n) channel, isobaric analog states, and their decay properties have been extensively studied via the (p,n) [30], (^{3}He, t) [32], and (^{6}Li,^{6} He) [31] reactions. The GT transitions in the (n,p) channel have been investigated via (n,p), $(d,{}^2\mathrm{He})$ [33], $(t,{}^3\mathrm{He})$ [34], and (^{7}Li,^{7} Be) [35] reactions. The $(d,{}^2\mathrm{He})$ reaction exclusively excites spin-flip (ΔS=1) transitions and is suitable for studying GT states and spin dipole resonances (SDR, ΔS=1, ΔL=1). Spin-flip and non-spin-flip transitions by the (^{7}Li,^{7} Be) reaction can be decomposed by detecting the gamma-ray from the excited ^{7}Be nucleus in coincidence.

The new experimental technique to measure the (p,p') reaction at 0° is hopeful to study the spin-isospin excitations in nuclei, since it provides high energy resolution with high detection efficiency, and the reaction mechanism is simple comparing with the reactions of composite particles. In addition, the PT observables at 0° are sensitive to macroscopic properties of the excited states, *i.e.*, spin, parity, and isospin, while they are insensitive to the details of the shell-model configurations of the excited states and distortion effects [24]. Fig. 1.5 shows DWIA calculations for the excitation of the isoscalar and isovector $M1$ states via the $^{12}\mathrm{C}(p,p')$ reaction. The solid curves represent the calculation with realistic target wave functions by Cohen and Kurath [36]. The dashed curves represent the one with a simple $(0p_{1/2}\,0p_{3/2}{}^{-1})$ configuration. It can be seen from the figure that the PT observables at forward angles are quite insensitive to the configuration of the excited state. In Fig. 1.6 the DWIA and the PWIA calculations for the $M1$ states are compared. The PT observables at very forward angles are insensitive also to the distortion effects. From the calculations, it is justified to expect that the macroscopic

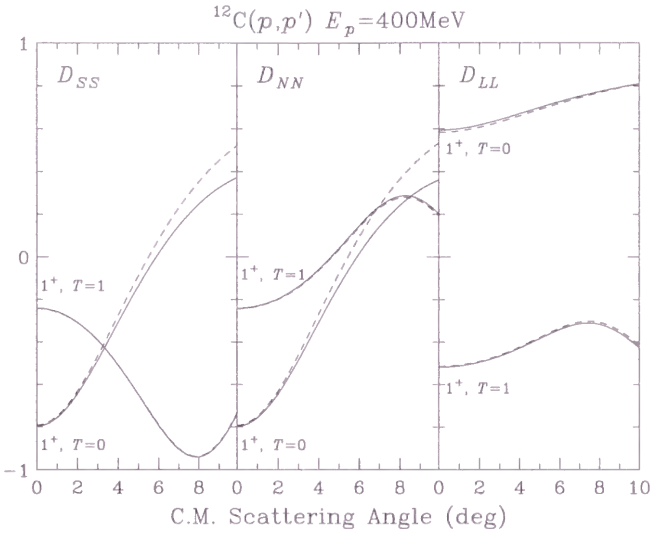

Figure 1.5: Predictions of the PT observables by the DWIA calculations for the excitations of the 1^+, T=0 state and the 1^+, T=1 state on ^{12}C using the Franey and Love effective interaction. Cohen and Kurath target wave functions are employed in the calculations represented by the solid curves, while a simple $(0p_{1/2}\,0p_{3/2}{}^{-1})$ configuration is assumed in the calculation of the dashed curves.

properties of excited states can be studied with little ambiguity from the configuration of the excitated states and the distortion effects.

The (p,p') reaction can excite various spin-isospin modes: $(\Delta S,\ \Delta T)$=(0,0), (1,0), (0,1), and (1,1). Although all the modes can be studied by the reaction, the problem is how to extract the information on the spin-isospin mode of excitation strengths. In this work, we try a new approach to extract spin-isospin information of excited states from PT observables at 0°. For this purpose, two quantities are newly defined. One is total spin transfer and the other is $S_{LL} - S_{SS}$.

The total spin transfer (Σ)is defined [38] by a linear combination of the PT observables as

$$\Sigma \equiv \frac{3 - (D_{SS} + D_{NN} + D_{LL})}{4} \ . \tag{1.15}$$

At 0°, it has the form

$$\Sigma = \frac{3 - (2D_{SS} + D_{LL})}{4} \quad \text{(at 0°)} \ . \tag{1.16}$$

The total spin transfer takes unity for spin-flip (ΔS=1) transitions and zero for non-spin-

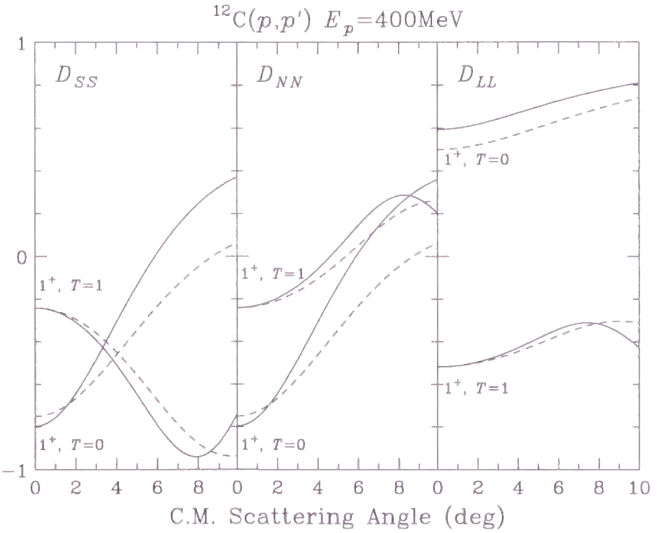

Figure 1.6: Predictions of the PT observables by the DWIA calculations for the excitations of the 1^+, T=0 state and the 1^+, T=1 state on ^{12}C using the Franey and Love effective interaction and the Cohen and Kurath target wave functions. Solid curves show the results with an optical potential taken from Ref. 37, while dotted curves show the results with plane waves for the initial and final states.

flip (ΔS=0) transitions provided that the spin-orbit (LS) interaction is negligible [39]. The condition is valid in the case of (p, p') reactions at 0°. By measuring the total spin transfer, excitations in the continuum region can be decomposed into the spin-flip part and the non-spin-flip part.

The PT observable D_{LL} is sensitive to the isospin (T) of the excited $M1$ states as can be seen in Fig. 1.6. The quantity, $S_{LL} - S_{SS}$, is more sensitive to the isospin of the spin-flip states. From Eq. 1.8, S_{LL}-S_{SS} can be written in the form

$$\begin{aligned} S_{LL} - S_{SS} &= \frac{1}{2}(D_{SS} - D_{LL}) \\ &= \frac{(2|B_i|^2 - |F_i|^2)X_T^2 - |B_i|^2 X_L^2}{(|B_i|^2 + |F_i|^2)X_T^2 + |B_i|^2 X_L^2} , \end{aligned} \tag{1.17}$$

where S_{LL}=(1-D_{LL})/2 and S_{SS}=(1-D_{SS})/2 are the longitudinal and transverse spin-flip probabilities, respectively. The DWIA calculations predict that $S_{LL} - S_{SS}$ takes positive values for isovector spin-flip transitions with ΔL=0 or 1, and takes negative values for the isoscalar spin-flip transitions. Details are discussed in Sec. 5.5.

1.6 Purposes of this work

The purposes of the $(\vec{p}, \vec{p}')$ experiment at 0° are summarized as follows.

1. Determination of the strength of V_σ.

   This is an attempt to investigate the details of the reaction mechanism. Franey and Love (FL) derived [28, 40] the strengths of all the terms of the effective interaction by fitting them to the free NN scattering phase shifts. They noted, however, that the determination of V_σ was poor [28, 41]. The reason of the poor determination is the insensitivity of the NN scattering observables to the small V_σ strength. Until now the strength of the V_σ has not been empirically determined.
   However, specified interactions can be selectively studied by measuring a suitable excitation in nucleon-nucleus scattering as we have seen in Sec. 1.4. The PT observables for the isoscalar $M1$ transitions at 0° are sensitive to the strength of V_σ. By using this property, the strength of V_σ is studied.

2. Establishment of the measurement of the PT observables at 0° as a powerful probe to study spin-isospin excitations.

   The second purpose is to establish the PT observables at 0° as a spectroscopic tool by applying their unique properties. Spin-flip and non-spin-flip excitations can be decomposed by using the total spin transfer. The quantity $S_{LL} - S_{SS}$ is sensitive to the isospin of the spin-flip excitations. The sensitivity of the PT observables to the spin-isospin mode of the excited states is investigated for known excitation strengths on ^{12}C.

In Chap. 2, the experimental setup and conditions are described. The procedure of the data analysis is explained in Chap. 3. The experimental results are presented in Chap. 4. In Chap. 5, the results are compared with calculations with distorted wave impulse approximation. The strength of V_σ and other interaction strengths are discussed. The

spin-isospin decomposition of the excitation strength on ^{12}C is performed. Concluding remarks are give in Chap. 6.

Chapter 2

EXPERIMENT

The experiment was performed at the Research Center for Nuclear Physics (RCNP), Osaka University, by using a high resolution spectrometer *Grand Raiden* [42] and a focal plane polarimeter (FPP) [43]. An overview of the RCNP facility is illustrated in Fig. 2.1. In this chapter, details about the detector setup and the experimental conditions are described.

2.1 Beam line

2.1.1 Polarized proton beam

A polarized proton beam was provided by a high intensity polarized ion source (HIPIS) [44]. The HIPIS employs cold (30 K) atomic beams and an electron cyclotron resonance (ECR) ionizer. The polarized proton beam extracted from the HIPIS was bent from the horizontal direction to the vertical direction by an electrostatic deflector and a dipole megnet, and was injected to an AVF (Azimuthally Varying Field) cyclotron with the polarization axis in the vertical direction. The beam was accelerated by the AVF cyclotron up to a kinetic energy of 64.2 MeV. The polarization axis was rotated from the vertical direction to the horizontal direction by using one of two super-conducting solenoids placed at an injection line of the K400 ring cyclotron. The beam was accelerated by the ring cyclotron up to 392 MeV. Single turn extraction from the ring cyclotron was performed.

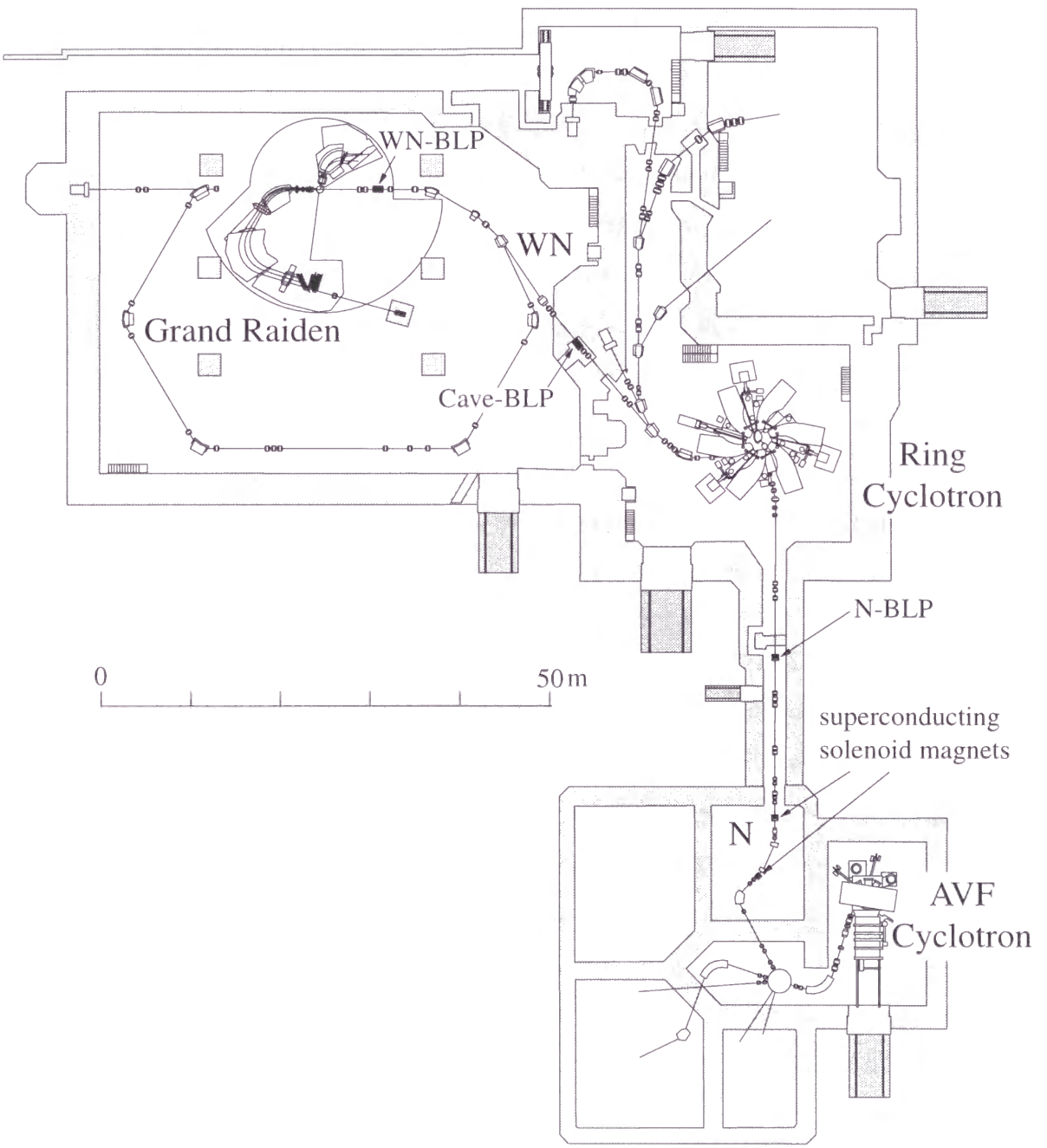

Figure 2.1: Overview of the RCNP facility.

The horizontally polarized beam was transported to the WN experimental hall, where it bombarded a target in the scattering chamber.

The beam intensity was 2–3 nA, which was limited by the leak currents of wire chambers (Sec. 2.4) and the dead time of the data acquisition system (Sec. 2.6). The maximum available beam intensity was also 2–3 nA after the beam was tuned by using slits and Q-magnets so as to have a minimum halo. The direction of the beam polarization was flipped every 0.5 seconds by using the strong and weak transition units of the HIPIS alternatively. The typical beam polarization was 0.7. The direction of the beam polarization in the horizontal plane was adjusted by changing the super-conducting solenoid, or by selecting another beam turn of the cyclotron orbit. The latter was made by tuning the phase and voltage of the flat-top cavity.

2.1.2 Beam line polarimeter

The polarization of the proton beam was measured by two sets of beam line polarimeters (BLPs). Fig. 2.2 illustrates the setup of the BLPs. A plastic scintillator made of polystyrene with a thickness of 0.3 mm was used as the analyzer target. The p-p scatterings, free p-p and quasi-free p-p from carbon nuclei, were measured in coincidence. The trigger signal L (left) was generated by taking the coincidence of the signals from the detectors labeled L and L', and the trigger signal R (right) from the detectors labeled R and R'. The y component of the beam polarization was derived from the asymmetry of the number of the L and R triggers. Similarly, the x component of the beam polarization was obtained from the signals of D (down), D', U (up), and U' plastic scintillators in the y direction. The analyzer target was put in the beam only when the beam polarization was monitored.

The BLPs, CAVE-BLP and WN-BLP, have the same detector configuration, and are placed at the WN beam line with a relative angle of 50° as shown in Fig. 2.3. All the three-dimensional components of the beam polarization at the target position can be deduced from the polarizations measured by the two BLPs. The procedure of deducing

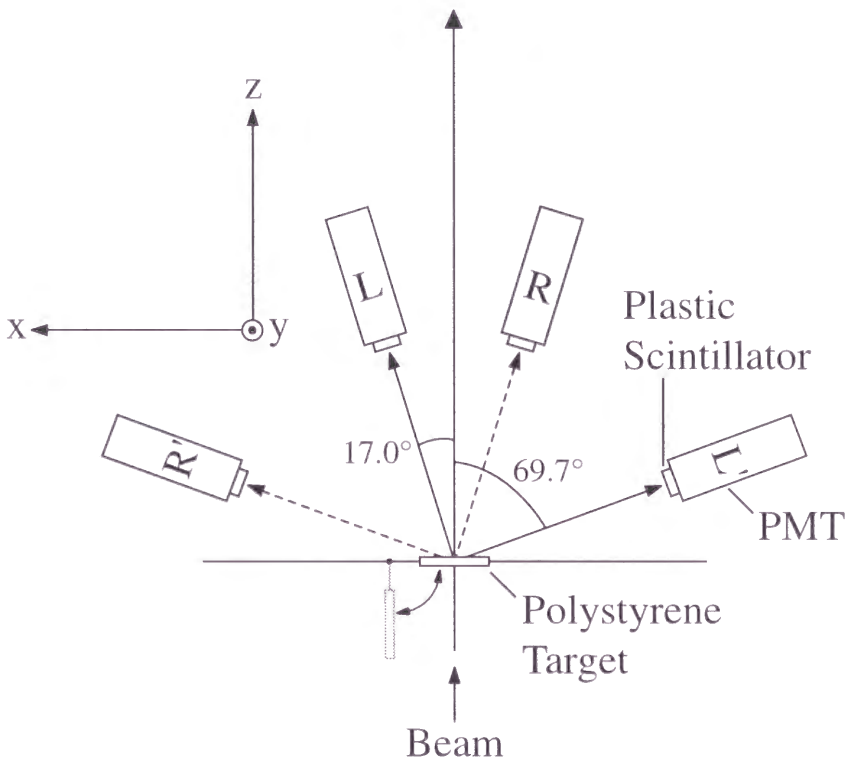

Figure 2.2: Setup of counters of the BLP in the horizontal plane (top view).

the polarization is described in Sec. 3.3.

The beam polarization was measured by putting the analyzer targets in the beam line (BLP-in mode) for 20 seconds in every 2 minutes. The BLP targets were removed from the beam line (BLP-out mode) during the data acquisition of the focal plane events in order to remove the background from the multiple scattering of the beam at the BLP targets.

2.2 Target

A self-supporting natural carbon sheet with a thickness of 30 mg/cm^2 was used as the target. The carbon sheet was mounted on a target frame made of aluminum. An empty target frame was used for the beam tuning and for the check of the experimental background. The target frames were mounted on a target ladder placed at the center of the

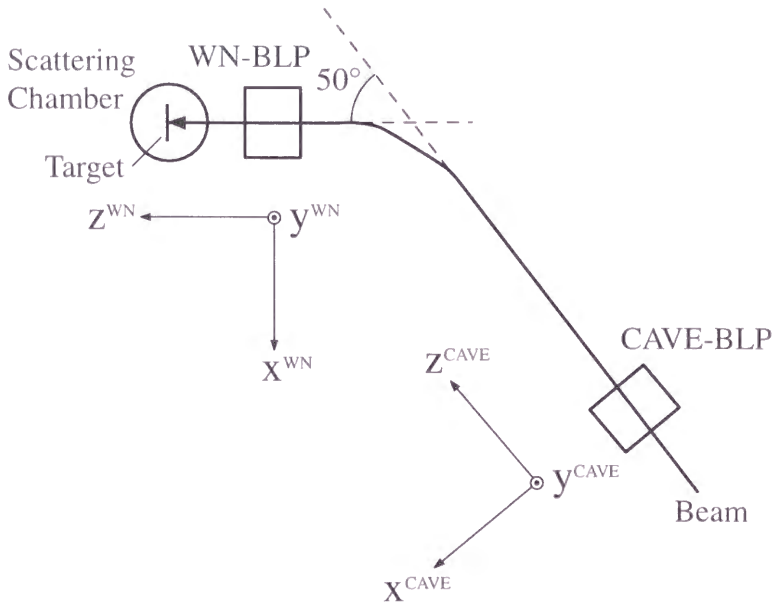

Figure 2.3: The CAVE-BLP and WN-BLP, are placed at the WN beam line with a relative angle of 50°. All the three-dimensional components of the beam polarization are determined from the polarizations measured by the two BLPs.

scattering chamber.

2.3 Grand Raiden spectrometer

Fig. 2.4 shows the setup of the high resolution magnetic spectrometer *Grand Raiden* [42] for experiments at 0°. The properties of the *Grand Raiden* spectrometer are summarized in Table 2.1. The spectrometer has a QSQDMD(+D) configuration. It provides a large momentum resolving power of $p/\Delta p = 37{,}000$ and a large momentum acceptance of 5%. The last dipole magnet, named Dipole for Spin Rotation (DSR), is capable of bending protons additionally to +18° (DSR+ mode) or -17° (DSR- mode) with little distortion of the ion optics. By combining the measured proton polarization for the two mode, all the three-dimensional components of the polarization can be determined. In this experiment, the DSR magnet was used to adjust the direction of the primary beam to the Faraday cup placed 12 m downstream of the focal plane.

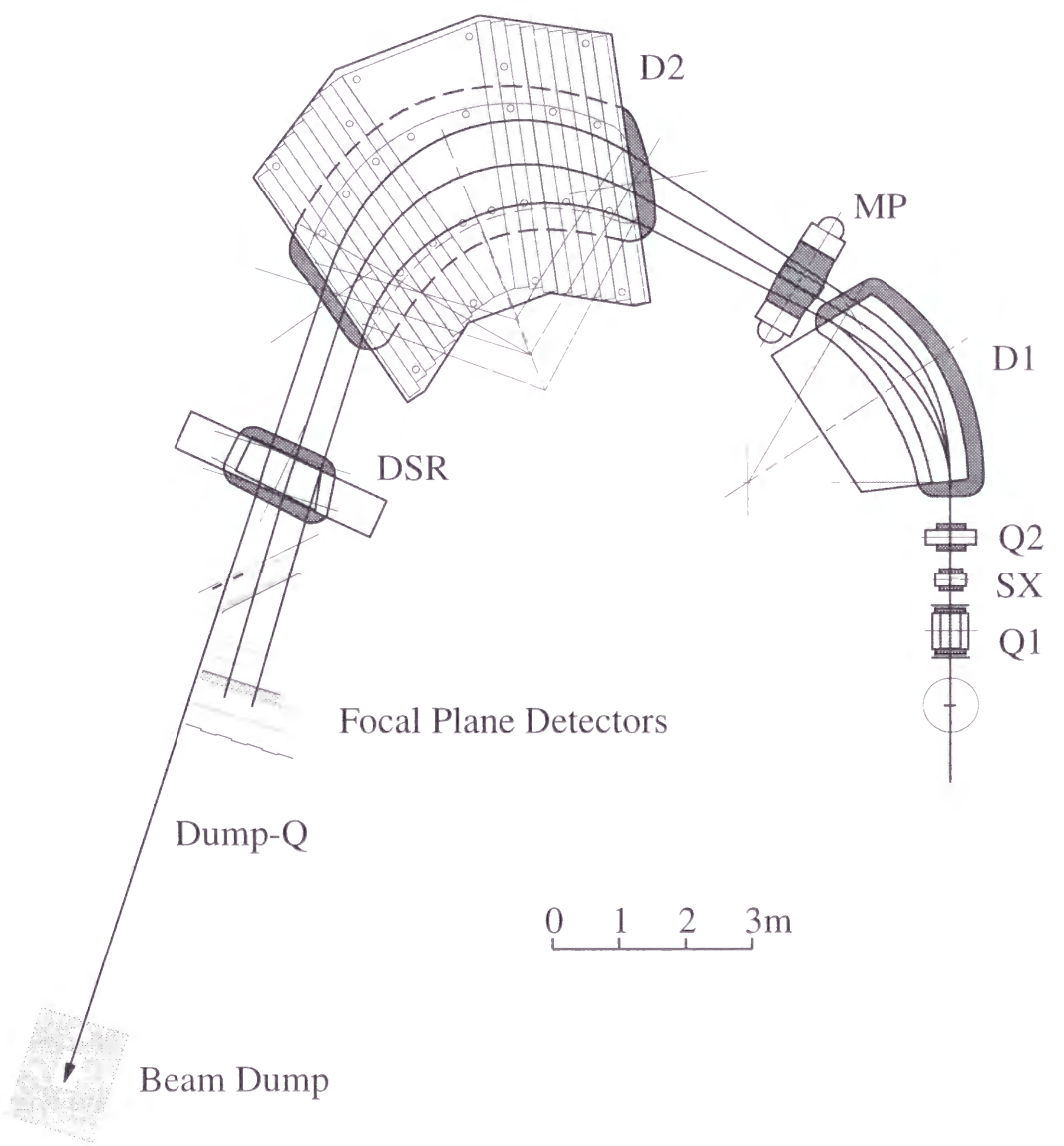

Figure 2.4: Spectrometer *Grand Raiden* in the setup of the experiment at 0°.

Table 2.1: Design specification of the *Grand Raiden* spectrometer.

Configuration	QSQDMD(+D)
Mean orbit radius	3 m
Total deflection angle	162°
Focal plane length	150 cm
Focal plane tilting angle	45.0°
Maximum particle rigidity	54kG-m
Momentum resolving power $p/\Delta p$	37,000
Momentum broadness	5%
Horizontal magnification $(x\|x)$	-0.417
Vertical magnification $(y\|y)$	5.98
Momentum dispersion $(x\|\delta)$	15451 mm

2.4 Focal plane detector system

The focal plane detector system consists of two units, *i.e.* the standard focal plane detectors and the focal plane polarimeter (FPP). These detectors are illustrated in Fig. 2.5. In this section, the structures of the detectors are described.

2.4.1 Standard focal plane detectors

Standard focal plane detectors consist of two multi-wire drift chambers of vertical drift type (VDCs) [45], and a plastic scintillation counter (PS1). Characteristics of the VDCs are summarized in Table 2.2. The wire configuration of the VDCs is illustrated in Fig. 2.6. The VDCs give the position and the incidence angle of charged particles at the focal plane. Holes are placed in the frames of the VDCs near the sensitive area. For experiments at 0°, these holes allow the primary beam to pass through. Measurement of nuclear excitations as low as 5 MeV has been achieved. A high voltage of -5.6 kV is applied to the cathode planes of the VDCs, and -300 V to the potential wires. The high voltage of the cathode planes was lowered during the BLP-in mode in order to reduce the large leak current caused by the background particles from multiple scattering at the BLP targets. The typical leak current in the BLP-out mode was 10 μA for each VDC. but it depended

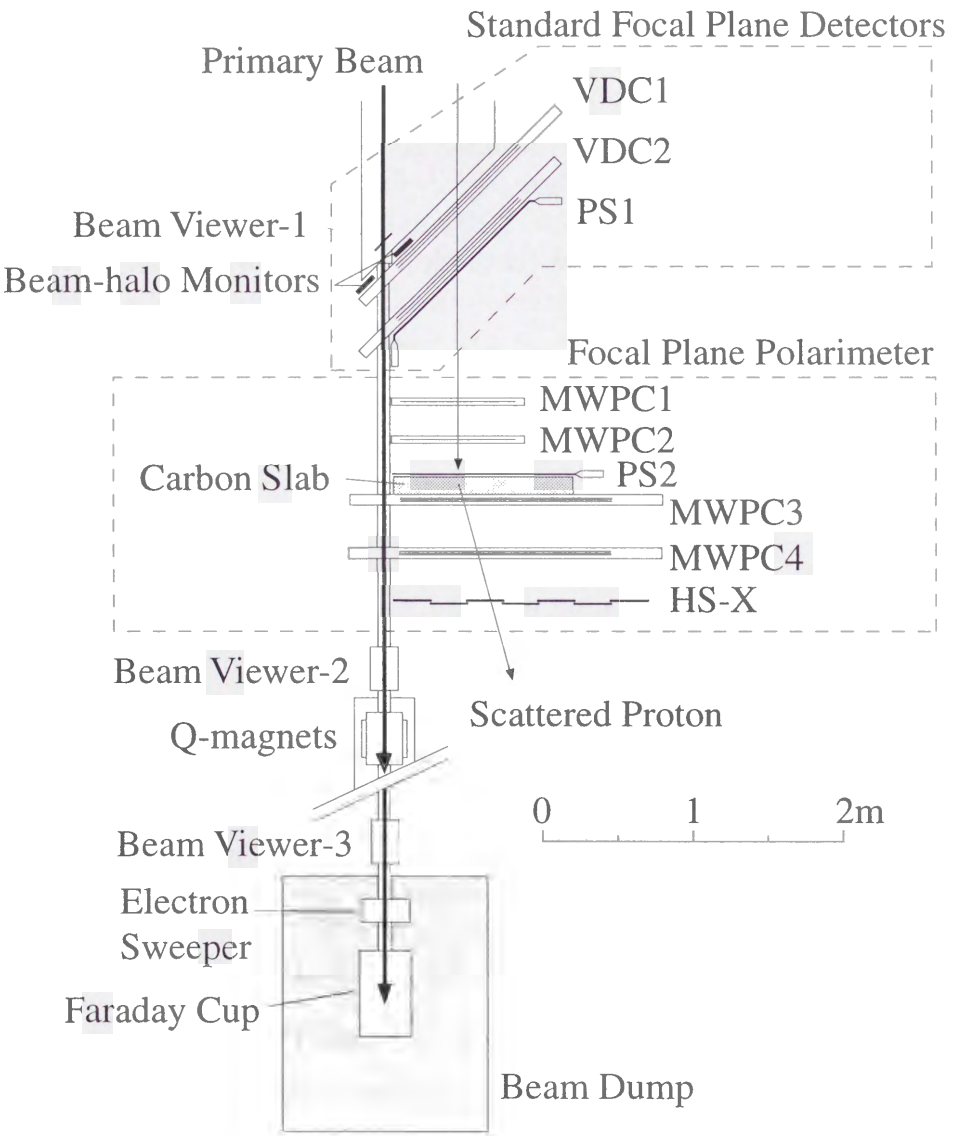

Figure 2.5: The standard focal plane detectors and the Focal Plane Polarimeter (FPP) at the focal plane of the spectrometer in the setup of the 0° experiment.

Table 2.2: Specification of the VDCs.

Wire configuration	X(0°), U(-48.2°)
Active area	$1150^{W} \times 120^{H}$ mm
Number of sense wires	192 (X), 208 (U)
Anode-cathode gap	10 mm
Anode wire spacing	2 mm
Sense wire spacing	6 mm (X), 4 mm (U)
Anode sense wires	20 μmϕ gold-plated tungsten wire
Anode potential wires	50 μmϕ gold-plated beryllium copper wire
Cathode film	10 μm carbon-aramid film
Applied voltage	-5600 V (cathode), -300 V (potential), 0 V (sense)
Gas mixture	argon:iso-butane:iso-propyl-alcohol = 70:30:*[1]
Pre-amplifier	LeCroy 2735DC
Digitizer	LeCroy 3377 drift chamber TDC

[1]Mixed with the argon gas in 2°C vapor pressure.

on the beam quality. A gas mixture of argon (70%) and iso-butane (30%) is used. Iso-propyl alcohol is mixed at 2°C vapor pressure with the argon gas. The signals from the anode wires are pre-amplified and discriminated by LeCroy 2735DC cards, and the timing information is digitized by LeCroy 3377 drift chamber TDCs. The performance of the VDCs is described in Sec. 3.5.

In order to reduce multiple scatterings, a thin plastic scintillator with a thickness of 3 mm is used as the PS1. The light guide of the photo-multiplier tubes (PMTs) on both sides of the PS1 is bent for 45° in order not to interfere with the beam duct for the primary beam. The signals from the PS1 are used to generate trigger signals. The timing and charge of the PS1 signals are digitized by LeCroy FERA and FERET systems and are recorded by the data acquisition system.

2.4.2 Focal plane polarimeter (FPP)

The polarization of the scattered protons are measured by the FPP. As polarimetries, p+C elastic, inelastic and quasi-free scatterings are inclusively measured. One of the

characteristics of the FPP is its large size with which all the momentum acceptance of the *Grand Raiden* spectrometer is covered at once. As shown in Fig. 2.5, the FPP consists of four multi-wire proportional chambers (MWPC1–4), a carbon slab as the second scatterer, a plastic scintillator (PS2) in front of the scatterer, and a plastic scintillator hodoscope (HS-X).

The specifications of the MWPCs are summarized in Table 2.3. The wire configuration of the MWPCs is illustrated in Fig. 2.6. The MWPC3 and MWPC4 have three anode planes: X (0°:vertical), U (-45°), and V (+45°). The X planes were not used in the experiment due to the limitation of the readout electronics. The MWPC1 and MWPC2 have one anode wire plane (X). The counter gas is a mixture of argon (66), iso-butane (33), and freon (0.3). Iso-propyl-alcohol is mixed in 2°C vapor pressure with the argon gas at 1 atm in order to reduce the aging effects of the anode wires. A high voltage of -4.7 kV is applied to the MWPC3 and MWPC4, and -4.9 kV to the MWPC1 and MWPC2. The high voltage was lowered during the BLP-in mode to reduce the leak currents due to the background particles. The typical leak currents in the BLP-out mode were 2 μA for the MWPC1 and MWPC2, 25 μA for the MWPC3, and 50 μA for the MWPC4. Holes are opened in the frame of the MWPC3 and MWPC4 allowing the primary beam duct to pass through. The performance of the MWPCs is described in Sec. 3.7.

A carbon slab with a thickness of 12 cm is used. The thickness is optimized considering the polarimetry efficiency and the multiple scattering effects. The density of the carbon block was 1.7 g/cm^3. The thickness of the PS2 is 3 mm. The light output of the PS2 is detected by a PMT placed on the low momentum side of the PS2. The HS-X consists of 8 plastic scintillation counters with an area of 200 mm $\times$ 800 mm and a thickness of 10 mm. The light outputs are detected by the PMTs on both upper and lower sides.

The polarization of the protons is obtained from the asymmetry during the inclusive scattering at the carbon slab. The MWPC3 and MWPC4 determined both the x and y trajectories of scattered protons. The MWPC1 and MWPC2 determined only the x trajectory of incoming protons. The MWPC1 and MWPC2 are used only for the

Table 2.3: Specification of the MWPCs.

	MWPC1,2	MWPC3	MWPC4
Wire configuration	X(0°)	X(0°), U(-45°), V(+45°)	
Active area	$760^{W} \times 200^{H}$ mm	$1400^{W} \times 418^{H}$ mm	$1400^{W} \times 600^{H}$ mm
Number of wires	384	704 (X), 640 (U,V)	704 (X,U,V)
Anode-cathode gap	6 mm		
Anode wire spacing	2 mm		
Anode wires	25 mmϕ gold-plated tungsten wire		
Cathode film	10 μm carbon-aramid		6 μm aluminized mylar
Cathode voltage	-4900 V	-4700 V	
Gas mixture	argon:iso-butane:freon:iso-propyl-alcohol = 66:33:0.3:[1]		
Pre-amplifier	LeCroy 2735PC and Nanometric N277-C3		
Digitizer	LeCroy PCOS III		

[1]Mixed with the argon gas in 2°C vapor pressure.

second-level trigger system (Sec. 2.5.2).

2.5 Trigger system

The event branches selected by the trigger system is illustrated in Fig. 2.7. As described in Sec. 2.5.1, the first-level trigger system generates FP triggers and FPP triggers according to the sampling conditions and the signals from the PS1, PS2, and Hodoscope-X counters. The FP trigger is generated by taking the coincidence of the signals of the PS1 and PS2. Every n-th FP event is unconditionally recorded by the data acquisition system (FP sampling event), where n is a preset sampling rate. For other FP events, the trigger system generates FPP triggers if the FP trigger occurs in coincidence with the HD-X signal. Every m-th FPP event is unconditionally recorded (2nd-Level sampling event). For other FPP events, the trigger system determines whether to record the event or not, according to the decision of the 2nd-Level trigger system which is described in Sec. 2.5.2.

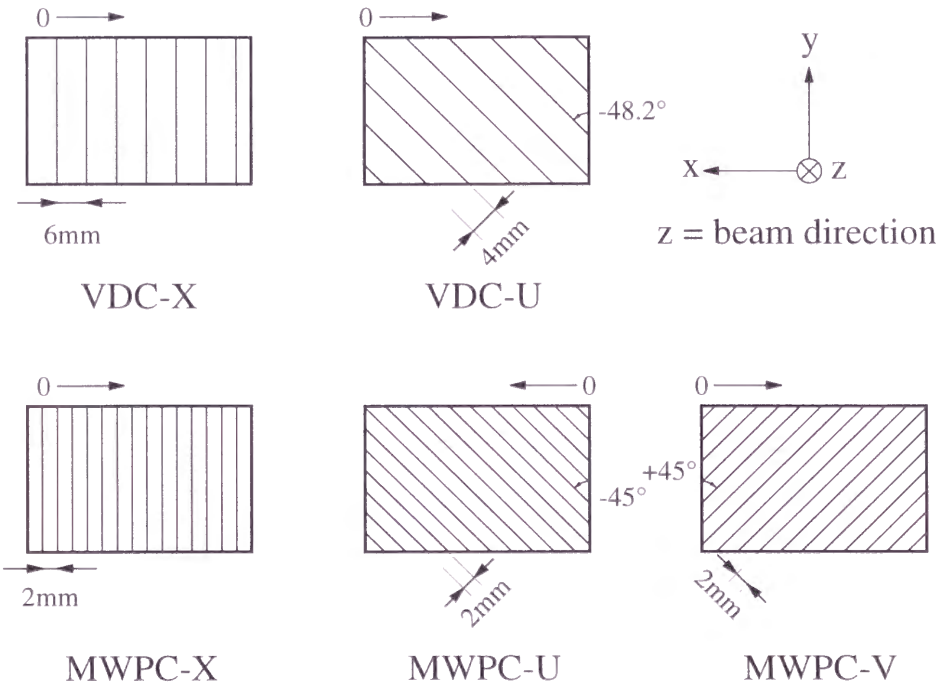

Figure 2.6: Wire configuration of the VDCs and MWPCs. The wire numbering orders are shown by the arrows.

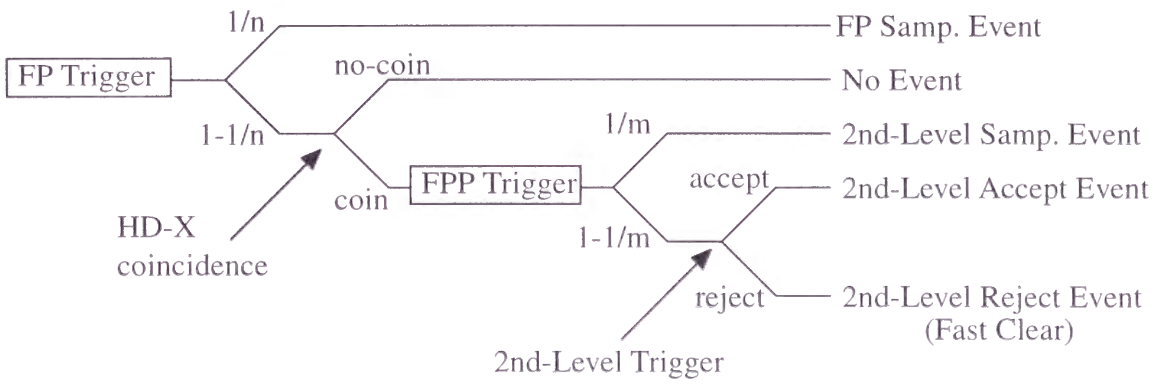

Figure 2.7: Event branches by the trigger system illustrated in Fig. 2.9. The sampling rates were set as (n, m)=(1, any value) for the singles (cross section) measurement, and (n, m)=(20, ∞) or (n, m)=(∞, 20) for the polarization transfer measurement.

2.5.1 First-level trigger

A logic diagram of the first-level trigger system is illustrated in Figs. 2.8 and 2.9. The core of the trigger system [46] is designed by a CAD system on a personal computer and down-loaded to field programmable gate arrays (FPGAs) in three LeCroy 2366 Universal Logic Modules. The FPGAs are programmed to be capable of changing the detailed configuration of the trigger circuit via CAMAC functions. For example, sampling rates and coincidence logic of the triggers can be changed.

The trigger system generates two types of triggers.

- focal plane (FP) trigger

  The FP triggers are generated by taking the coincidence of the signals from the PS1 and PS2 (PS1∩PS2). Here the PS1 signal is the coincidence of the signals from both the PMTs of the PS1.

- focal plane polarimeter (FPP) trigger

  The FPP triggers are generated by taking the coincidence of the signals PS1∩PS2 and HS-X (PS1∩PS2∩HSX) when the FP sampling event is not generated. Here the HS-X signal is created by taking *OR* of all the PMT signals of the HS-X.

For every n-th FP trigger, the n-1 signal of the counter-1 in Fig. 2.9 is generated, and the event is recorded as an FP sampling event independently of whether the HD-X signal occurs or not. The sampling rate, n, can be changed by a CAMAC function. For other FP triggers, the FPP trigger is generated if the FP trigger occurs in coincidence with the HD-X signal. After the triggers are generated, the counter is incremented preparing for the next event. When an FP or FPP event is generated, the trigger system sets the busy status and distributes gate signals to analog-to-digital converters (ADCs) and start/stop signals to time-to-digital converters (TDCs). The trigger circuit is designed so that the timing of the gate signals does not depend on the type of the triggers.

For every m-th trigger, the m-1 signal of the counter-2 is generated, and the event is recorded as a second-level sampling event independently of the decision of the second-

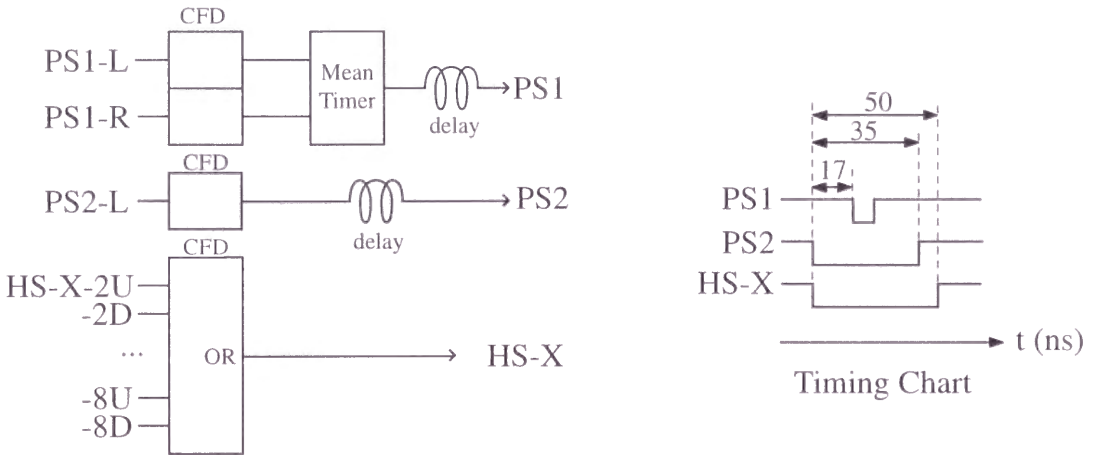

Figure 2.8: Schematic diagram of the trigger sources. The triggers are generated from the signals of the plastic scintillation counters.

level trigger system. For other FPP triggers, the trigger system determines whether to take the event or not, according to the decision of the second-level trigger system, which is described in Sec. 2.5.2. If the decision is 'accept', the system records the event as a second-level accept event and clears the busy status. Otherwise, *i.e.* if the decision is 'reject', the system distributes clear signals (fast clear) to all the digitizer modules. After a fixed time (1.5 μsec), which is sufficient to clear all the modules, the system clears the busy status and becomes ready for the next event.

2.5.2 Second-level trigger

One of the most important parts of the FPP is the second-level trigger system [47]. Most of the triggered events have small scattering angles at the carbon slab, and are useless to determine the polarization of the protons since the analyzing power for such events is small. In order to avoid taking these meaningless events, the second-level trigger system has been developed. The system calculates a rough scattering angle in a few micro seconds and makes decision whether to take the event (accept) or not (reject). A diagram of the second-level trigger system is illustrated in Fig. 2.10. The system is also based on a field programmable gate array on a LeCroy 2366 universal logic unit.

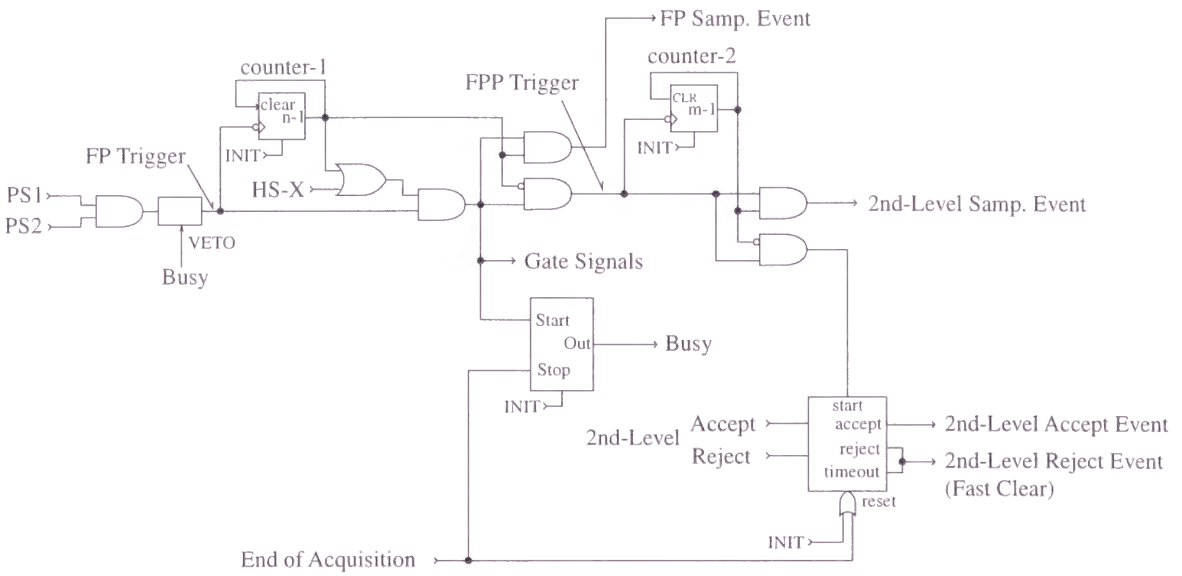

Figure 2.9: Schematic diagram of the trigger circuit down-loaded to the FPGA in LeCroy 2366 Universal Logic Modules.

The scattering angle at the carbon block is calculated from the hit positions at the four MWPCs. The data from the VDCs are not used because of a relatively large conversion time of the TDCs and the complexity of calculating the hit positions. The wire number of the center position of the clusters in each MWPC plane is obtained by a LeCroy PCOS III system. The data are transfered to the second-level trigger system via ECL bus lines and stored in the memory of the FPGA.

The horizontal direction of the incoming proton is approximately proportional to $x_2 - x_1$ as

$$\theta_x^{\rm in} \sim \tan\theta_x^{\rm in} = \frac{d}{D^{\rm in}}(x_2 - x_1) \ , \tag{2.1}$$

where x_1 (x_2) is the wire number hit in the X-plane of the MWPC1 (MWPC2), $D^{\rm in}$ is the distance between the MWPC1 and the MWPC2, and d is the wire spacing (2 mm). The direction of the incoming proton is approximated to be in the horizontal plane according to the ion optical properties of the Grand Raiden. Then the projections of the incoming beam direction onto the U and V planes ($\mp 45^\circ$ from the vertical direction) are written

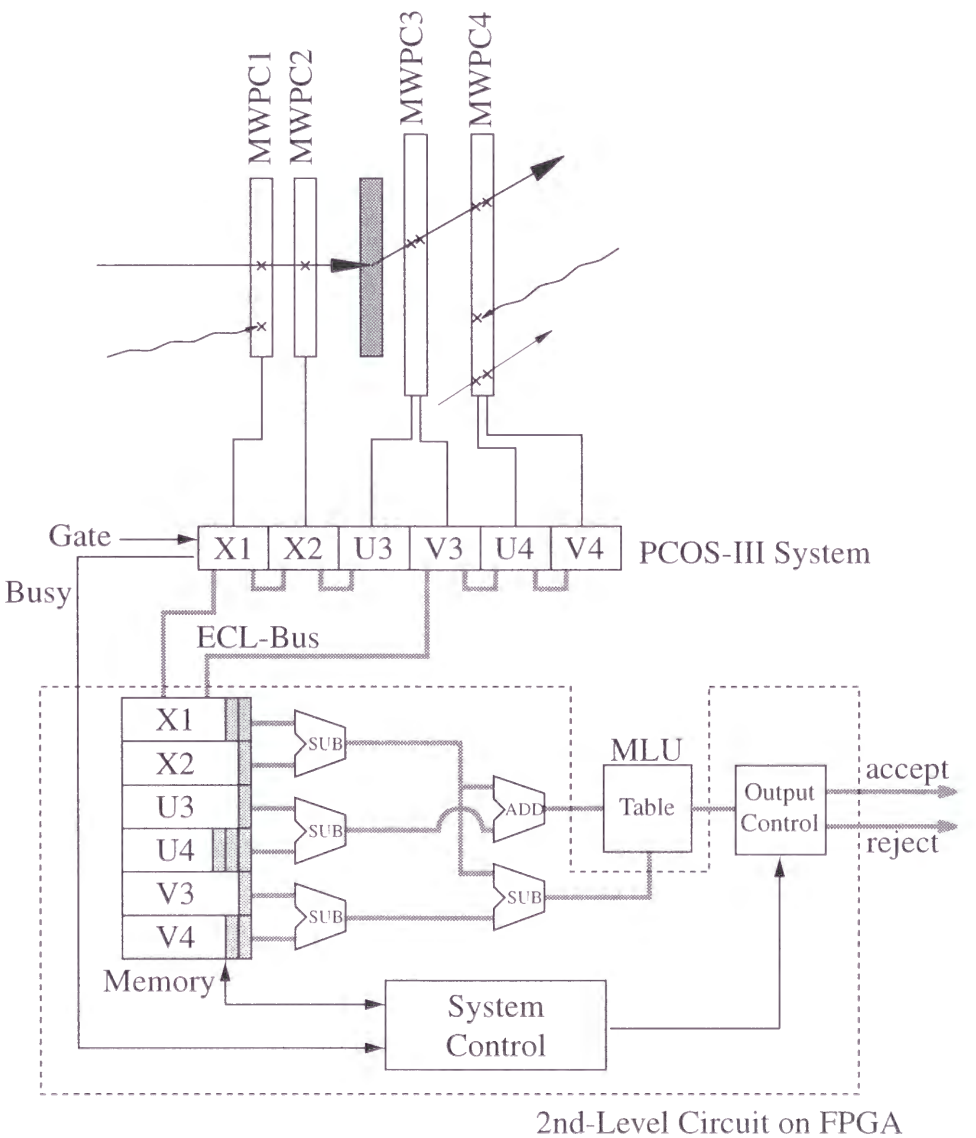

Figure 2.10: Schematic diagram of the second-level trigger system. The main part of the circuit is programmed on a FPGA (shown by the box with dashed lines).

as

$$\theta_u^{\rm in} = -\frac{1}{\sqrt{2}}\theta_x^{\rm in} = -\frac{1}{\sqrt{2}}\frac{d}{D^{\rm in}}(x_2 - x_1) \ , \tag{2.2}$$

$$\theta_v^{\rm in} = +\frac{1}{\sqrt{2}}\theta_x^{\rm in} = +\frac{1}{\sqrt{2}}\frac{d}{D^{\rm in}}(x_2 - x_1) \ . \tag{2.3}$$

The projection of the directions of the outgoing protons onto U and V planes were approximately proportional to $u_4 - u_3$ and $v_4 - v_3$, respectively, as

$$\theta_u^{\rm out} \sim \tan\theta_u^{\rm out} = \frac{d}{D^{\rm out}}(u_4 - u_3) \ , \tag{2.4}$$

$$\theta_v^{\rm out} \sim \tan\theta_v^{\rm out} = \frac{d}{D^{\rm out}}(v_4 - v_3) \ , \tag{2.5}$$

where u_3 (u_4) is the wire number hit in the U-plane of the MWPC3 (MWPC4), v_3 (v_4) is the wire number in the V-plane of the MWPC3 (MWPC4), and $D^{\rm out}$ is the distance between the MWPC3 and the MWPC4. The distance between the MWPC3 and the MWPC4 is $\sqrt{2}$ times longer than that between the MWPC1 and the MWPC2, *i.e.*

$$D^{\rm out} = \sqrt{2}D^{\rm in} \ . \tag{2.6}$$

The U and V components of the scattering angles (θ_u and θ_v)

$$\theta_u \sim \theta_u^{\rm out} - \theta_u^{\rm in} \ , \tag{2.7}$$

$$\theta_v \sim \theta_v^{\rm out} - \theta_v^{\rm in} \ , \tag{2.8}$$

are calculated from the following equations:

$$\frac{D^{\rm out}}{d}\cdot\theta_u \sim (u_4 - u_3) + (x_2 - x_1) \ , \tag{2.9}$$

$$\frac{D^{\rm out}}{d}\cdot\theta_v \sim (v_4 - v_3) - (x_2 - x_1) \ . \tag{2.10}$$

By looking up a table with the two numbers (scattered angles) as indices, the system determines whether to *accept* or *reject* each event. The table is down-loaded by CAMAC functions to the LeCroy 2372 memory look up unit. If multi-clusters occur in one or more MWPC planes, the system looks up the table for all the combinations of the clusters at the six planes. The event is rejected when the results are *reject* for all the combinations, otherwise the event is accepts.

The table is set so that the event with a scattering angle of less than 4° are rejected. The data of the horizontally scattered protons are also taken. Those data are useful to check the consistency in the azimuthal angular distribution of the scattered events, while they are useless to measure the horizontal component of the polarization.

In the experiment, the second-level trigger system reduced the trigger rate by a factor of 2.5. The trigger rate was sufficiently reduced to be handled by the data acquisition system described in the next section.

2.6 Data acquisition system

A fast data acquisition (DAQ) [48, 49] system has been developed for high rate measurements using the FPP system. A schematic view of this DAQ system is shown in Fig. 2.11. The drift time data of the VDCs are digitized by the LeCroy 3377 system and the digitized data are transfered via the ECL bus to a memory buffer in a VME system. The event header, event counter, and input register words are appended by the Flow Controlling Event Tagger (FCET) [50] modules. The hit pattern of the MWPCs are converted to the central position and the width of each cluster by the LeCroy PCOS-III system. The data are transfered to a memory buffer via a Rapid Data Transfer Module (RDTM) [51]. The RDTM transfers data from the LeCroy-bus to the ECL bus. The timing and the charge of the signals from the plastic scintillation counters are digitized by the LeCroy FERA and FERET systems. The data are also transfered to a memory module via the ECL bus.

The data conversion and the storing are performed only by hardware logics without software management nor CAMAC functions. The typical dead time for an event is less than 30 micro seconds, which is more than 20 times smaller than that of the previous CAMAC based system. The details about the DAQ system are described in Appendix D. The dead time ratio was 20% even at a 7 kHz trigger rate. In total, 350 GByte data were stored in this experiment on digital linear tapes (DLTs) and a migration system.

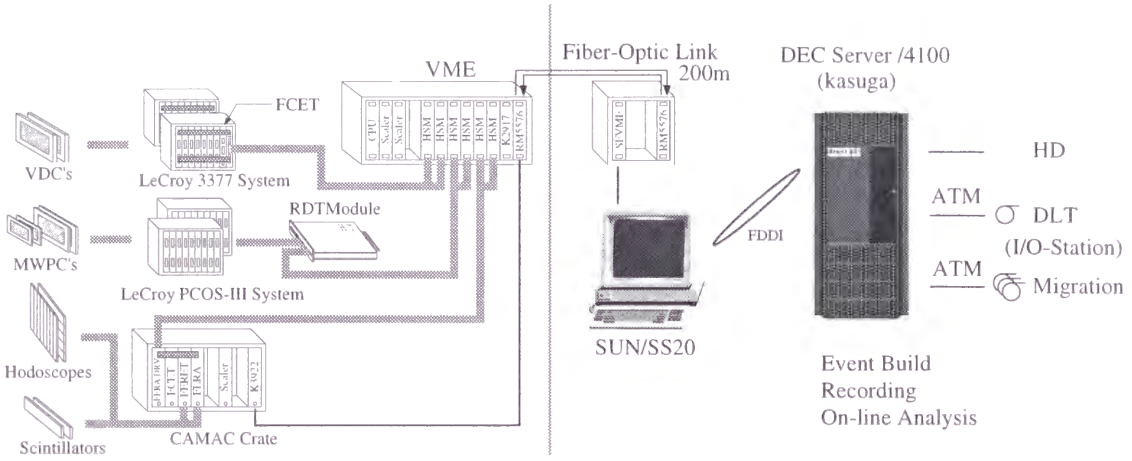

Figure 2.11: An overview of the fast data acquisition system.

2.7 Experimental Conditions

The experimental conditions are summarized in Table. 2.4 The polarized proton beam was tuned not to have any sizable halo by monitoring the trigger rate at the focal plane for the empty target frame. The beam halos were reduced mainly by adjusting the slits and Q-magnets at the injection line from the AVF cyclotron to the ring cyclotron, and the phase matching of the two cyclotrons. The three beam viewers at the focal plane in Fig. 2.5 were used for the beam tuning purpose, and were pulled off during the data acquisition. The typical FP trigger rate was 20 kHz. The FP triggers were pre-scaled by a factor of 20 to be 1 kHz and were acquired as FP sampling events. The typical FPP trigger rate was 15 kHz. The FPP trigger was reduced to 6 kHz by the second-level trigger system. The event was acquired as an FPP event. Consequently, the DAQ system acquired 6+1=7 kHz triggers with a dead time of less than 20%.

We succeeded in measuring spectra over a broad excitation energy region of 5–34 MeV, which corresponds to a very important energy region. The lowest excitation energy, 5 MeV, was achieved owing to the holes opened in the frame of the VDCs and MWPCs. By introducing a triplet quadrupole magnet in the beam line from the focal plane to the beam dump, the transmission of the beam current to the 0° Faraday cup was improved.

Table 2.4: Summary of the experimental conditions.

beam	proton	
beam energy	392	MeV
beam intensity	2-3	nA
beam polarization	0.7	
target	^{nat}C	
target thickness	30	mg/cm^2
scattering angle	0	deg.
horizontal acceptance (lab.)	$\pm$1.00	deg.
vertical acceptance (lab.)	$\pm$2.98	deg.
energy resolution	100-200	keV
carbon slab thickness	12	cm
carbon slab density	1.7	g/cm^3
FP trigger rate	20	kHz
FP sampling event rate	1	kHz
FPP trigger rate (1st level)	15	kHz
2nd-level accept event rate	6	kHz
DAQ live time	80	%
Event size	160	Byte/event
Total data f	350	GByte

The transmission was checked by comparing the beam currents measured by the 0° Faraday cup and by the Faraday cup in the scattering chamber. Since the two currents could not be measured simultaneously, the number of the events at the BLPs, which was proportional to the beam current if the accidental coincidence events were subtracted, was used for the normalization of the beam current. The transmission was 99%.

The polarization transfer data were obtained for mainly two orientations of the beam polarization in the horizontal plane in order to decompose the two PT observables, D_{SS} ($=D_{NN}$) and D_{LL}. The measured observables are summarized in Table 2.5.

Table 2.5: Summary of the measured observables.

target	thickness (mg/cm 2)	observable	scat. angle (deg)
^{nat}C	30	D_{SS} and D_{LL}	0
^{nat}C	30	$d\sigma/d\Omega$	0

Chapter 3

DATA REDUCTION AND ANALYSIS

3.1 Data reduction procedure

The analysis has been performed by using the central computer system at the RCNP. The operating system was Digital Unix V4.0 on DEC/4100 computers. The data stored in the DLTs were copied to the migration system. The three steps of the data summary tapes (DSTs) were created from the raw data according to the following scheme.

DST-1.

- Convert the hit pattern and the drift time data of the VDCs to a three dimensional trajectory before scattering at the carbon slab.
- Convert the hit pattern of the MWPCs to a three dimensional trajectory after scattering at the carbon slab.
- Select the events that have only one cluster in each VDC plane.
- Position dependent efficiency of the VDC planes were deduced.
- If the type of the event was FPP (not FP), select the events that have only one cluster in each of the MWPC planes.

DST-2.

- Select the events having the horizontal scattering angle of the first scattering in a region of interest ($-2^\circ \leq \theta \leq 2^\circ$).
- Select the events corresponding to the second scattering angle in a region of interest ($4^\circ \leq \theta_{\rm fpp} \leq 30^\circ$).

DST-3.

- Select the events corresponding only to the excitation of the specified discrete states, *i.e.* 0^+ at 7.65 MeV, 1^+, T=0 at 12.7 MeV, and 1^+, T=1 at 15.1 MeV.

The typical data size of the DST-1, DST-2, and DST-3 were 64%, 37%, and 1.7% of the raw data size, respectively.

The DST-1 were mainly used for the analysis of the double differential cross sections. The DST-2 were used to deduce the PT observables over the measured excitation energies. The DST-3 were used to deduce the PT observables for the three discrete states, to check the consistency of the analysis, to calibrate the parameters.

3.2 Analyzer Program

A general purpose analyzer program, DRED [52], has been developed for the analysis of the data obtained during this experiment.

The sequences of the analysis are specified in a description file as a list of definitions of variables. The program does the calculation of the variables for output, from other variables in the data file according to their definitions. The output of the program is considered as a DST-file. The description of the output data are automatically appended at the head of the output file, and are interpreted when the file is read to create the next DST-file. The event selection algorithm required to select meaningful events is also implemented.

The program is optimized to be capable of handling DSTs easily and flexibly. The user needs not to care the data type in the input file, but only needs to modify the definition

of the output variables and the output conditions. The obtained histograms are stored in a HBOOK [53] file and are plotted using the program PAW [54].

3.3 Polarization of the proton beam

The beam polarization was measured by two sets of beam line polarimeters as described in Sec. 2.1.2. The number of measured events corresponds to a sum of the true coincidence and the chance coincidence. The number of the chance coincidence events were counted by the coincidence of signals from one of a paired plastic scintillation counters and delayed signals from the other one. The delay time 60 nsec, which is the time interval of beam bunches. The chance events represent about 0.3% of the total events.

The x component of beam polarization ($p_x^{\rm BLP}$) and the statistical uncertainties ($\Delta p_x^{\rm BLP}$) were calculated from the following equations:

$$\begin{aligned} p_x^{\rm BLP} &= \frac{1}{A_y^{\rm BLP}} \frac{1-\alpha_x}{1+\alpha_x} , \\ \Delta p_x^{\rm BLP} &= \frac{1}{A_y^{\rm BLP}} \frac{\alpha_x}{(1+\alpha_x)^2} \sqrt{\frac{1}{D_\uparrow} + \frac{1}{U_\downarrow} + \frac{1}{D_\downarrow} + \frac{1}{U_\uparrow}} , \\ \alpha_x &\equiv \sqrt{\frac{D_\uparrow U_\downarrow}{D_\downarrow U_\uparrow}} . \end{aligned} \tag{3.1}$$

These equations can be applied both to the WN-BLP and the CAVE-BLP (see Sec. 2.1.2)

Similarly the y component of the beam polarization ($p_y^{\rm BLP}$) and the statistical uncertainties ($\Delta p_y^{\rm BLP}$) were calculated using the following equations:

$$\begin{aligned} p_y^{\rm BLP} &= \frac{1}{A_y^{\rm BLP}} \frac{1-\alpha_y}{1+\alpha_y} , \\ \Delta p_y^{\rm BLP} &= \frac{1}{A_y^{\rm BLP}} \frac{\alpha_y}{(1+\alpha_y)^2} \sqrt{\frac{1}{L_\uparrow} + \frac{1}{R_\downarrow} + \frac{1}{L_\downarrow} + \frac{1}{R_\uparrow}} , \\ \alpha_y &\equiv \sqrt{\frac{L_\uparrow R_\downarrow}{L_\downarrow R_\uparrow}} . \end{aligned} \tag{3.2}$$

The variables, $L_\uparrow$, $L_\downarrow$, represent the event numbers detected by the left (L) scintillation counters for 'up' (↑) and 'down' (↑) beam mode. The variables, $R_\uparrow$, $R_\downarrow$, $U_\uparrow$, $U_\downarrow$, $D_\uparrow$, $D_\downarrow$ are defined similarly for the right (R). up (U). and down (D) counters. respectively. The

modes, 'up' and 'down', represents the orientation of the polarization at the injection line of the AVF cyclotron.

The analyzing power for the $(p, 2p)$ inclusive scattering from a polyetherene target at 392 MeV was calibrated by measuring the asymmetry for the beam whose polarization was monitored by the beam line polarimeter, N-BLP. The N-BLP was placed at the injection line of the ring cyclotron where the beam energy was 64.2 MeV. The N-BLP detected the asymmetry during p+C elastic scattering at a laboratory angle of 47.5°. The analyzing power of the N-BLP, 0.975±0.011, was taken from Ref. 55 and 3. In the calibration measurements, the beam was tuned so that the transmission efficiency through the ring cyclotron was maximum. The obtained analyzing power is 0.44±0.02 for the polyetherene target.

The analyzing power for the polystyrene target was calibrated to that for the polyetherene target. The asymmetry for the polystyrene target at the CAVE-BLP was measured for the polarized proton beam whose polarization was monitored by the WN-BLP with the polyetherene target. The obtained analyzing power is $A_y^{\rm BLP}$=0.44±0.02 for the polystyrene target.

The three-dimensional components of the beam polarization at the reaction target have been obtained from the polarizations measured by the two BLPs using the following equations:

$$\begin{aligned} p_x^{\rm beam} &= p_x^{\rm WN} \ , \\ p_y^{\rm beam} &= p_y^{\rm WN} = p_y^{\rm CAVE} \ , \\ p_z^{\rm beam} &= \frac{p_x^{\rm WN} \cdot \cos\theta'_{\rm BLP} - p_x^{\rm CAVE}}{\sin\theta'_{\rm BLP}} \ , \\ \theta'_{BLP} &= \gamma(\frac{g_p}{2} - 1)\theta_{\rm BLP} \ , \\ \gamma &= \frac{K_p + M_p c^2}{M_p c^2} \ , \end{aligned} \tag{3.3}$$

where $p_x^{\rm beam}$, $p_y^{\rm beam}$, and $p_z^{\rm beam}$ represent the x, y, and z components of the polarization at the reaction target, respectively. $p_x^{\rm WN}$ ($p_x^{\rm CAVE}$) and $p_y^{\rm WN}$ (p_y^{CAVE}) denote the x and y component of the beam polarization at the WN-BLP (CAVE-BLP) deduced from Eqs. 3.1

and 3.2, respectively. $\theta_{\rm BLP}$ (=50°) is the relative angle of the two BLPs (see Fig. 2.3), $g_p = 5.585$ is the gyromagnetic ratio (g-factor) of protons, $K_p = 392$ MeV is the kinetic energy of the proton beam, and M_p is the proton rest mass. Sec. B.1 describes in details the precession of a polarization vector in a magnetic field.

The horizontal component of the polarization was about 0.65–0.78. The vertical component of the polarization was typically less than 0.03, and 0.10 for the worst case. The magnitude and the orientation of the beam polarization were stable during the experiment.

3.4 Plastic scintillation counters and hodoscope-X

The plastic scintillation counter (PS1), placed downstream of the VDC's, was used to create trigger signals. The mean time of the signals from the PMTs on both sides of the PS1 was the reference point of all the acquired timing information. The charge information from the PMTs was used to identify the particle which triggered the event. The energy loss of a charged particle passing through material depends on its charge and velocity as described by the Bethe-Bloch equation (see Eq. 3.32 and Ref. 56).

The light intensity at the x position is given by

$$I(x) = I_0 \exp\{-x/l\}, \tag{3.4}$$

where I_0 is the light intensity where the particle passes, and l is the attenuation length of the scintillator. The energy loss, $E_{\rm loss}$ ($\propto I_0$), is related to the square root of the product of the light outputs from both sides of the scintillation counter:

$$I_m \equiv \sqrt{I(x)I(L-x)} = I_0 \exp\{-L/2l\} \propto E_{\rm loss} \tag{3.5}$$

where L is the length of the scintillator. A histogram of I_m is plotted in Fig. 3.1 for (p,p') scattering at 8°. A rough gate was set for protons from 100 to 300 channels. In the 0° measurement the deuteron peak was not observed.

The plastic scintillator (PS2) on the carbon slab was also used for generating the trigger

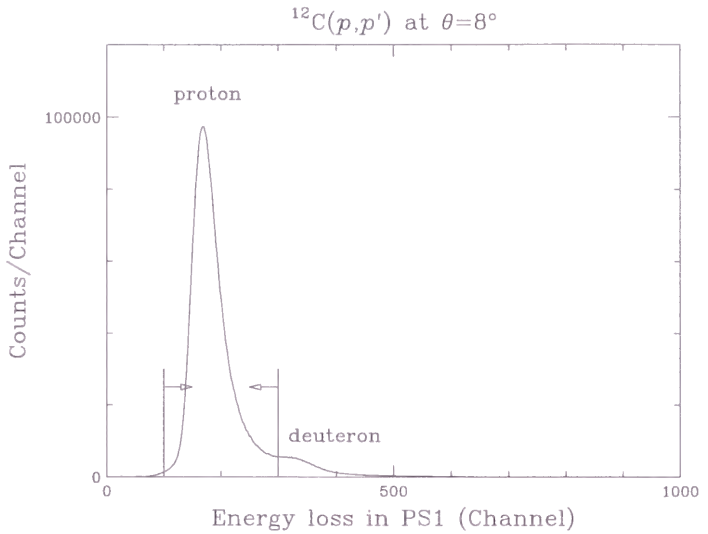

Figure 3.1: Energy loss in the PS1 in the $^{12}C(p, p')$ reaction at 8° deduced by the square root of the product of the charge outputs from the PMTs on both sides. A gate for the proton events was set in a range of 100–300 channels as shown in the figure.

signals. The light output of the PS2 was detected only from the low momentum side in order not to interfere with the primary beam duct. It was confirmed that the signal at the high momentum edge of PS2 was large enough to generate trigger signals.

The plastic scintillators of the HD-X were used for generating the FPP triggers. The charge and time information was digitized and recorded. No cut was applied to the HD-X data in the analysis.

3.5 Multiwire drift chambers

Fig. 3.2 illustrates the structure of the multiwire drift chambers of vertical drift type (VDCs). A voltage of -5700 V was applied to the cathode planes and a voltage of -300 V to the potential wires in order to reach high efficiency. The sense wires were distant of 4mm (X-planes) or 6 mm (U-planes) and were kept at the ground voltage. When a charged particle passes through the VDC, electron-ion pairs are created along the trajectory. The electrons move to an anode wire in the normal direction to the

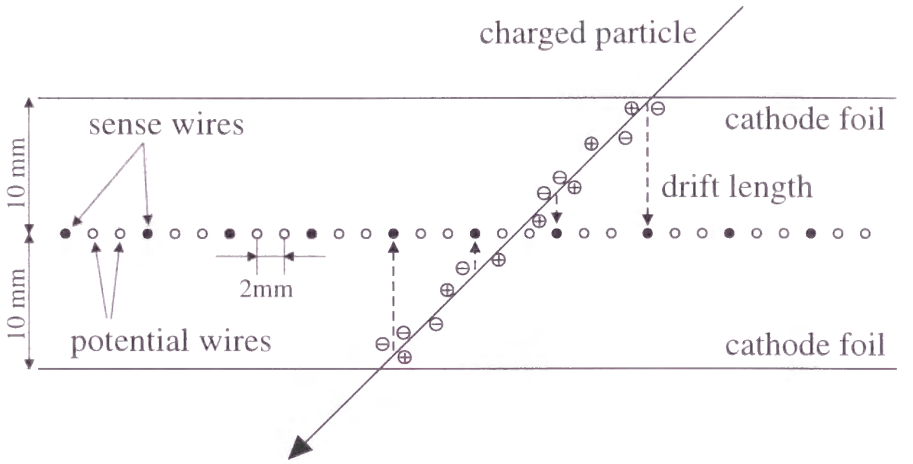

Figure 3.2: Structure of the VDCs (U-Plane).

cathode planes by the force of the electric field. The mobility has an almost constant value of ~50 μm/nsec. The electrons are multiplied at the place close to the anode wire, and generate a negative signal at the anode wire. Usually particles pass through the VDCs in the 45° direction and hit 3 or 4 sense wires. In the case of the excitation of continuum energy region, no sharp peak is observed in the position histogram. The drift length histogram should, therefore, have a flat distribution in a range of 0–10 mm. The conversion tables from the drift time to the drift length have been created from the data of continuum excitation so that the drift length histogram has a flat distribution (Fig. 3.3).

The adjacent hit wires are grouped as a cluster. The intercept position of a trajectory at a wire plane is calculated by a least-square fit method from the drift lengths of the hit wires in the cluster. By combining the deduced positions at the four wire planes the trajectory is uniquely determined. The following rules are applied in the determination of the trajectory.

- A cluster has at least two hit wires. A single hit wire is not considered as a cluster and ignored.

- The distribution of the drift lengths in a cluster has only one local minimum which

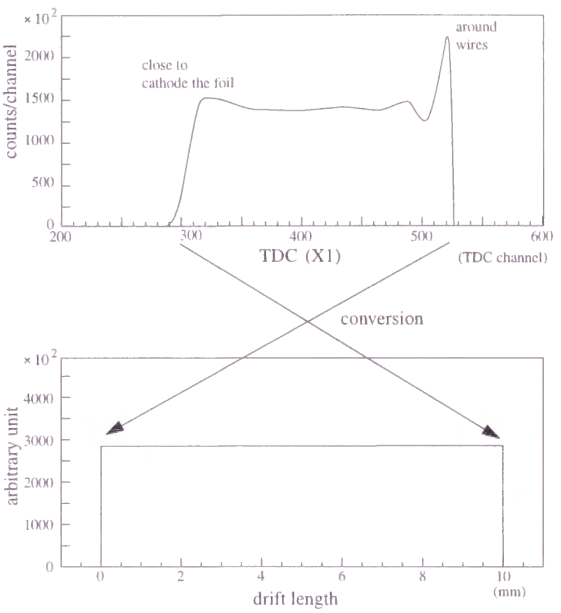

Figure 3.3: Conversion of the timing spectrum of the sense wires of the VDCs to the drift length.

is not at the edge of the cluster.

- The number of clusters in each plane is one.

The position resolution was about 0.29 mm in full width at half maximum (FWHM). It corresponds to the energy resolution of 29 keV/mm × 0.29 mm = 8.4 keV, which was good enough compared with the energy resolution of the beam (≥100 keV in FWHM). The resolution of the incidence angle was $\tan^{-1}(0.29/250) = 0.066°$, which corresponds to a horizontal scattering angle of 0.028° at the target.

The efficiency of the VDC's has been determined by the following scheme. In order to obtain the efficiency of the X1 and U1 planes, the trajectory of a proton is determined from the data of the X2 and U2 planes. The trajectory is traced back to the focal plane, and the excitation energy for the proton is roughly determined. The efficiency of the X1 (U1) plane $\epsilon_X 1(E_x, E_x + dE_x)$ ($\epsilon_U 1(E_x, E_x + dE_x)$) in a region of the excitation energy

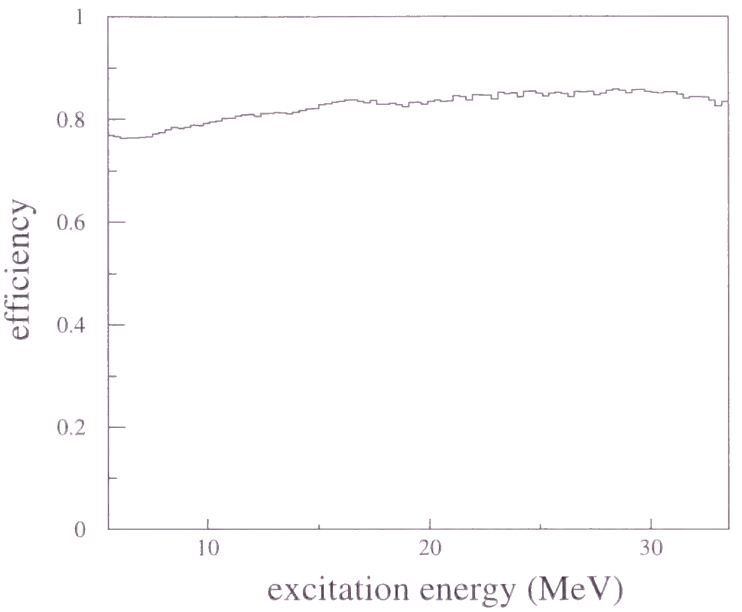

Figure 3.4: Overall efficiency of the VDCs for all the four planes versus excitation energy.

from E_x to $E_x + dE_x$ is calculated from the following equations:

$$\begin{aligned} \epsilon_{X1}(E_x, E_x + dE_x) &= \frac{N_{X1U1}(E_x, E_x + dE_x)}{N_{U1}(E_x, E_x + dE_x)}, \\ \epsilon_{U1}(E_x, E_x + dE_x) &= \frac{N_{X1U1}(E_x, E_x + dE_x)}{N_{X1}(E_x, E_x + dE_x)}, \end{aligned} \tag{3.6}$$

where $N_{X1}(E_x, E_x + dE_x)$, $N_{U1}(E_x, E_x + dE_x)$, and $N_{X1U1}(E_x, E_x + dE_x)$ denotes the number of the events in which the position of the proton can be determined in the X1, V1, and both X1 and V1 planes, respectively. The efficiency of the X2 and U2 planes is determined in a similar way by exchanging X1 with X2, and U1 with U2. The obtained efficiencies are about 93∼97 % per plane. Fig. 3.4 shows the total efficiency obtained by multiplying the efficiency of all the four planes. The efficiency decreases gradually as the excitation energy decreases. This tendency is due to the high amount of background particles generated by scattering of the primary beam at the beam duct or the exit flange. The beam duct is placed close to the low excitation energy region of the VDCs. After a particle passes through the chamber, the electric field is effectively lowered until created ions move to the cathode foils. The mobility of ions is typically 1000 times lower than that of electrons. Therefore, the efficiency decreases when the rate of the passing charged

particles increases.

3.6 Acceptance of the Grand Raiden spectrometer

The scattering angle in the acceptance of the spectrometer was calibrated by measuring the p+Si elastic scattering at θ=18.1°, where the differential cross section is maximum. In the case of the 0° experiments, the DSR magnet of the Grand Raiden was utilized to adjust precisely the direction of the primary beam to the beam line to the Faraday Cup. In the calibration, the magnetic field of the spectrometer was scaled to the p+Si elastic measurement based on the setting for the 0° experiments.

The relation between the horizontal scattering angle and the horizontal incidence angle at the focal plane was calibrated by measuring the elastic data for several settings of the horizontal entrance slit of the spectrometer. The direction of the central ray, which was used as the reference point of 0° in the 0° experiments, was also calibrated. The systematic uncertainty in the determination of the horizontal scattering angle was estimated as 0.02° in the laboratory frame.

The vertical acceptance was determined by comparing the number of scattering events for several setting of the vertical entrance slit of the spectrometer. The dependence on the orbit radius (ρ) was determined by using the events of elastic scattering events, excitation of the 2^+ state at 1.78 MeV, the $4^+ + 0^+$ states around 4.8 MeV, and the $3^- + 4^+ + 2^+ + 2^+$ states around 7 MeV. The averaged value was used as the acceptance in the vertical direction. The deviations, resulted from the *ryo* dependence, were ±3.4%. The deviations were treated as a systematic uncertainty of the vertical acceptance.

In the 0° experiments, the entrance slits were fully opened to avoid background events due to the edge scattering and the (p, n)-(n, p) sequential reactions at the slits. The off-line analysis used the events with the horizontal scattering angle in a range of ±1.00° in the laboratory frame (±1.12° in the c.m. frame) with a systematic uncertainty of 0.02°. For the vertical direction the full acceptance of the spectrometer, which was ±2.98° in

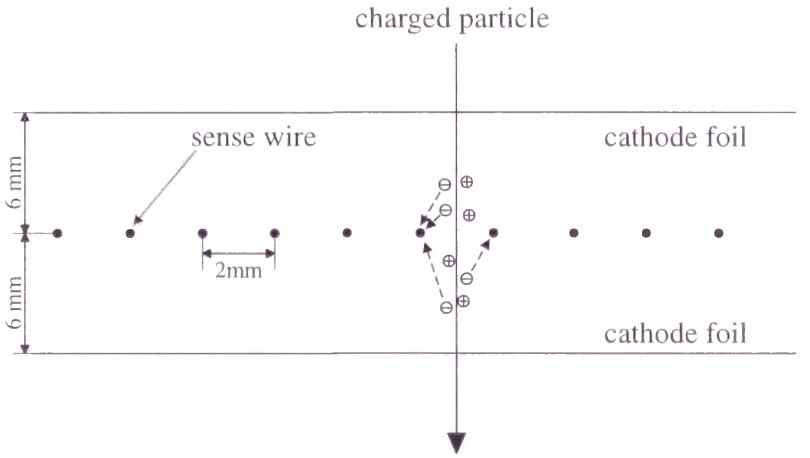

Figure 3.5: Structure of the MWPCs.

the laboratory frame (±3.35° in the c.m. frame) with a systematic uncertainty of 0.10°, was used. As a result, the solid angle for the analyzed events was 3.63±0.14 msr in the laboratory frame and 4.53±0.18 msr in the c.m. frame. The energy dependence of the Jacobian for the lab.–c.m. transformation in the momentum acceptance of the spectrometer was less than 0.4%, and was neglected.

3.7 Multiwire proportional chambers

Fig. 3.5 illustrates the structure of the multiwire proportional chambers (MWPC's). In contrast to the case of the VDCs, all the anode wires were read out and the drift times were not measured. The signals from the anode wires were amplified and discriminated by amplifier/discriminator cards of LeCroy 2735PC and Nanometric N277-C3 A LeCroy PCOS-III system clusterizes the hit patterns of the anode wires, and transfered the data of the central position and the width of each cluster.

The data of the MWPC have been analyzed according to the following event selection rule:

- Number of the clusters for each plane is one.

The position resolution of the MWPC with a wire spacing of d=2 mm is $d/\sqrt{(12)} \sim$ 0.58 mm in root mean square and ~1.4 mm in FWHM. The actual resolution is slightly better than the value because adjacent two wires can be hit when a particle passes around the middle of the wires. The trajectory of charged particles is determined by combining the positions at four wire planes. The incidence angle resolution is estimated to be $\tan^{-1}(\sqrt{2} \times 2/359.5) = 0.45°$. The hit patterns of the X1 and X2 planes were used by the second-level trigger system. Since the VDCs had much better resolution for the incidence angle than the X1 and X2, the data were not used in the off-line analysis.

The consistency of the position and the incidence angle at the VDCs and MWPCs has been checked by the events acquired without the carbon slab. The rotation of VDC's along the y-axis and the z-axis was adjusted so that the trajectory determined by the VDCs became parallel to that determined by the MWPCs. The uncertainty of the rotation angle was less than 0.080 degrees. The x and y positions of the MWPCs were adjusted so that the hit position of the MWPCs agreed with the position calculated by using the trajectory determined by the VDCs. The discrepancy of the positions were less than 2 mm over all the acceptance of the MWPCs. The discrepancy is negligible for deducing the asymmetry during the second scattering. The measured values are used for the z positions of the VDCs and the MWPCs

3.8 Scattering angle at the carbon slab

The scattering angle of the protons at the carbon slab has been deduced from the trajectories determined by the VDCs and the MWPCs. We define a cartesian coordinate system, in which $\hat{z}$ is in the direction of the central ray, $\hat{y}$ is in the upward vertical direction, and $\hat{x}$ is $\hat{x} = \hat{y} \times \hat{z}$. Suppose $\hat{k}_i$ is the unit vector of the trajectory determined by the VDCs, and $\hat{k}_f$ is the unit vector of the trajectory determined by the MWPCs.

At first the rotation angles α and β are determined from the equation

$$\hat{z} = R_x(\beta)R_y(\alpha)\hat{k}_i \ , \tag{3.7}$$

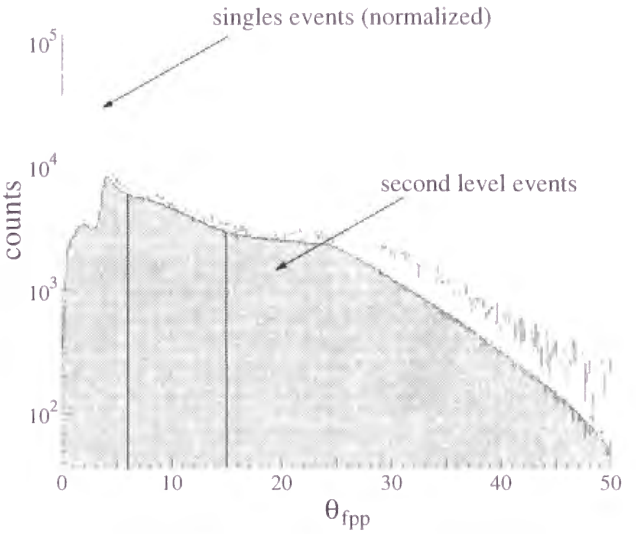

Figure 3.6: Scattering angle at the carbon slab for the FP sampling events (normalized by the sampling rate) and for the second-level accept events. The data with a scattering angle in a region of 6–15° are used in the analysis.

where $R_i(\theta)$ is a usual 3-dimensional rotation operator for the angle θ along the i axis. A unit vector $\hat{k}$ is calculated by the equation

$$\hat{k} = R_x(\beta)R_y(\alpha)\hat{k}_f. \tag{3.8}$$

The polar angle $\theta_{\rm fpp}$ from the z axis and the azimuthal angle $\phi_{\rm fpp}$ from the x axis for the scattering are determined from the equations

$$\begin{aligned} \cos\theta_{\rm fpp} &= \hat{k}\cdot\hat{z}\ , \\ \cos\phi_{\rm fpp} &= -\hat{\ell}\cdot\hat{y}\ , \\ \sin\phi_{\rm fpp} &= \hat{\ell}\cdot\hat{x}\ , \\ \hat{\ell} &\equiv \frac{\hat{k}\times\hat{z}}{|\hat{k}\times\hat{z}|}\ . \end{aligned} \tag{3.9}$$

The $\theta_{\rm fpp}$ distribution of the scattered events is shown in Fig. 3.6 for the FP sampling events and for the second-level accept events. The FP sampling events are normalized by the sampling rate. The hatched area shows the events accepted by the second-level trigger system. The events which have a scattering angle of less than 4° are efficiently

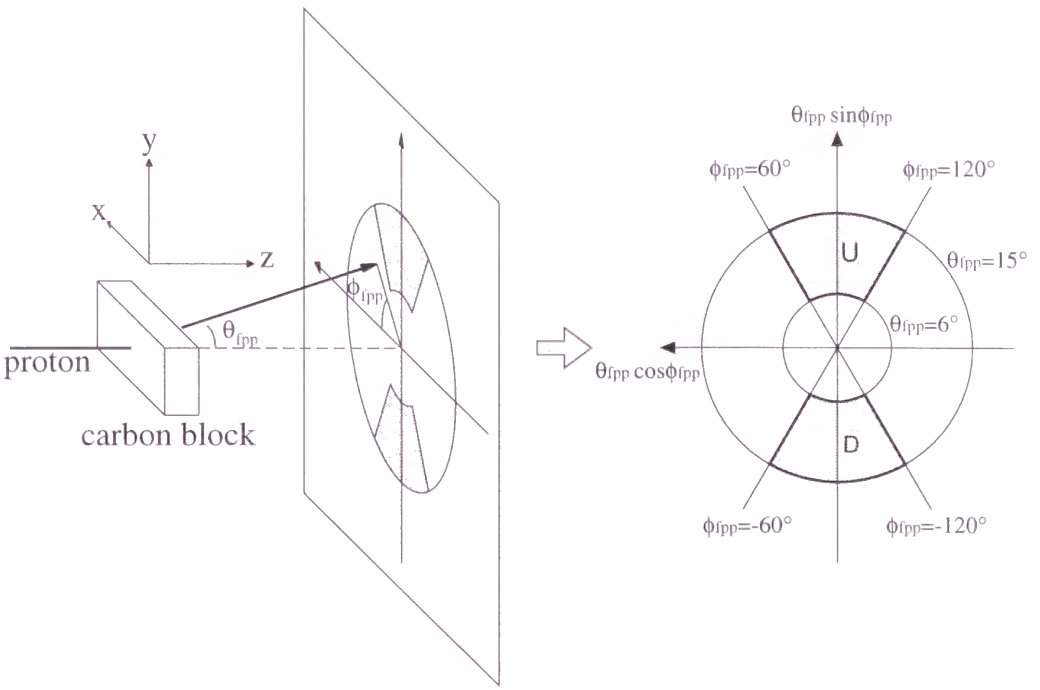

Figure 3.7: Coordinate system used in the analysis of the scattering angles. The hatched regions are the integration area to deduce the polarization of the scattered particles.

rejected. The remaining events with a scattering angle of less than 4° are due to the large vertical incidence angle, which is assumed to be zero in the calculation of the second-level trigger system. The events in an angular range of 6–15° are used to deduce the polarization of the protons.

3.9 Polarization of scattered protons

The sideway polarization of the scattered protons are deduced from the following equations:

$$
\begin{aligned}
p_x^{\mathrm{fpp}} &= \frac{1}{\langle A_y \rangle^{\mathrm{fpp}}} \frac{1-\alpha^{\mathrm{fpp}}}{1+\alpha^{\mathrm{fpp}}} , \\
\Delta p_x^{\mathrm{fpp}} &= \frac{1}{\langle A_y \rangle^{\mathrm{fpp}}} \frac{\alpha^{\mathrm{fpp}}}{(1+\alpha^{\mathrm{fpp}})^2} \sqrt{\frac{1}{N_D^{\uparrow}} + \frac{1}{N_D^{\downarrow}} + \frac{1}{N_U^{\uparrow}} + \frac{1}{N_U^{\downarrow}}} , \\
\alpha^{\mathrm{fpp}} &\equiv \sqrt{\frac{N_D^{\uparrow} N_U^{\downarrow}}{N_D^{\downarrow} N_U^{\uparrow}}} ,
\end{aligned}
\tag{3.10}
$$

where $N_U^{\uparrow}$ and $N_D^{\uparrow}$ are defined as the number of the events which have the scattering angle in the area of U and D, respectively, for the 'up'-mode beam. $N_U^{\downarrow}$ and $N_D^{\downarrow}$ are defined similarly for the 'down'-mode beam. The U and D areas are shown in Fig. 3.7. $\langle A_y \rangle^{\rm fpp}$ is the effective analyzing power of the FPP for the specified U and D areas. The way to determine the areas and the value of $\langle A_y \rangle^{\rm fpp}$ are described in the next section.

3.10 Effective analyzing power of the FPP

As polarimetries, p+C elastic, inelastic, and quasi-free scatterings are inclusively measured. In general, the differential cross sections, $\frac{d\sigma}{d\Omega}(\theta, \phi)$, to the direction specified by θ (polar angle) and ϕ (azimuthal angle) are expressed as

$$\begin{aligned} \frac{d\sigma}{d\Omega}(\theta, \phi) &= \frac{d\sigma}{d\Omega}(\theta)\{1 - p_\perp A_y(\theta)\sin(\phi - \phi_p)\} , \\ \frac{d\sigma}{d\Omega}(\theta) &\equiv \frac{d\sigma}{d\Omega}(\theta, \phi_p) . \end{aligned} \tag{3.11}$$

where $p_\perp$ is the magnitude of the polarization perpendicular to the z-axis, and ϕ_p is the azimuthal angle of the polarization vector perpendicular to the z axis from the x-axis. By using $\frac{d\sigma}{d\Omega}(\theta, \phi)$, the scattering asymmetry for the D and U regions is written by

$$\begin{aligned} \text{Asym} &\equiv \frac{N_D - N_U}{N_D + N_U} \\ &= \frac{\int_{D-U} d\Omega \frac{d\sigma}{d\Omega}(\theta)\{1 - p_\perp A_y(\theta)\sin(\phi - \phi_p)\}}{\int_{D+U} d\Omega \frac{d\sigma}{d\Omega}(\theta)\{1 - p_\perp A_y(\theta)\sin(\phi - \phi_p)\}} \\ &= \frac{\int d\theta \sin\theta \frac{d\sigma}{d\Omega}(\theta) \int_{\phi_D - \phi_U} d\phi\{1 - p_\perp A_y(\theta)\sin(\phi - \phi_p)\}}{\int d\theta \sin\theta \frac{d\sigma}{d\Omega}(\theta) \int_{\phi_D + \phi_U} d\phi\{1 - p_\perp A_y(\theta)\sin(\phi - \phi_p)\}} . \end{aligned} \tag{3.12}$$

We express $\int_D d\Omega + \int_U d\Omega$ as $\int_{D+U} d\Omega$ for convenience. By using the following relation

$$\begin{aligned} \int_{\phi_U} d\phi\{1 - p_\perp A_y(\theta)\sin(\phi - \phi_p)\} &= \int_{\frac{\pi}{2} - \Delta\phi}^{\frac{\pi}{2} + \Delta\phi} d\phi\{1 - p_\perp A_y(\theta)\sin(\phi - \phi_p)\} \\ &= \int_{-\Delta\phi}^{\Delta\phi} d\phi\{1 - p_\perp A_y(\theta)\cos(\phi - \phi_p)\} , \\ \int_{\phi_D} d\phi\{1 - p_\perp A_y(\theta)\sin(\phi - \phi_p)\} &= \int_{-\frac{\pi}{2} - \Delta\phi}^{-\frac{\pi}{2} + \Delta\phi} d\phi\{1 - p_\perp A_y(\theta)\sin(\phi - \phi_p)\} \\ &= \int_{-\Delta\phi}^{\Delta\phi} d\phi\{1 + p_\perp A_y(\theta)\cos(\phi - \phi_p)\} , \end{aligned} \tag{3.13}$$

the integrals in Eq. 3.12 are modified as

$$\begin{aligned}
\int_{\phi_D+\phi_U} d\phi\{1 - p_\perp A_y(\theta)\sin(\phi-\phi_p)\} &= \int_{-\Delta\phi}^{\Delta\phi} 2d\phi = 4\Delta\phi \ , \\
\int_{\phi_D-\phi_U} d\phi\{1 - p_\perp A_y(\theta)\sin(\phi-\phi_p)\} &= \int_{-\Delta\phi}^{\Delta\phi} d\phi\{2p_\perp A_y(\theta)\cos(\phi-\phi_p)\} \\
&= 4p_\perp \cos(\phi_p)\sin(\Delta\phi)A_y(\theta) \ . \qquad (3.14)
\end{aligned}$$

Then we obtain

$$\text{Asym} = p_\perp \cos(\phi_p)\frac{\sin(\Delta\phi)}{\Delta\phi}\frac{\int d\theta \sin\theta \frac{d\sigma}{d\Omega}(\theta)A_y(\theta)}{\int d\theta \sin\theta \frac{d\sigma}{d\Omega}(\theta)} \ . \qquad (3.15)$$

By defining effective analyzing power $\langle A_y\rangle^{\text{fpp}}$ as

$$\langle A_y\rangle^{\text{fpp}} \equiv \frac{\sin(\Delta\phi)}{\Delta\phi}\frac{\int d\theta \sin\theta \frac{d\sigma}{d\Omega}(\theta)A_y(\theta)}{\int d\theta \sin\theta \frac{d\sigma}{d\Omega}(\theta)} \ , \qquad (3.16)$$

the x component of the polarization is written as

$$p_x = p_\perp \cos(\phi_p) = \frac{\text{Asym}}{\langle A_y\rangle^{\text{fpp}}} \ . \qquad (3.17)$$

The effective analyzing power, $\langle A_y\rangle^{\text{fpp}}$, is expressed by the value ($\langle A_y\rangle^{\text{fpp}}_{\Delta\phi=0}$) at the limit of $\Delta\phi \to 0$ as

$$\begin{aligned}
\langle A_y\rangle^{\text{fpp}} &= \frac{\sin\Delta\phi}{\Delta\phi}\langle A_y\rangle^{\text{fpp}}_{\Delta\phi=0} \ , \\
\langle A_y\rangle^{\text{fpp}}_{\Delta\phi=0} &= \frac{\int d\theta \sin\theta \frac{d\sigma}{d\Omega}(\theta)A_y(\theta)}{\int d\theta \sin\theta \frac{d\sigma}{d\Omega}(\theta)} \ . \qquad (3.18)
\end{aligned}$$

The above equation holds for each 'up' and 'down' beam mode.

In practical analyses, the data for both 'up' and 'down' beam modes are combined to cancel false asymmetries of the detector system. For this purpose, we define a modified asymmetry as

$$\begin{aligned}
\text{Asym}' &\equiv \frac{1-\alpha^{\text{fpp}}}{1+\alpha^{\text{fpp}}}, \\
\alpha^{\text{fpp}} &\equiv \sqrt{\frac{N_D^\uparrow N_U^\downarrow}{N_D^\downarrow N_U^\uparrow}} \ . \qquad (3.19)
\end{aligned}$$

If the polarization of the beam completely flips for the 'up'- and 'down'-mode, the polarization of the scattered protons also completely flips at the scattering angle of 0°.

It is because the analyzing power A_N and the induced polarization P_N is zero at 0° in Eq. C.22. At small scattering angles, A_N and P_N can be approximated to be proportional to the scattering angle. Therefore, if Eq. C.22 is averaged in a finite solid angle which is symmetric around 0°, the averaged polarization of the scattered particles completely flips in the first order of the maximum scattering angle. The spin-flip condition can be written in the form

$$p_\perp^\uparrow = p_\perp^\downarrow . \tag{3.20}$$

$$\phi_p^\uparrow = \pi + \phi_p^\downarrow . \tag{3.21}$$

Then we obtain

$$N_U^\downarrow = \int_U d\Omega \frac{d\sigma}{d\Omega}(\theta)\{1 - p_\perp A_y(\theta)\sin(\phi - \phi_p^\downarrow)\} \tag{3.22}$$

$$= \int_D d\Omega \frac{d\sigma}{d\Omega}(\theta)\{1 - p_\perp A_y(\theta)\sin(\phi - \phi_p^\downarrow)\} \tag{3.23}$$

$$= N_D^\downarrow . \tag{3.24}$$

and similarly

$$N_U^\downarrow = N_D^\uparrow . \tag{3.25}$$

The following equations can be deduced:

$$\mathrm{Asym}' = \mathrm{Asm}^\uparrow = -\mathrm{Asm}^\downarrow . \tag{3.26}$$

$$p_x = p_x^\uparrow = -p_x^\downarrow = \frac{\mathrm{Asym}'}{\langle A_y \rangle^{\mathrm{fpp}}} . \tag{3.27}$$

Thus the sideway component of the polarization can be determined from the above analysis even if the vertical polarization of the scattered particles is non-zero, *i.e.* the vertical polarization of the beam is non-zero. This is one of the properties of the measurement at zero degrees.

In order to choose the most efficient integration areas, U and D, we examine figure of merit (FOM). The FOM is defined as [57]

$$\mathrm{FOM} \equiv \eta(\langle A_y \rangle^{\mathrm{fpp}})^2 . \tag{3.28}$$

Here η is the efficiency of the polarimeter, which is defined as

$$\eta \equiv \frac{\text{number of detected events}}{\text{number of incident particles}}. \tag{3.29}$$

In our case η is proportional to the number of the events which are used to deduce the polarization, *i.e.*

$$\eta \propto \int_{U+D} \frac{d\sigma}{d\Omega}(\theta) d\Omega \ . \tag{3.30}$$

The FOM is inversely proportional to the square of the statistical uncertainty for the events acquired in a time interval. Therefore, the U and D areas are usually determined as the FOM takes the maximum. The FOM depends on the $\Delta\phi$ value as

$$\begin{aligned} \text{FOM} &\propto \int_{U+D} d\Omega \frac{d\sigma}{d\Omega}(\theta) \cdot (\langle A_y \rangle^{\text{fpp}})^2 \\ &\propto \frac{\sin^2(\Delta\phi)}{\Delta\phi}. \end{aligned} \tag{3.31}$$

The FOM takes the maximum at $\Delta\phi = 66.78°$, where the equation, $\tan\Delta\phi{=}2\Delta\phi$, holds. The most suitable θ range (from θ_{min} to θ_{max}) depends on the angular distribution of $\frac{d\sigma}{d\Omega}(\theta)$. Typically the θ range is taken as 5–20°. In this experiment the acceptance of the FPP does not cover the θ region of 5–20° for all the momentum acceptance of the spectrometer and for the $\Delta\phi$ of 66.78°. The U and D regions are determined as $\Delta\phi = 30°$ for the excitation below 15 MeV, $\Delta\phi = 66.8°$ for the excitation above 15 MeV, and $(\theta_{\text{min}}, \theta_{\text{max}}){=}(6°, 15°)$ for all the excitation energies.

The value of the effective analyzing power of the FPP is determined by the following scheme according to Ref. 58. The energy of the protons at the center of the carbon slab, E_p^c, is calculated by numerical integration of the energy loss per unit thickness described by the Bethe-Bloch equation [56] as

$$-\frac{dE}{dx} = 2\pi N_a r_e^2 m_e \frac{Z}{A}\frac{z^2}{\beta^2}\left[\ln\frac{2m_e\gamma^2\beta^2 W_{max}}{I^2} - 2\beta^2 - \delta - 2\frac{C}{Z}\right] \quad (\text{MeVg}^{-1}\text{cm}^{-2}). \tag{3.32}$$

For details of the definitions variables. see Ref. 56. $I = 78.0$ eV is used for mean excitation potential from Ref. 59. A value of $\delta = 0.121$ was used for the density correction. The shell correction term is estimated to be about $C = 0.0446$ and negligible. For example.

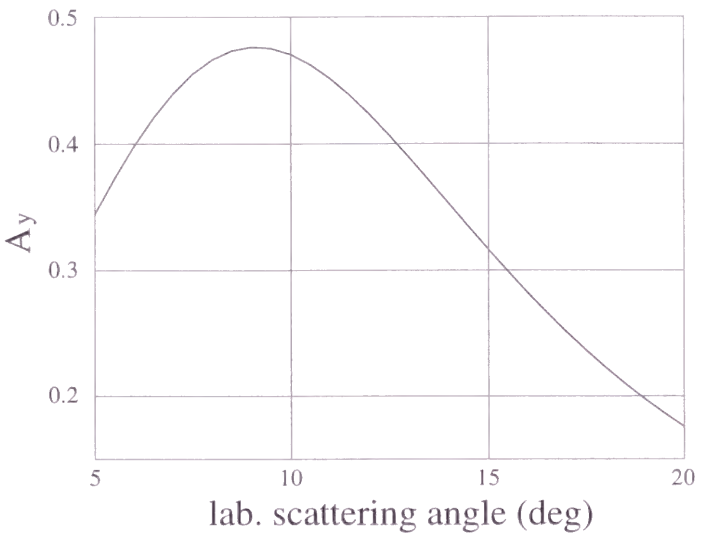

Figure 3.8: Analyzing power of p+C inclusive scattering at E_p^c=363 MeV from the equation by McNaughton *et al.* For details, see text.

the energy loss of the 392 MeV protons in a carbon slab with a thickness of 6 cm and a density of 1.73 g/cm^3 is calculated as 28.9 MeV. The p+C inclusive analyzing power for each proton energy at the center of the carbon slab is calculated from the empirical energy dependent fit by McNaughton *et al.* [58]. Fig. 3.8 plots the calculated analyzing power as a function of the scattering angle in the laboratory frame for E_p=363 MeV protons. The angular distribution of the differential cross sections are taken from the data of this experiment. The upper curve denoted by 'singles events' in Fig. 3.6 is proportional to $\frac{d\sigma}{d\Omega}(\theta_f pp) \cdot \sin\theta_{\rm fpp}$. The effective analyzing power has been obtained by a numerical integration of Eq. 3.16. Similar calculations are performed for several energies. The calculated values have been fitted by a second order polynomial of the excitation energy. The obtained function is written as

$$\langle A_y \rangle^{\rm fpp}_{\Delta\phi=0} = 0.432 + 1.10 \times 10^{-3} E_x + 2.84 \times 10^{-6} E_x^2 \tag{3.33}$$

and plotted in Fig. 3.9. The effective analyzing power of the FPP for a given $\Delta\phi$ has been calculated from Eq. 3.18. The obtained values are summarized in Table 3.1.

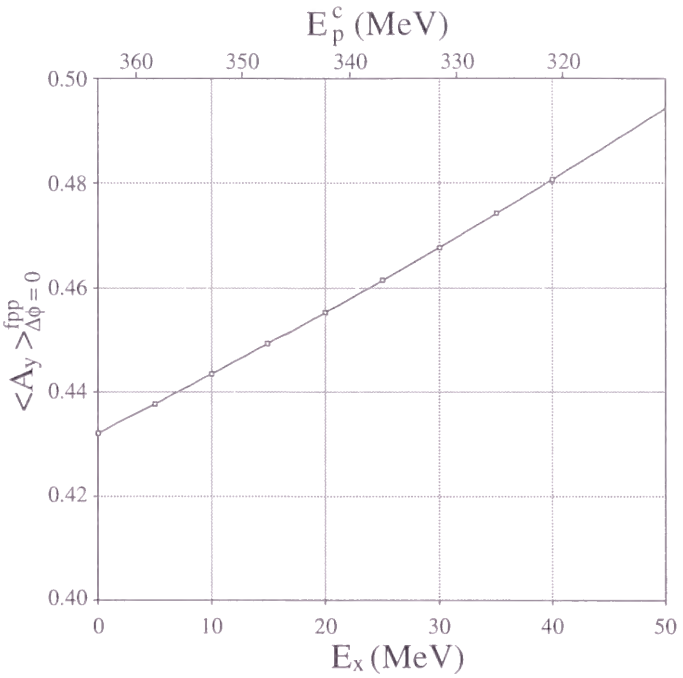

Figure 3.9: Effective analyzing power of the FPP for $\Delta\phi = 0$ versus excitation energy. The upper axis represents the energy of the protons at the center of the carbon slab with a thickness of 12 cm.

3.11 Background subtraction

Although we have succeeded in reducing the background arising from the beam halo, background still remains resulting mainly from multiple scattering of the beam on the targets. The background events have been subtracted from excitation spectra by the following scheme. From the ion-optical features of the *Grand Raiden* spectrometer, true events, *i.e.* inelastically scattered protons, were focused at the focal plane not only in the horizontal direction but also in the vertical direction. In contrast, background due to the multiple scattering at the target and re-scattering in the spectrometer had a flat distribution in the histogram of the vertical (y) position at the focal plane. The vertical position histogram is shown in Fig. 3.10 for the excitation of the 1^+, T=0 state at 12.7 MeV. The spectrum has been obtained by a sum of the histograms of 23 data runs. The peak position of the y histogram for the excitation of the 1^+, T=1 state at

Table 3.1: Energy of protons at the center of the carbon slab and effective analyzing power of the FPP as a function of the excitation energy.

E_X (MeV)	E_p (MeV)	E_p^c (MeV)	$\langle A_y \rangle^{\rm fpp}_{\Delta\phi=0}$	$\langle A_y \rangle^{\rm fpp}_{\Delta\phi=30.0}$	$\langle A_y \rangle^{\rm fpp}_{\Delta\phi=66.8}$
0	392	363.14	0.4322	0.4127	0.3407
5	387	357.93	0.4378	0.4181	0.3451
10	382	352.71	0.4435	0.4235	0.3496
15	377	347.48	0.4493	0.4291	0.3542
20	372	342.25	0.4553	0.4348	0.3590
25	367	337.00	0.4615	0.4407	0.3638
30	362	331.73	0.4676	0.4465	0.3688
35	357	326.45	0.4742	0.4528	0.3738
40	352	321.16	0.4807	0.4590	0.3790

15.1 MeV has been adjusted to be at y=0 for each run. The histogram is an overlay of the true peak at y=0 and a background trapezoid. The background has a flat distribution in the region of interest. In the analysis of the PT observables, the middle hatched region ($-3.0 \leq y \leq 3.0$) in the histogram is treated as true plus background events, while the other two hatched regions ($-13.0 \leq y \leq -7.0$ and $7.0 \leq y \leq 12.0$) are treated as background events. A wider middle region ($-8.0 \leq y \leq 8.0$) is used to deduce differential cross sections in order to reduce the loss of the true events. A deduced background spectrum is plotted in Fig. 3.11 versus excitation energy as well as the true plus background spectrum. The peak of the background events observed at 5 MeV is due to the tail of the protons coming from multiple scattering at the target. A bump of the background events around E_x=19 MeV is due to the protons scattered at the fringe of the entrance to the spectrometer from the scattering chamber.

Polarization of the scattered protons ($p^{\rm fpp}_{x,{\rm t}}$) for an excitation energy bin has been obtained by subtracting the background by using the following equations:

$$
\begin{aligned}
p^{\rm fpp}_{x,{\rm t}} &= \frac{1}{r} p^{\rm fpp}_{x,{\rm tb}} - \frac{1-r}{r} p^{\rm fpp}_{x,{\rm b}} \ , \\
r &\equiv 1 - \frac{N_{\rm b}}{N_{\rm tb}} \ ,
\end{aligned}
$$

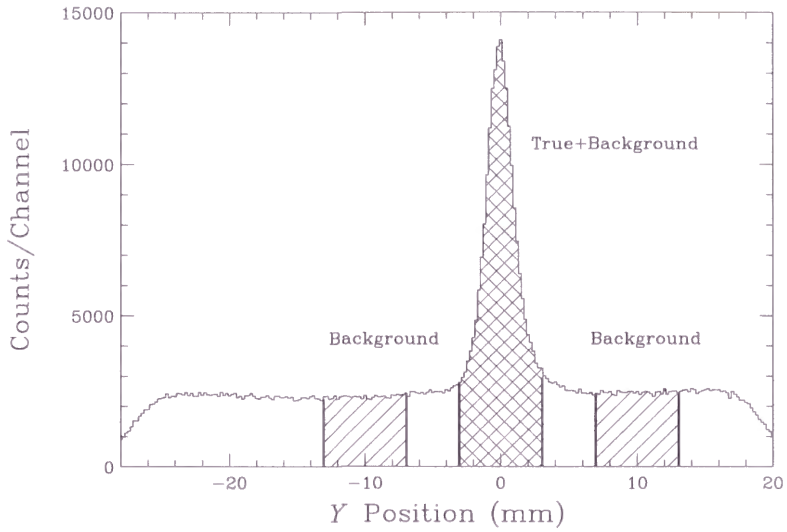

Figure 3.10: Histogram of the vertical (y) position at the focal plane for the excitation of the 1^+, T=0 state at 12.7 MeV. The middle hatched region is treated as true and background events, and the other two hatched regions are treated as background events.

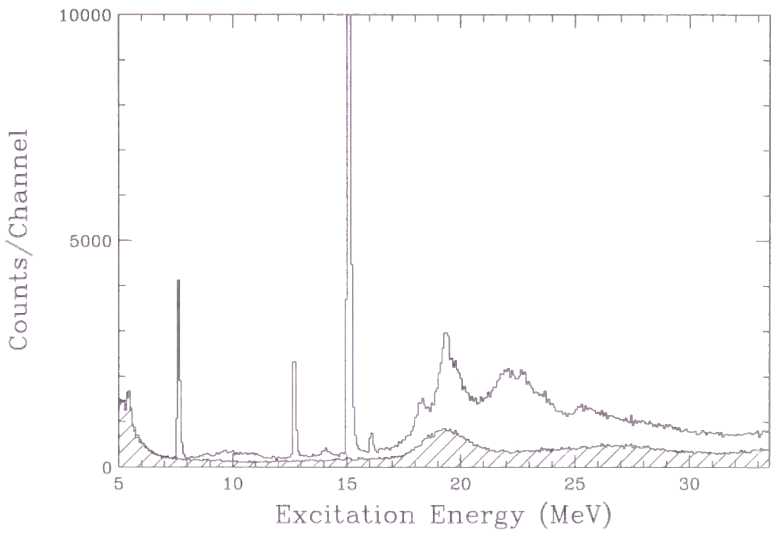

Figure 3.11: Excitation energy spectrum for the ^{12}C(p,p') reaction at 0°. The hatched region is the background events estimated by setting background gates in the y position spectrum (see Fig. 3.10).

$$\Delta p_{x,\mathrm{t}}^{\mathrm{fpp}} = \sqrt{(\frac{\Delta p_{x,\mathrm{tb}}^{\mathrm{fpp}}}{r})^2 + (\frac{\Delta r}{r^2} p_{x,\mathrm{tb}}^{\mathrm{fpp}})^2 + (\frac{1-r}{r}\Delta p_{x,\mathrm{b}}^{\mathrm{fpp}})^2 + (\frac{\Delta r}{r^2} p_{x,\mathrm{b}}^{\mathrm{fpp}})^2} \ ,$$
$$\Delta r = \frac{N_{\mathrm{b}}}{N_{\mathrm{tb}}}\sqrt{\frac{1}{N_{\mathrm{b}}} + \frac{1}{N_{tb}}} \ . \tag{3.34}$$

N_{b} (N_{tb}) denotes the number of the background (true plus background) events in the energy bin, and r is defined as the ratio of the true events to the true plus background events. $p_{x,\mathrm{b}}^{\mathrm{fpp}}$ and $p_{x,\mathrm{tb}}^{\mathrm{fpp}}$ denote the x component of the polarization at the focal plane for the background events and the true plus background events, respectively. $p_{x,\mathrm{tb}}^{\mathrm{fpp}}$ is the polarization obtained by applying for the true plus background gate on the y spectrum (Fig. 3.10). The average of polarizations obtained for the two background gates on the y spectrum was used as $p_{x,\mathrm{b}}^{\mathrm{fpp}}$. The width of the energy bin was set as 200 keV.

3.12 Polarization transfer coefficients

The PT observables are related to the beam polarization and the polarization at the focal plane by the relation

$$p_{x,\mathrm{t}}^{\mathrm{fpp}} = D_{SS} p_x^{\mathrm{beam}} \cos\delta_b' + D_{LL} p_z^{\mathrm{beam}} \sin\delta_b' \ , \tag{3.35}$$

where p_x^{beam} and p_z^{beam} denote the x and z components of the beam polarization, respectively (see Eq. 3.3). δ_b' ($\sim 407^\circ$ for E_x=15.1 MeV) is the spin precession angle in the spectrometer. The value of δ_b' (161.7° for the primary beam) depends on the proton momentum (see Sec. B.1). The dependence of δ_b on the excitation energy (E_x) has been fitted by a linear equation as

$$\delta_b(\mathrm{deg}) = 161.7 + 0.119 E_x(\mathrm{MeV}) \ , \tag{3.36}$$

by using the central incidence angles measured at the focal plane for several excitation energies.

Then D_{SS} and D_{LL} can be simply decomposed by using the data taken with two different orientations of the beam polarization in the horizontal plane. But in actual, since the orientation of the beam polarization changed several times due to the re-tunings

of the cyclotron, the number of the orientations is larger than two. The least square fit has been applied to deduce the PT observables from all the obtained data. Eq. 3.35 is converted to the form

$$a_i D_{SS} + b_i D_{LL} + c_i = 0 \ . \tag{3.37}$$

The suffix i is for distinguishing different measurements (called 'run'). The values a_i, b_i, and c_i and their statistical errors (Δa_i, Δb_i, and Δc_i) are calculated from the experimental data for each run:

$$\begin{aligned} a_i &= p_x^{\rm beam} \cos\delta_s' \ , \\ b_i &= p_z^{\rm beam} \sin\delta_s' \ , \\ c_i &= -p_{x,{\rm t}}^{\rm fpp} \ , \\ \Delta a_i &= \Delta p_x^{\rm beam} |\cos\delta_s'| \ , \\ \Delta b_i &= \Delta p_z^{\rm beam} |\sin\delta_s'| \ , \\ \Delta c_i &= \Delta p_{x,{\rm t}}^{\rm fpp} \ . \end{aligned} \tag{3.38}$$

The values of D_{SS} and D_{LL} have been determined by minimizing the χ^2 of the equations for 53 runs. The statistical errors of D_{SS} and D_{LL} have been obtained from the differential coefficients by the following equations:

$$\begin{aligned} (\Delta D_{SS})^2 &= \sum_i \left\{ (\frac{\partial D_{SS}}{\partial a_i}\Delta a_i)^2 + (\frac{\partial D_{SS}}{\partial b_i}\Delta b_i)^2 + (\frac{\partial D_{SS}}{\partial c_i}\Delta c_i)^2 \right\} \ , \\ (\Delta D_{LL})^2 &= \sum_i \left\{ (\frac{\partial D_{LL}}{\partial a_i}\Delta a_i)^2 + (\frac{\partial D_{LL}}{\partial b_i}\Delta b_i)^2 + (\frac{\partial D_{LL}}{\partial c_i}\Delta c_i)^2 \right\} \ . \end{aligned} \tag{3.39}$$

Chapter 4

RESULTS

4.1 Excitation energy spectrum

An excitation energy spectrum of the $^{12}C(p,p')$ reaction at 0° is plotted in Fig. 4.1. The scattered protons were measured in a broad excitation energy region of 5–33.5 MeV. The lowest excitation energy, 5 MeV, was achieved owing to the holes opened in the frames of the wire chambers to pass the primary beam through. The energy resolution in Fig. 4.1 is 120 keV in FWHM. In the figure, background events have been subtracted by the method described in Sec. 3.11. Background events seem to be properly subtracted at least in the region of the discrete states. The signal to noise (S/N) ratio is 20/1 at the peak of the 12.7 MeV state. The 0^+ state at 7.65 MeV, the 1^+, T=0 state at 12.7 MeV, and the 1^+, T=1 state at 15.1 MeV are clearly observed. In general, the differential cross sections of $\Delta L = 0$ transitions have the maximum at 0°, while that of the transitions with $\Delta L > 0$ quickly decrease as the scattering angle approaches to 0°. Therefore $\Delta L = 0$ transitions are relatively enhanced at 0° compared with other transitions.

An enlarged spectrum of Fig. 4.1 is plotted in Fig. 4.2. Broad resonances at 18.4 MeV, 19.5 MeV, and 22.5 MeV are also observed. A broad state at 10.3 MeV, which was tentatively assigned as 0^+ in Ref. 63, is observed. Several authors [60, 61, 62] treated a 2^+ state around 10 MeV in α-cluster models as a member of the rotational band starting from the 0^+ state at 7.65 MeV. Unfortunately it is not possible to assign the spin-parity

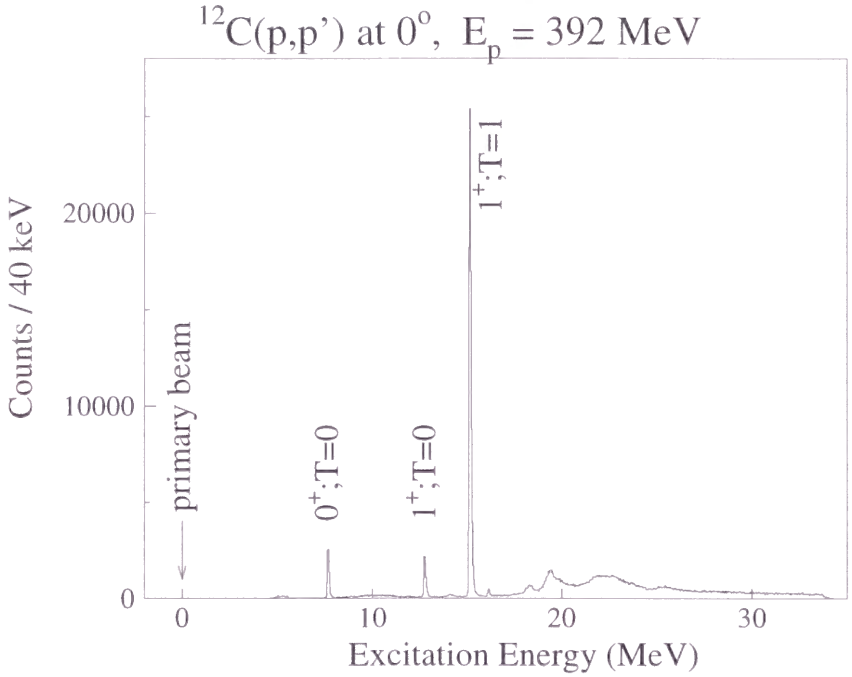

Figure 4.1: Excitation energy spectrum in the $^{12}C(p,p')$ reaction at 0° and at E_p=392 MeV. The energy resolution is 120 keV in FWHM.

of the broad state only with this data because the vertical acceptance of the spectrometer was very large and it is not feasible to see the angular distribution of the state at the very forward angles.

Another broad state is observed at 14.1 MeV. At 14.08 MeV, a 4^+ state has been reported [63]. It is not clear whether the observed states can be assigned as this 4^+ state or not. It is because a large L transfer of 4 is required in the excitation of a 4^+ state, and the excitation must be suppressed at 0°.

4.2 Differential cross sections

Differential cross sections for the discrete states have been deduced from the following equation

$$\frac{d\sigma}{d\Omega} = CN\frac{eA}{QTN_A\Omega t\eta L}$$

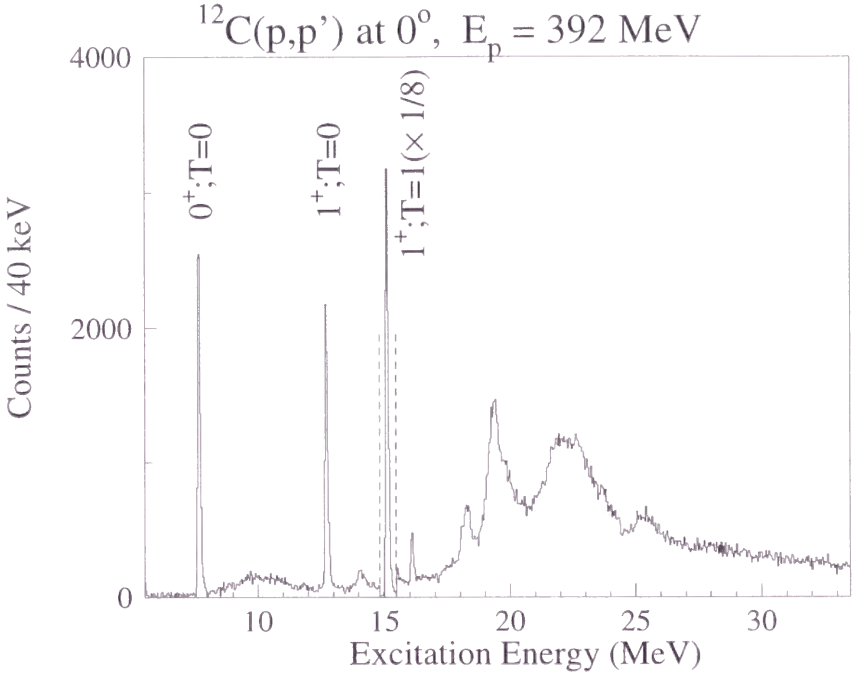

Figure 4.2: Enlarged spectrum of Fig. 4.1.

$$\sim \frac{1}{3.76} N \frac{A}{QT\Omega} \frac{1}{t\eta L} . \tag{4.1}$$

The notation of the variables is shown in Table 4.1. The statistical uncertainty is in the form

$$\Delta \frac{d\sigma}{d\Omega} = \frac{1}{\sqrt{N}} \frac{d\sigma}{d\Omega} . \tag{4.2}$$

The results of the measured differential cross sections are summarized in Table 4.3 and are plotted in Fig. 4.3. The solid curves represent the DWIA calculation using the Franey and Love interaction. The DWIA calculation slightly underestimates the experimental data. See Chap. 5 for details.

4.3 Polarization transfer observables

Experimental results for the PT observable are listed in Table 4.4 for discrete states. The D_{SS} and D_{LL} values for the excitation of the 0^+ state are in good agreement with the

Table 4.1: Notation of the variables used in the expression of the differential cross sections in Eq. 4.1 and their values used in the calculation.

$\frac{d\sigma}{d\Omega}$	differential cross section		[mb sr^{-1}]
N	number of detected particles		[counts]
Q	total beam charge		[nC]
T	target thickness	30.	[mg cm^{-2}]
N_A	Avogadro constant	6.02×10^{23}	[counts mol^{-1}]
Ω	solid angle (c.m.)	4.53	[msr]
e	elementary charge	1.60×10^{-19}	[C]
A	target atomic weight	12.0	[g mol^{-1}]
t	target abundance in weight	0.9881	[-]
η	detector efficiency		[-]
L	DAQ live time		[-]
C	unit conversion constant	10^{42}	[mg g^{-1} msr sr^{-1} mb cm^{-2} nC C^{-1}]

Table 4.2: Natural abundance of the carbon isotopes. The data were taken from Ref. 64. A value of 931.494 MeV is used as the unified atomic mass. The abundance of the ^{14}C atoms is omitted.

isotope	mass excess	mass	abundance	
	(MeV)	(MeV)	atomic percent	weight percent
^{12}C	0.000	11178.	98.90	98.81
^{13}C	3.125	12113.	1.10	1.19

PWIA predictions of 1.0 The measured PT observables for the excitation of the 1^+, T=0 state at 12.7 MeV are plotted in Fig 4.4 by solid circles. The measured PT observables for the excitation of the 1^+, T=1 state at 15.1 MeV are plotted in Fig 4.5 by solid circles.

The double differential cross sections and the PT observables D_{SS} and D_{LL} are plotted as functions of the excitation energy of the ^{12}C nucleus in Fig. 4.6.

Table 4.3: Measured differential cross sections for discrete states with statistical uncertainty and systematic uncertainty.

E_X	J^π	T	θ	$\frac{d\sigma}{d\Omega}$±stat.±syst.
7.65	0^+	0	0.0	0.42±0.01±0.02
12.7	1^+	0	0.0	0.33±0.01±0.02
15.1	1^+	1	0.0	3.16±0.02±0.16

Table 4.4: Measured PT observables with statistical errors.

E_X	J^π	T	D_{SS}^{exp}	D_{LL}^{exp}	Σ
7.65	0^+	0	1.00 ± 0.06	1.07 ± 0.07	-0.02 ± 0.04
12.7	1^+	0	-0.63 ± 0.07	0.74 ± 0.08	0.88 ± 0.04
15.1	1^+	1	-0.18 ± 0.02	-0.58 ± 0.02	0.99 ± 0.01

Table 4.5: Systematic uncertainties for the measured differential cross sections.

horizontal acceptance (θ_s)	2	%
vertical acceptance (ϕ_s)	3	%
beam current	3	%
target thickness	1	%
peak fit	2	%
total	5	%

4.4 Systematic uncertainties

Systematic uncertainties are tabulated for the measurement of differential cross sections (Table 4.5) and PT observables (Table 4.6). The systematic uncertainties in the horizontal and vertical acceptances have been determined to be 2% and 3.4%, respectively (see Sec. 3.6). The transmission of beam current from the target position to the 0° Faraday cup was determined by by comparing the beam currents measured by the 0° Faraday cup and by the internal Faraday cup in the scattering chamber (Sec. 2.7). The transmission was more than 99%. The uncertainty of the beam current arising from the current integrator circuit was less than 3% in the calibration using standard resistances.

Table 4.6: Systematic uncertainties ($\Delta D_{ii}/D_{ii}$) of the measured PT observables.

analyzing power of the BLP	5	%
effective analyzing power of the FPP	3	%
bending angle of the spectrometer	2	%
total	6	%

The fluctuation of the PT observables relative to their magnitude was less than 2% for the uncertainty of the bending angle of the spectrometer ($\pm 0.2^\circ$). The uncertainty of the effective analyzing power of the FPP was estimated by the uncertainty of the input parameter of the p+C inclusive analyzing power, which deviates 3% depending on the data base.

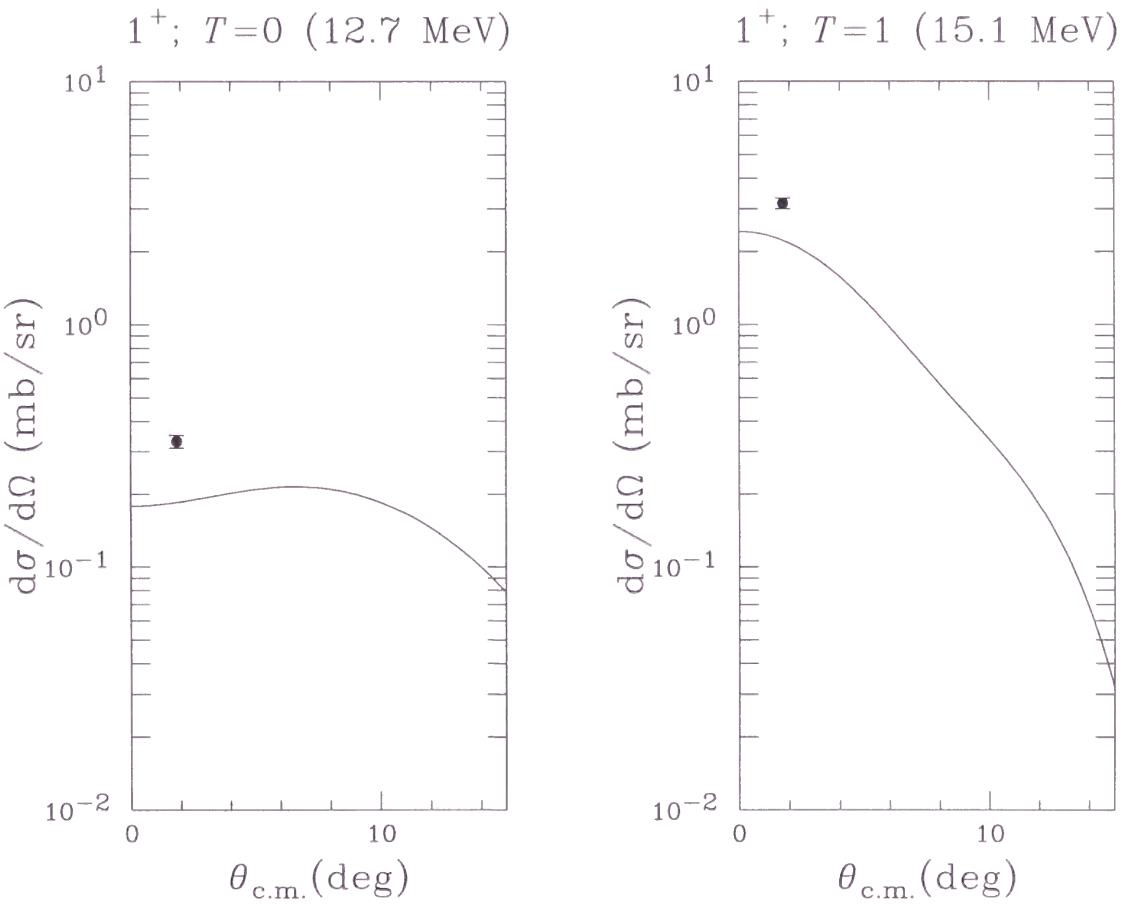

Figure 4.3: Measured differential cross sections with statistical and systematic errors for excitation of the 1^+; T=0 state at 12.7 MeV (left panel) and the 1^+; T=0 state at 15.1 MeV (right panel). The experimental data are plotted at the average scattering angle in the acceptance of the spectrometer. Solid lines are the predictions of the DWIA calculation using the Franey and Love interaction.

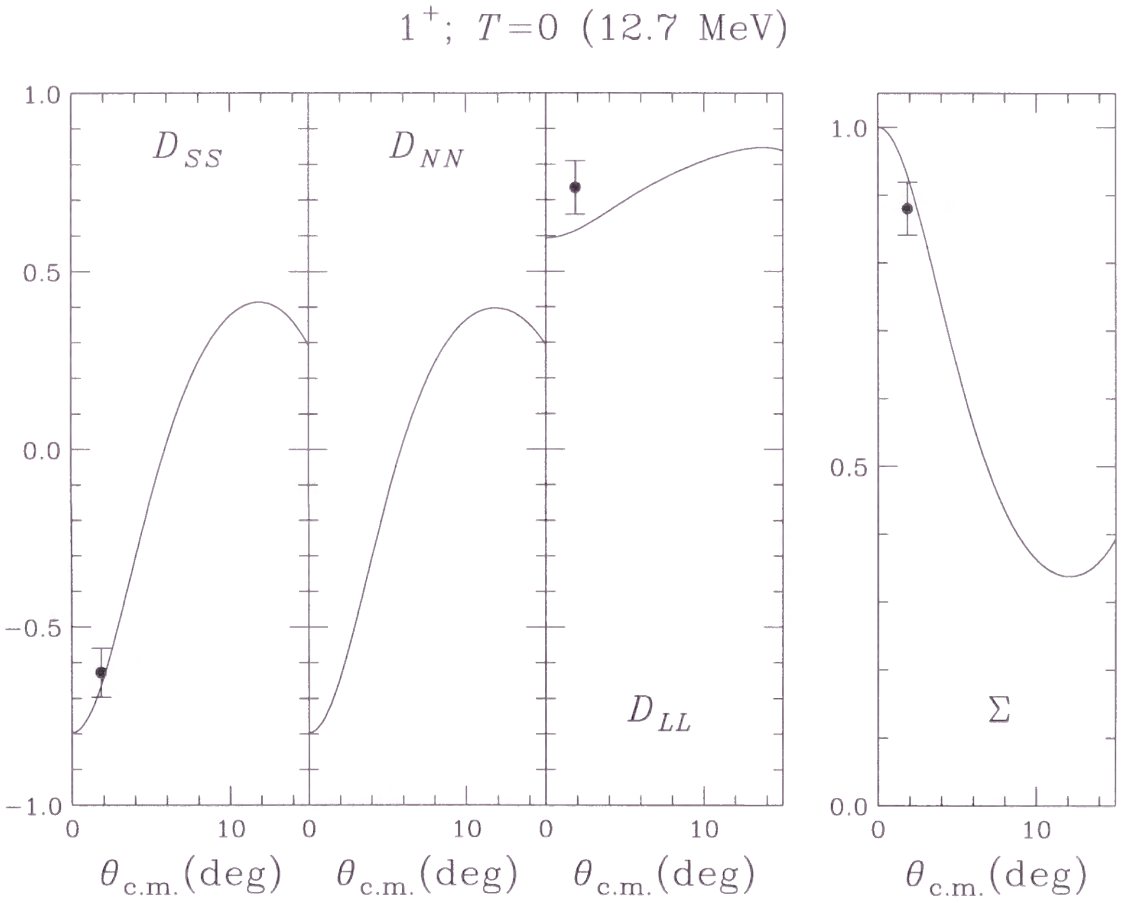

Figure 4.4: Measured PT observables for excitation of the 1^+, T=0 state at 12.7 MeV are plotted by solid circles with statistical uncertainties. The experimental data are plotted at the average scattering angle in the acceptance of the spectrometer. The total spin transfer was calculated by Eq. 1.15. Solid lines shows the prediction of the DWIA calculations using the FL interaction described in Chap. 5.

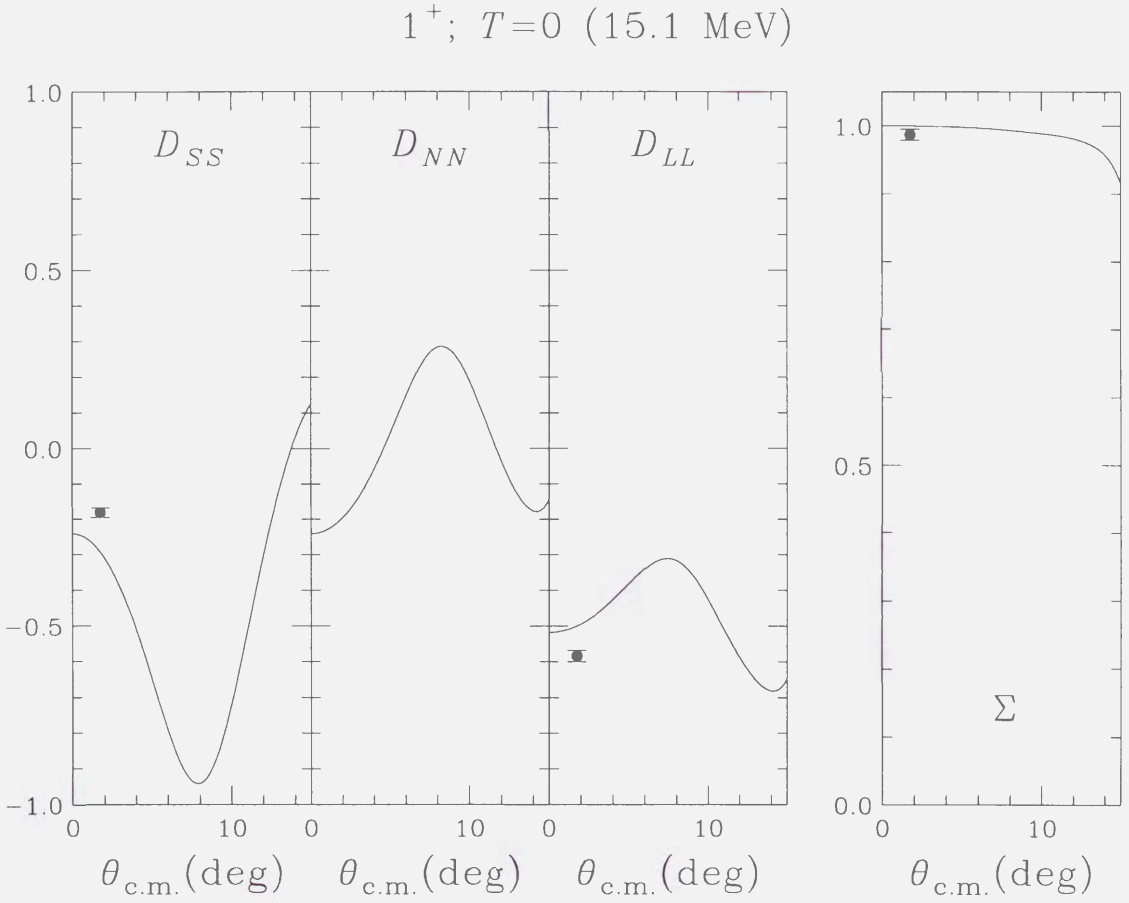

Figure 4.5: Measured PT observables for the excitation of the 1^+, T=1 state at 15.1 MeV are plotted by solid circles with statistical uncertainties. The experimental data are plotted at the average scattering angle in the acceptance of the spectrometer. Solid lines shows the prediction of the DWIA calculations using the FL interaction described in Chap. 5.

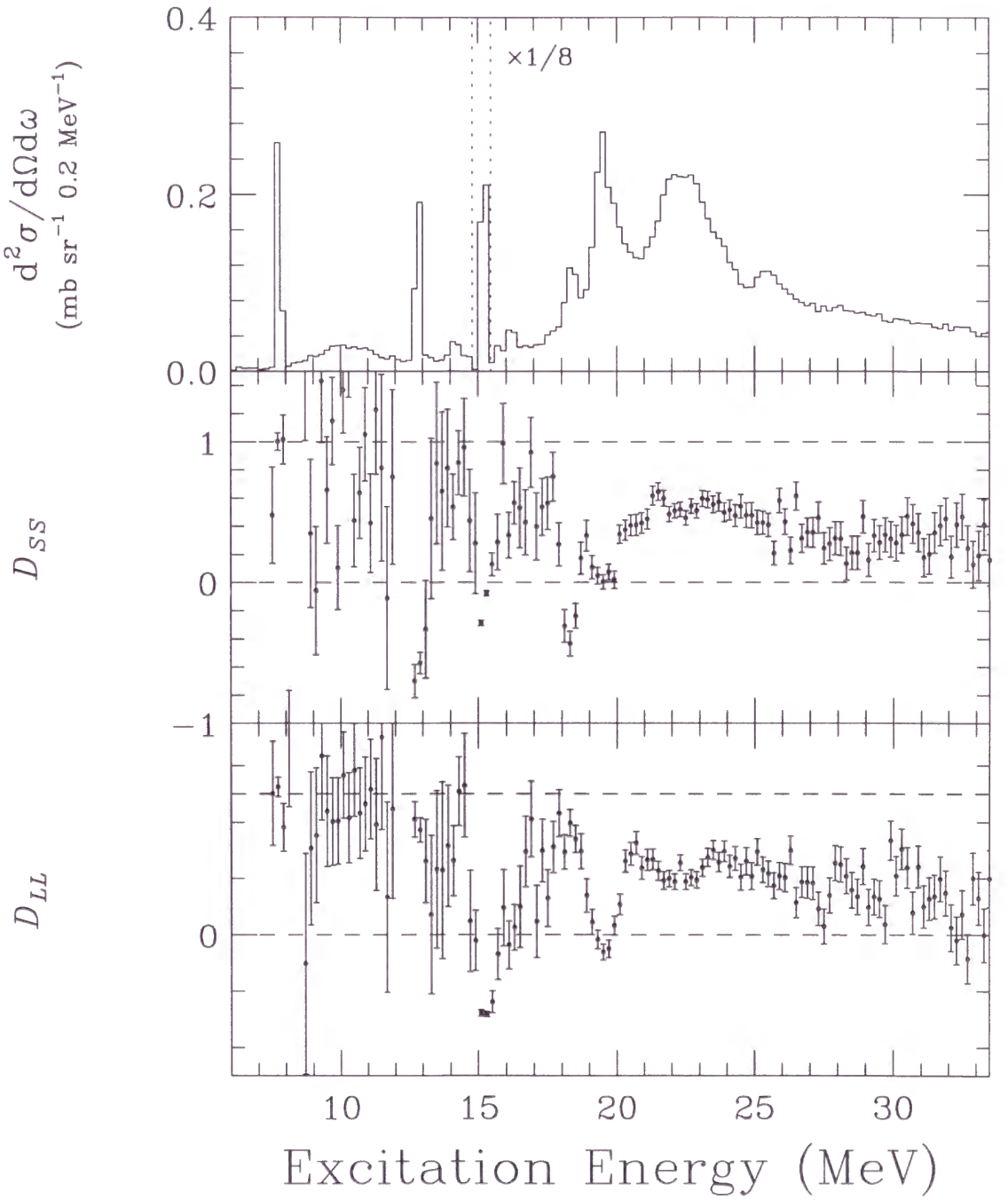

Figure 4.6: Measured double differential cross sections and the PT observables, D_{SS} and D_{LL}, versus excitation energy of ^{12}C.

Chapter 5

DISCUSSION

In this chapter, the experimental results are compared with distorted wave impulse approximation (DWIA) calculations. In Sec. 5.2, the strength of the V_σ interaction is studied from the measured PT observables for the excitation of the 1^+, T=0 state. In Sec. 5.3, the strength of V_τ^T is discussed from the PT observables for excitation of the 1^+, T=1 state. In Sec. 5.4, a better parametrization of the effective NN interaction is investigated. Spin-isospin decomposition of the strengths in the continuum on ^{12}C nucleus is performed in Sec. 5.5.

5.1 DWIA calculations

Microscopic DWIA calculations are performed by using a program code DWBA91 [65]. Cohen and Kurath target wave functions [36] are employed for the excitation of the 1^+ states. A simple one-particle-one-hole configuration is assumed for the 0^+ state. Since the PT observables for the 0^+ excitation at 0° are determined by the axial symmetry and the conservation law of angular momentum, they have essentially no dependence on the detail configuration of the excited state. The optical potential parameters and the length parameters of the harmonic oscillator radial distribution are taken from Ref. 66.

Three types of effective interactions are employed as the NN interaction. One is the 425 MeV parameter set of the effective interaction by Franey and Love (FL) [40].

Table 5.1: The measured PT observables with statistical errors are compared with the DWIA calculations using the Franey and Love (FL), Paris free (PF), and Paris density dependent (PD) effective interactions. The DWIA results are averaged in the acceptance of the spectrometer as described in Appendix C so as to be directory compared with the experimental results.

			DWIA^{cor}		
E_X (J^π; T)	Values	Exp.	FL	PF	PD
7.65 (0^+; 0)	D_{SS}	1.00±0.06	1.00	1.00	1.00
	D_{LL}	1.07±0.07	1.00	1.00	1.00
	Σ	-0.02±0.04	0.00	0.00	0.00
12.7 (1^+; 0)	D_{SS}	-0.63±0.07	-0.64	-0.46	-0.41
	D_{LL}	0.74±0.08	0.62	-0.13	0.10
	Σ	0.88±0.04	0.92	0.95	0.93
15.1 (1^+; 1)	D_{SS}	-0.18±0.02	-0.21	-0.28	-0.25
	D_{LL}	-0.58±0.02	-0.50	-0.35	-0.40
	Σ	0.99±0.01	0.98	0.98	0.98

The others are the Paris free interaction (PF) and the Paris density-dependent (PD) interaction [67] derived from the Paris potential [68]. The averaged PT observables (D_{SS}^{cor} and D_{LL}^{cor}) in the acceptance of the spectrometer are obtained by Eq. C.26 from the calculated PT observables and differential cross sections. The total spin transfers are calculated by Eq. C.27 using the averaged PT observables.

The results of the DWIA calculations are listed in Table 5.1 with the experimental results. The measured PT observables for excitation of the 0^+ state are consistent with the predictions of the DWIA.

5.2 Strength of V_σ

The strength of the V_σ interaction has not been well known in spite of a long term study on the NN interaction, since the interaction is considered to be very weak and the observables in the NN scattering are not sensitive to the strength of V_σ. We will investigate the strength of V_σ by using the unique property that the PT observables for excitation of the 1^+, T=0 state at 0° is sensitive to the strength of V_σ as described in

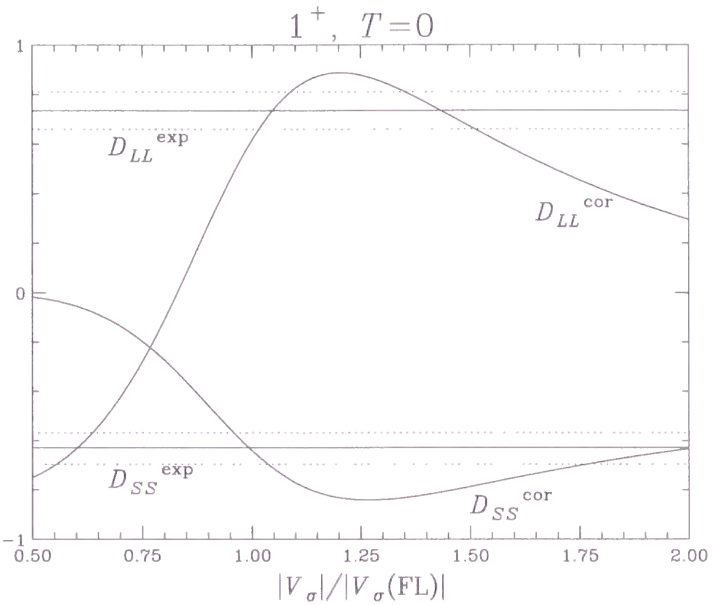

Figure 5.1: PT observables for the 1^+, T=0 excitation calculated with the FL interaction as a function of the magnitude of V_σ which is artificially modified relative to that of the FL interaction. Solid and dashed horizontal lines represent the central values of the experimental results and the 1σ error bars, respectively.

Chap. 1. Fig. 5.1 shows the predictions of the PT observables, for the 1^+, T=0 excitation by using the FL interaction as a function of the magnitude of V_σ. The magnitude of the V_σ strength is artificially modified from that of the FL interaction. The solid horizontal lines show the experimental results, and the dotted lines represent the 1σ statistical errors. In the figure, it is observed that the experimental results are well reproduced if the strength of V_σ relative to that of FL is close to unity. This is the first observation of the V_σ strength. The result means that the FL interaction surprisingly well describes the strength of V_σ even though they noted that the determination of V_σ was poor [28].

Fig. 5.2 plots the PT observables and the total spin transfer by the DWIA calculations for the 1^+, T=0 excitation. The total spin transfer is well reproduced by the calculation with the FL interaction. The consistency means that the strength of the isoscalar spin-orbit interaction (V_0^{LS}) relative to that of V_τ^T is well described in the FL interaction. Concerning the D_{SS} and D_{LL} observables, the calculation using the FL interaction well reproduce the data, while the calculations using the PF and PD interactions fail to

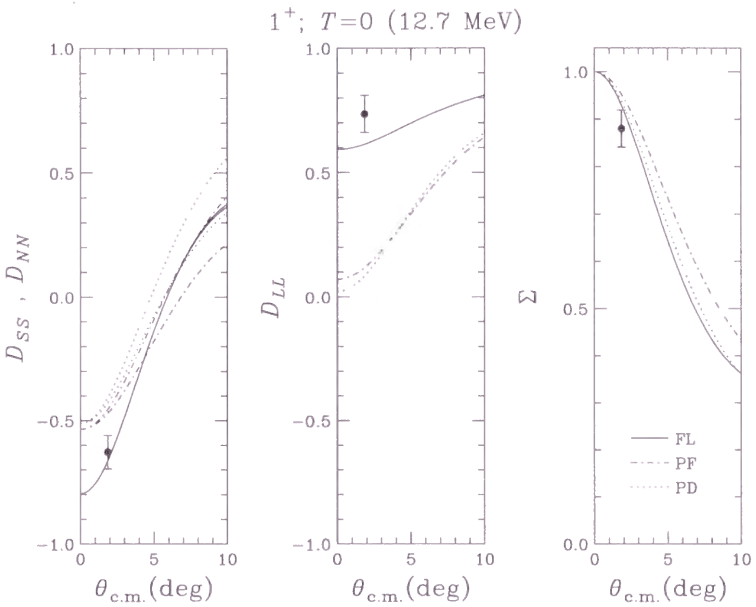

Figure 5.2: Results of the DWIA calculations for the excitation of the 1^+, T=0 state. The curves represent the calculation with the FL interaction (solid), with the PF interaction (dash-dotted), and with the PD interaction (dotted), respectively. In the left panel, the upper (lower) curve represents D_{SS} (D_{NN}) for each PF and PD. The experimental results are plotted by solid circles with statistical errors.

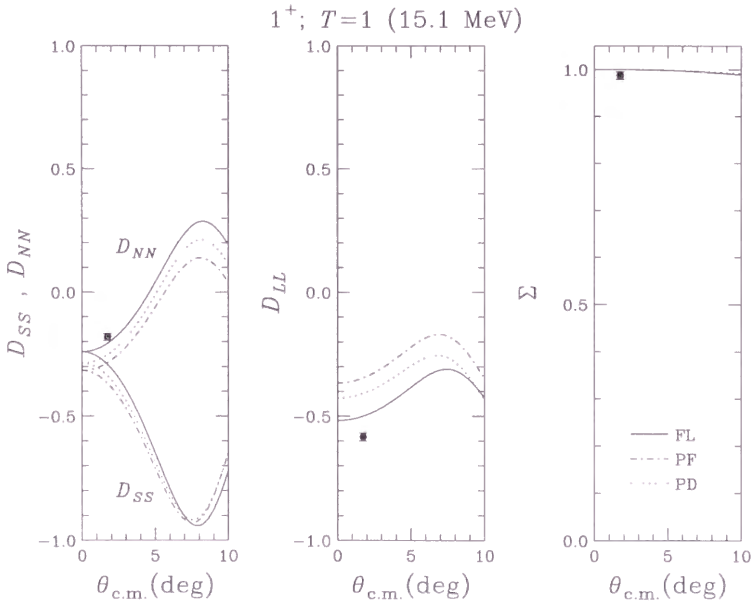

Figure 5.3: Results of the DWIA calculations for the excitation of the 1^+, T=1 state. For details, see the caption of Fig. 5.2.

describe the data especially for D_{LL}. The V_σ term is very weak and is considered to be poorly determined from the NN scattering data [28, 41]. The result shows that the strength of V_σ is reasonably described in the FL interaction while it is not well described in the PF and PD interactions.

5.3 Strength of V_τ^T

The results of the DWIA calculations for excitation of the 1^+, T=1 state are plotted in Fig. 5.3. The total spin transfer is well reproduced by the DWIA calculations. The DWIA calculation with the FL interaction better describes the measured D_{SS} and D_{LL} than those with the PF and PD interactions. It should be noted that the experimentally measured $D_{SS}^{\rm exp}$ is an average of the theoretical predictions of D_{SS} and D_{NN}; $D_{SS}^{\rm exp}$ is expressed by a linear combination of D_{SS} and D_{NN} as described by Eq. C.26. The averaged value is closer to the D_{NN} value than the D_{SS} value due to the geometry of the acceptance.

The PT observables for the 1^+, T=1 excitation are sensitive to the relative strength of the tensor interactions to that of $V_{\sigma\tau}$ [16, 17]. From the figure, it is inferred that the strength of the tensor interactions relative to that of $V_{\sigma\tau}$ is better described in the FL interaction than in the PF and PD interactions. The experimental D_{SS} value (-0.18±0.02) is close to the D_{NN} values at 0° measured by the ^{12}C$(\vec{p},\vec{n})^{12}$N(g.s.) reaction at E_p=160 MeV (-0.24±0.03) [16] and at E_p=295 MeV (-0.22±0.02) [17]. The ground state of the ^{12}N nucleus is considered as the isobaric analog state of the 1^+, T=1 state at 15.1 MeV on ^{12}C. The PT observables for the $(\vec{p},\vec{p})$ and $(\vec{p},\vec{n})$ reactions are comparable due to the isobaric symmetry of the nuclear reaction.

5.4 Modification of the effective interactions

In this section, parametrizations of the effective interaction are discussed. At first, the predictions of the calculations using the effective interaction modified by Sakemi *et al.* are

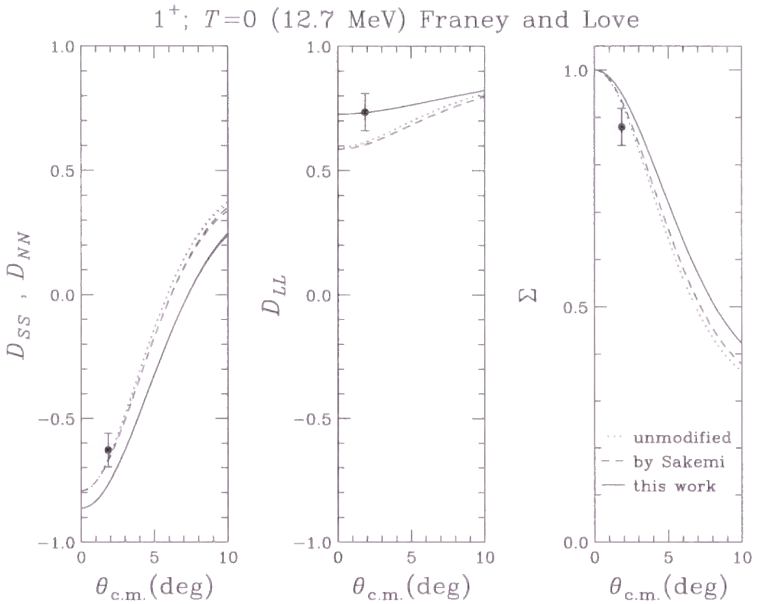

Figure 5.4: PT observables by DWIA calculations with the FL interactions for excitation of the 1^+, T=0 state. The curves are calculated with the interactions which are unmodified (dotted), modified by Sakemi *et al.* (dashed), and modified in the present work (solid). In the left panel, D_{SS} and D_{NN} are indistinguishable.

compared with the experimental results. Next, a better parametrization is investigated by modifying the FL and PF interactions to fit the experimental results.

5.4.1 Modification of V_τ^T by Sakemi *et al.*

Sakemi *et al.* [21] measured relative cross sections for the two 1^+ states in the ^{12}C(p,p') reaction at 0°. They claimed a requirement of the reduction of V_τ^T at 200 and 300 MeV for the FL interaction, and at 200, 300, and 400 MeV for the PF interaction [21] to reproduce the data. A little enhancement of V_τ^T is required for the FL interaction at 400 MeV. According to Ref. 21 the shortest-range part of Re VT_τ in the FL and PF interactions has been modified (see Tab. 5.2). The PT observables calculated by using the modified interaction are plotted in Figs. 5.4–5.7.

In the modification, the strength of V_τ^T in the FL interaction is a little enhanced as shown in Fig. 5.8. The modified FL interaction describes the PT observables of this work

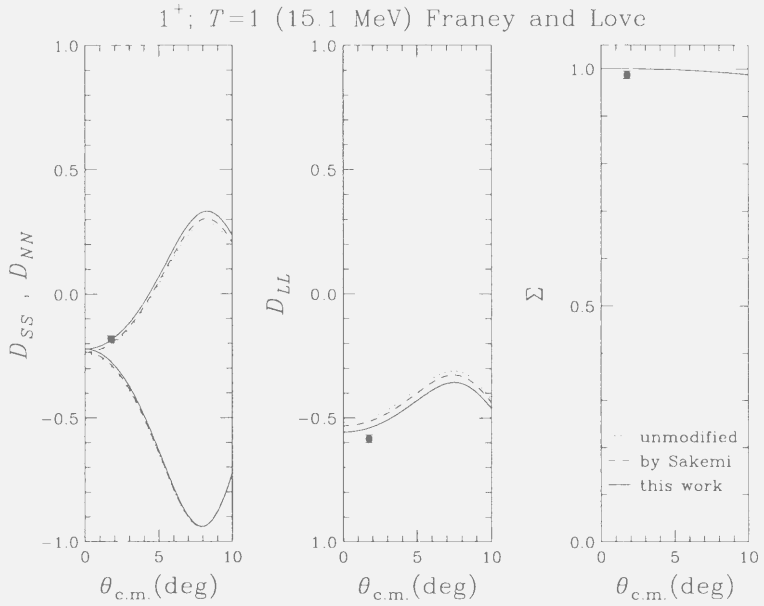

Figure 5.5: For excitation of the 1^+, T=1 state as Fig. 5.4.

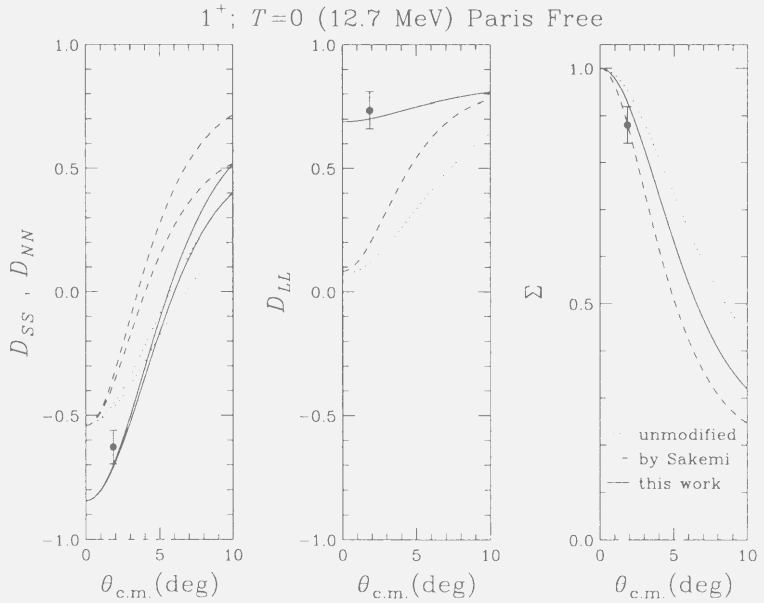

Figure 5.6: PT observables by DWIA calculations with unmodified and modified PF interactions for excitation of the 1^+, T=0 state. The curves are calculated with unmodified PF interaction (dotted), modified by Sakemi *et al.* (dashed), modified by the present work (solid). In the left panel, the upper (lower) curve represents D_{SS} (D_{NN}).

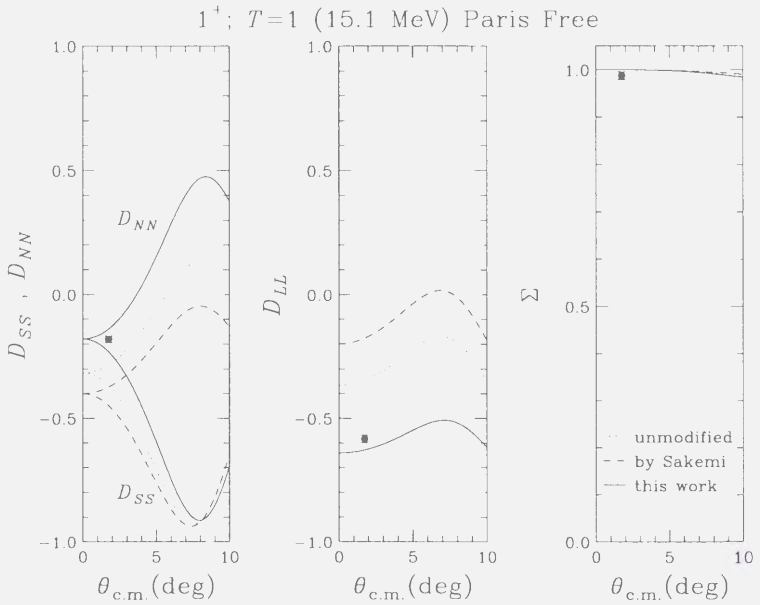

Figure 5.7: For excitation of the 1^+, T=1 state as Fig. 5.6.

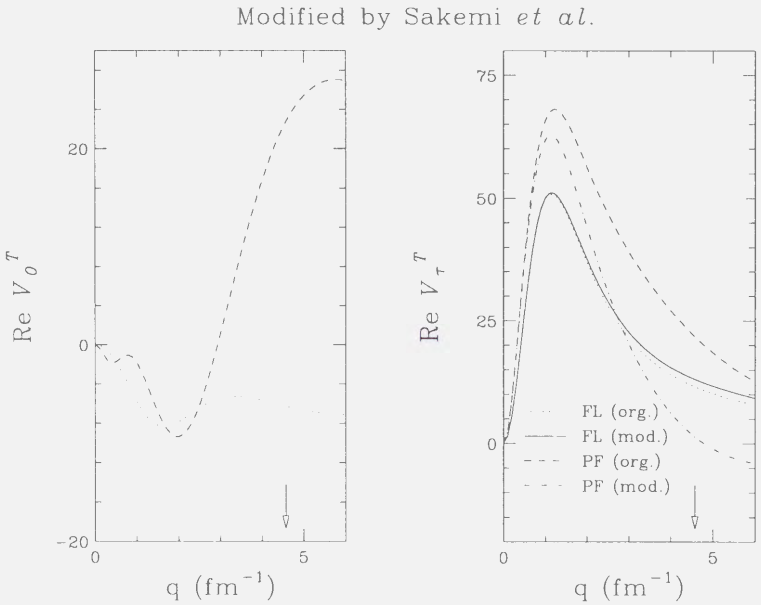

Figure 5.8: Real part of the tensor interactions, V_0^T and V_τ^T as functions of the momentum transfer. The curves are calculated with unmodified FL interaction (dotted), modified FL interaction by Sakemi *et al.* (solid), unmodified PF interaction (dashed), and modified PF interaction by Sakemi *et al.* (dot-dashed). The arrows represent the momentum transfer relevant to the knock-on exchange amplitude. Note that V_0^T was unmodified while V_τ^T was modified in Ref. 21.

Table 5.2: Modification of the strength of the shortest-range part of the tensor interactions for 400 MeV in Ref. 21.

Int.	Term	Range (fm)	Original	Modified
FL	V^{TNE}	0.150	-3.01782E+4	-3.46E+4
FL	V^{TNO}	0.150	-6.93196E+3	-5.44E+3
PF	V^{TNE}	0.175	3.96491E+3	8.41E+3
PF	V^{TNO}	0.175	4.56919E+3	3.09E+3

slightly better than the unmodified interaction (see Figs. 5.4 and 5.5).

The strength of V_τ^T in the PF interaction is highly (Fig. 5.8). In the case of the PF interaction, the modification results in worse predictions of the PT observables, especially for the 1^+, T=1 state (see Figs. 5.6 and 5.7). The strength of V_τ^T in the unmodified PF interaction is stronger than that of the original FL interaction. But the reduction of the V_τ^T in the PF interaction resulted in in worse predictions of the PT observables. The reason of this behavior comes from the large difference in the isoscalar tensor interaction, V_0^T, which can be seen in Fig. 5.8 at the momentum transfer relevant to the knock-on exchange amplitude.

5.4.2 The 1^+, T=1 state and the tensor interactions

In order to obtain a better parametrization of the effective interaction, the shortest-range parts of both the real V_0^T and V_τ^T interactions have been modified for each the FL and PF interaction. The relative cross sections $\frac{d\sigma}{d\Omega}(1^+,T{=}0)/\frac{d\sigma}{d\Omega}(1^+,T{=}1)$ and the PT observables $D_{SS}(1^+,T{=}1)$ and $D_{NN}(1^+,T{=}1)$ are fitted, since these observables are sensitive to the strength of the tensor interactions. In the fitting process, the calculated observables are averaged in the acceptance of the spectrometer according to the procedure described in Appendix C. The experimental uncertainties are set to be 3% for $\frac{d\sigma}{d\Omega}(1^+,T{=}0)/\frac{d\sigma}{d\Omega}(1^+,T{=}1)$, and 0.03 for $D_{SS}(1^+,T{=}1)$, and $D_{NN}(1^+,T{=}1)$ considering the systematic uncertainties.

The χ^2 map versus the relative strengths of V_0^T and V_τ^T to the original values are

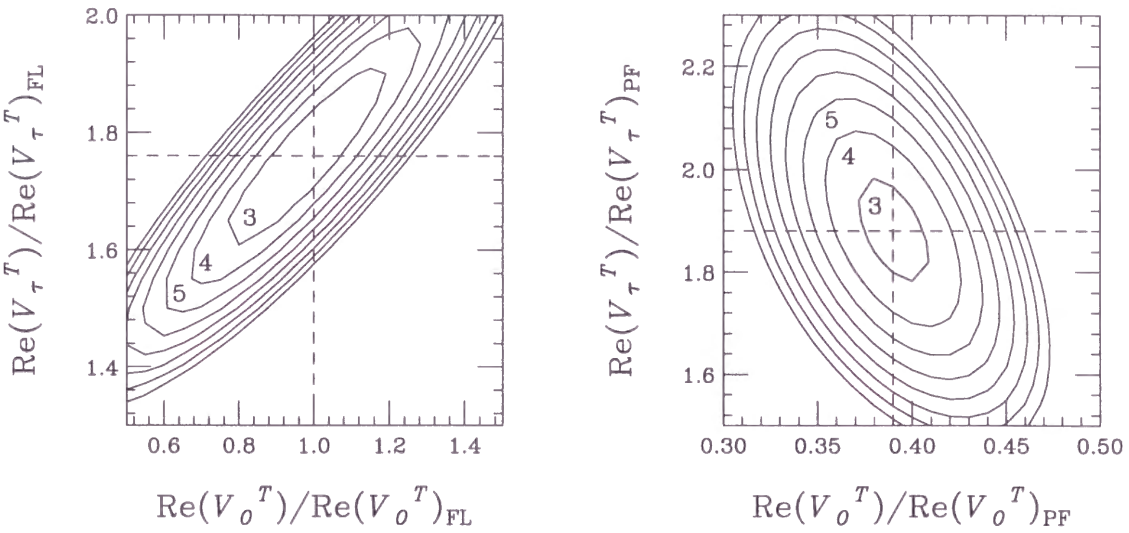

Figure 5.9: Results of the χ^2 fit of the shortest-range part of V_0^T and V_τ^T of the FL interaction (left) and the PF interaction (right). The values denoted by dashed lines, (1.00, 1.76) for FL and (0.39, 1.88) for PF, are used in Tab.5.3 and Fig. 5.10.

Table 5.3: Modified strength of the shortest-range part of the tensor interactions by fitting to the experimental data of this work.

Int.	Term	Range (fm)	Original	Modified
FL	V^{TNE}	0.150	-3.01782E+4	-4.34E+4
FL	V^{TNO}	0.150	-6.93196E+3	-2.52E+3
PF	V^{TNE}	0.175	3.96491E+3	8.71E+2
PF	V^{TNO}	0.175	4.56919E+3	2.01E+3

plotted in Fig. 5.9. The results are summarized in Tab. 5.3 and plotted in Fig. 5.10. Although a large difference is remaining in the strength of the V_0^T term due to the large attractive value of the next shortest-range part of the PF interaction, the strengths of V_0^T and V_τ^T have come close to each other around the momentum transfer relevant to the knock-on exchange amplitude.

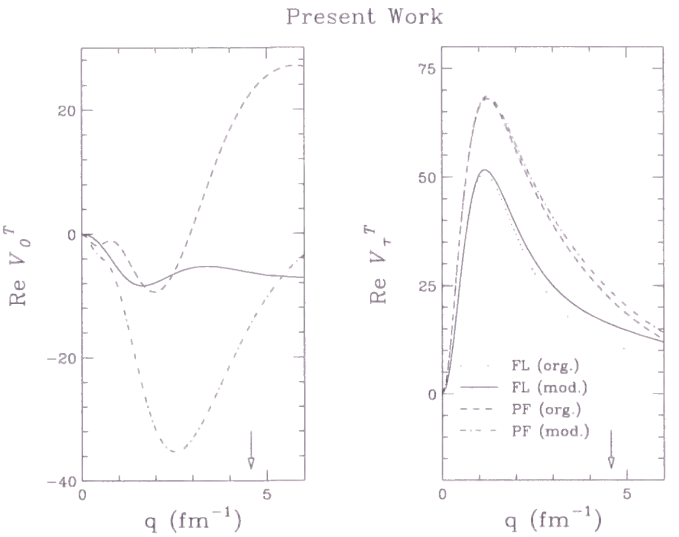

Figure 5.10: Modified V_0^T and V_τ^T strengths versus the momentum transfer compared with the original strengths. The curves are calculated with unmodified FL interaction (dotted), modified FL interaction of the present work (solid), unmodified PF interaction (dashed), and modified PF interaction of the present work (dot-dashed). The arrows represent the momentum transfer relevant to the knock-on exchange amplitude.

5.4.3 The 1^+, T=0 state and the V_σ interaction

The strength of V_σ is sensitive to the PT observables for excitation of the 1^+, T=0 state (see Sec.1.4), but very insensitive to other observables. By using this property, the longest-range part of the the real V_σ interaction has been fitted after the modification described in the previous section. Note that the longest-range of V_σ in the FL interaction is 0.55 fm^{-1}, since the strength of the 1.40 fm^{-1} range part is zero. The statistical uncertainties are used in the calculation of the variance because the experimental uncertainties of these observables are dominated by the statistical ones. The results of the χ^2 distribution is plotted in Fig. 5.11 and the interaction strengths are tabulated in Tab. 5.4.

As shown in Fig. 5.12, the strength of the real V_σ interaction in the FL interaction is slightly enhanced at the lowest momentum transfer region related to the enhancement of the tensor interactions in the previous section. In the case of the PF interaction, the V_σ strength is largely enhanced to reproduce the data. The discrepancy between the FL

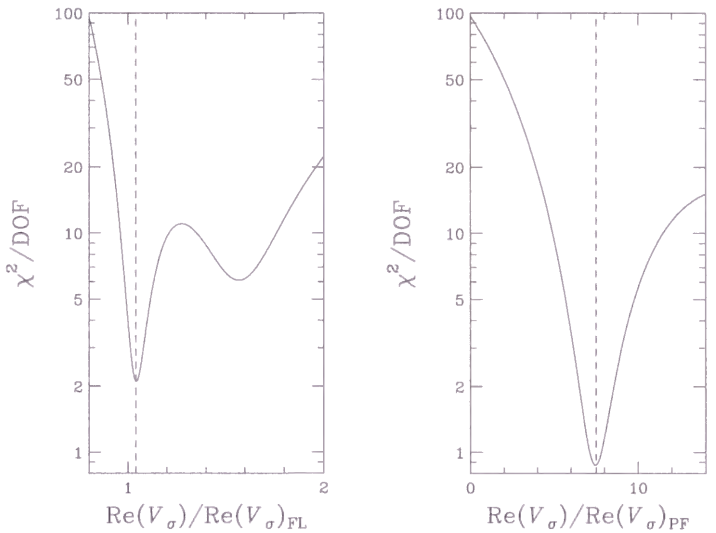

Figure 5.11: Variance (χ^2) per degree of freedom (DOF) versus the strength of the longest-range part of V_σ for the FL interaction (left) and the PF interaction (Right). Strength of V_σ relative to the unmodified one is taken as the horizontal axes. The dashed lines represent the value (1.04 for FL and 7.5 for PF) used in Table 5.4 and Fig. 5.12.

and PF interactions in the V_σ strength at the small momentum transfer region is reduced after the modification of the interactions.

5.5 Spin-isospin structure of the excitation strengths

5.5.1 Decomposition of the spin-flip strengths

The measured total spin transfer (Σ) is plotted in Fig. 5.13 (upper) as a function of the excitation energy. Σ times double differential cross section ($\Sigma \times \frac{d^2\sigma}{d\Omega d\omega}$) is plotted in Fig. 5.13 (lower) by hatched regions compared with the double differential cross section ($\frac{d^2\sigma}{d\Omega d\omega}$). The $\Sigma \times \frac{d^2\sigma}{d\Omega d\omega}$ value is considered to represent spin-flip strengths.

It is inferred from Fig. 5.13 that broad resonances at 18.4 MeV and 19.5 MeV have predominantly spin-flip nature, while a broad resonance at 22.5 MeV has both the spin-flip strength and the non-spin-flip strength. At higher excitation energies, the ratio of the spin-flip strengths to the non-spin-flip strengths gradually increases.

Table 5.4: Results of the modified interaction, in which the real V_σ interaction was fitted to reproduce the PT observables for excitation of the 1^+, T=0 state.

Int.	Term	Range (fm)	Original	Modified
FL	V^{SE}	0.550	-2.02124E+02	-2.13E+02
FL	V^{TE}	0.550	1.21137E+01	1.56E+01
FL	V^{SO}	0.550	-9.72663E+02	-9.83E+02
FL	V^{TO}	0.550	-5.96291E+01	-5.61E+01
PF	V^{SE}	1.449	-1.65076E+01	-1.91E+01
PF	V^{TE}	1.449	-1.37986E+01	-1.29E+01
PF	V^{SO}	1.449	3.93610E+01	3.68E+01
PF	V^{TO}	1.449	1.91574E+00	2.77E+00

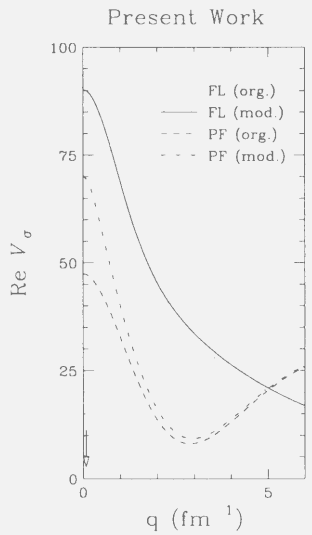

Figure 5.12: Modified V_σ strengths versus the momentum transfer compared with the unmodified strengths. The notations are same as Fig. 5.10. The arrow represents the momentum transfer relevant to the direct interaction.

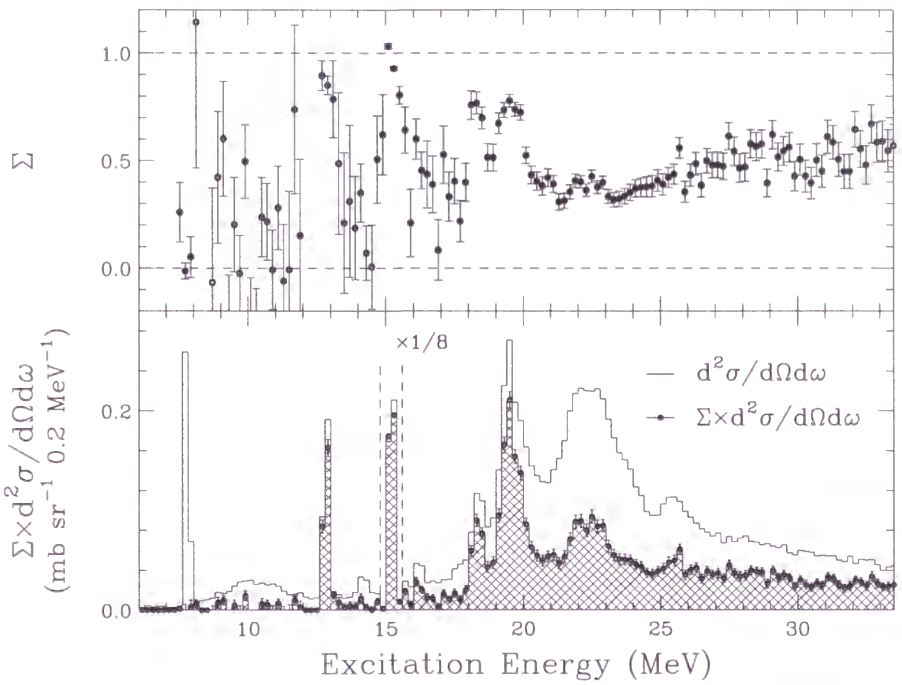

Figure 5.13: Measured total spin transfer versus the excitation energy of ^{12}C.

5.5.2 Isospin structure of the spin-flip excitations

Substitution of the measured PT observables for the two 1^+ states in Eq. 1.17 results in a $|F|^2/|B|^2$ value of 7.4 ± 1.5 for isoscalar spin-flip transitions and 0.50 ± 0.02 for isovector spin-flip transitions. By using these values and Eq. 1.9 for $\Delta J{=}\Delta L + 1$ transitions, it is deduced that the quantity, $S_{LL} - S_{SS}$, takes a negative value for isoscalar spin-flip transitions, and takes a positive value for isovector spin-flip transitions with $\Delta L{=}0$ or 1, since the sign of $S_{LL} - S_{SS}$ is the same as that of $2 - \frac{X_L^2}{X_T^2} - \frac{|F|^2}{|B|^2}$ from Eq. 1.17. S_{LL}-S_{SS} exceptionally becomes -1 for both isoscalar and isovector 0^- transitions, because only the $\Delta J{=}\Delta L - 1$ part can contribute to 0^- transitions. For non-spin-flip transitions, S_{LL}-S_{SS} becomes zero. Fig. 5.14 plots $(S_{LL}\text{-}S_{SS})\frac{d\sigma}{d\Omega d\omega}$ as a function of the excitation energy. From the above discussion, it is expected that isoscalar spin-flip strengths appear in the negative side and isovector spin-flip strengths in the positive side except 0^- states. In fact, we observe negative values for the broad isoscalar resonance at 18.4 MeV [69]. The broad resonances at 19.5 MeV and at 22.5 MeV are considered to be the isobaric analogue

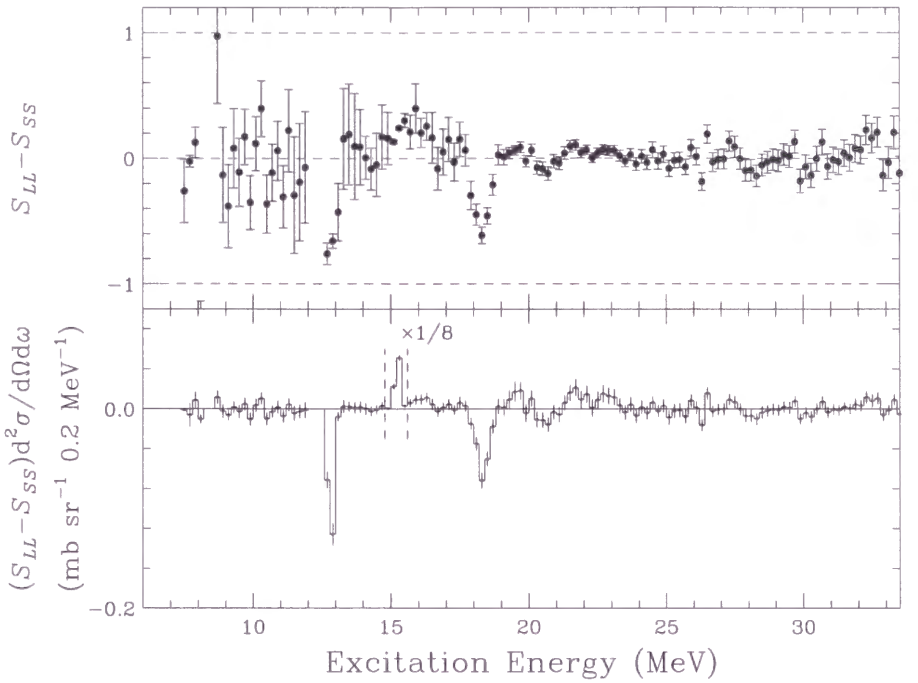

Figure 5.14: Measured S_{LL}-S_{SS} versus the excitation energy of ^{12}C.

states of the spin dipole resonances observed in charge exchange reactions [33, 70, 71]. Since the resonances have isovector nature, S_{LL}-S_{SS} takes positive values. In the figure, it is remarkable that an isoscalar spin-flip resonance is observed at 20.5 MeV. The state has recently been reported from the study of the ^{12}C$(\vec{d}, \vec{d}')$ reaction [72] and has not been observed in other reactions.

5.6 Future perspective

Now that the techniques to measure the PT observables in proton inelastic scattering at 0° have been established. Since we have obtained the parameters to describe the reaction mechanism, we can advance to the next step to survey structures of the nuclear spin-isospin excitations not only for discrete states but also for giant resonances and continuum.

Subsequent experiments, *e.g.* measuring ^{28}Si(p, p') at 0° have already performed. Pre-

liminary analysis of the ^{28}Si(p,p') reaction has revealed that the isospin decomposition technique can be properly applied to known 1^+ states.

One of the defects of the present 0° measurement is the large vertical acceptance of the spectrometer, which allowed protons with a scattering angle as large as 3° to be detected. In order to reduce the acceptance without decreasing the signal to noise ratio (S/N), active collimators made of plastic scintillators have been installed. By using the active collimators, background events due to the edge scattering at the collimator can be removed from the triggers by detecting the light output of the plastic scintillators. The ^{58}Ni(p,p') reaction has been successfully measured with the active collimators. In the experiment, charged particles emitted from excited ^{58}Ni nuclei have been measured by silicon detectors in coincidence. The analysis of the data is in progress. As the next experiment, study of the spin dipole resonances on ^{16}O nuclei by measuring 0° and extremely forward angle (p,p') reaction is planned.

Finally, I would like to conclude that the 0° (p,p') reaction is a powerful and promising probe to study the nuclear reaction and nuclear structures, and it will certainly shed a light on the way to the further interesting studies on nuclear physics.

Chapter 6

CONCLUSION

Polarization transfer (PT) observables, D_{SS} and D_{LL}, in ^{12}C(p,p') reaction at θ=0° and at E_p=392 MeV has been measured in a wide excitation energy region of 5–34 MeV. This is the first measurement of the PT observables in proton inelastic scattering at 0° in intermediate energy region. The experiment was performed by using a high resolution magnetic spectrometer, *Grand Raiden*, and a newly constructed focal plane polarimeter (FPP) at the Research Center for Nuclear Physics (RCNP).

The obtained PT observables for excitations of the 0^+, T=0 state at 7.65 MeV, the 1^+, T=0 at 12.7 MeV, and the 1^+, T=1 state at 15.1 MeV were compared with the predictions of the microscopic distorted wave impulse approximation (DWIA) calculations. The Franey and Love (FL) interaction, the Paris free (PF) interaction, and the Paris density-dependent (PD) interaction were employed as an elementary NN interaction. The PT observables, D_{SS} and D_{LL} for the 0^+ excitation were consistent with unity, which are determined by the axial symmetry and the conservation law of the total angular momentum. The isoscalar spin-dependent term (V_σ) of the effective interaction was first observed by measuring the PT observables for the 1^+, T=0 excitation. It was shown that the FL interaction surprisingly well describes the strength of the V_σ term even though it had been poorly determined from NN scattering data. The FL interaction reproduces the PT observables for the 1^+, T=1 excitation. The PF and PD interactions fail to reproduce the PT observables for both the 1^+ states. The disagreement means an improper

description of the strengths of the tensor terms and the isoscalar spin-dependent term in the PF and PD interactions.

A better set of parameters of the effective interactions were studied by modifying the FL and PF interactions to fit the experimental data. The shortest-range part of the real V_τ^T term and the real V_0^T term were modified to reproduce the PT observables for the 1^+, T=1 excitation and the relative differential cross section of the two 1^+ states. The longest-range part of the real V_σ term was modified to reproduce the PT observables for the 1^+, T=0 excitation.

It was demonstrated that the PT observables were powerful probes to study spin-isospin structure of the strengths in the continuum region as well as discrete states. The spin-flip and non-spin-flip strengths in ^{12}C were decomposed by using total spin transfers. We found that the broad structures at 18.4 MeV and at 19.5 MeV consist predominantly of spin-flip strengths, while the broad structure at 22.5 MeV consist of both spin-flip and non-spin-flip strengths. The ratio of the spin-flip strengths to the non-spin-flip strengths gradually increases above the giant resonance region. It was shown that the quantity S_{LL}-S_{SS} takes a positive value for isovector spin-flip strengths and a negative value for isoscalar spin-flip strengths. The selectivity was well confirmed for known spin-flip strengths on ^{12}C, *e.g.* isoscalar spin-flip strength at 18.5 MeV and isovector spin-flip strengths at 19.5 MeV and 22.5 MeV. The isoscalar spin-flip strength at 20.5 MeV, which has been reported from the study of the ^{12}C$(\vec{d}, \vec{d}')$ reaction, has been first observed via the (p, p') experiment.

The experimental technique to measure the PT observables in proton inelastic scattering at 0° has been established. It was confirmed that the PT observables at 0° are powerful and promising probes for the study on nuclear reaction as well as spin-isospin resonances in nuclei.

Chapter 7

ACKNOWLEDGEMENTS

I would like to express my sincere gratitude to Prof. M. Yosoi. He has continuously encouraged, advised, and supported me at every stage of the work: planning, experiment, analysis, and publication. I have been deeply influenced from his gratitude to the study of science and physics.

I am gratefully acknowledge Prof. H. Sakaguchi, who gave me an opportunity to study experimental nuclear physics, and has also been supported me at any stage of the work.

I would like to appreciate helpful discussions with Prof. K. Imai. He encouraged me to brush up the physical insights and complete the doctoral dissertation.

I am grateful to Prof. H. Sakai, who have encouraged me to complete the doctoral work, and now collaborates with me and gives me many suggestions on study of physics.

I deeply appreciate the valuable discussion with Prof. Toru Suzuki on the reaction mechanism and how to interpret the physics of this experiment.

I express many thanks to Prof M. Fujiwara. He gave me many suggestions and discussions about the experiment, and a lot of advice to brush up the manuscript of the publication. I also acknowledge Prof. Y. Fujita for advice to the manuscript.

I would like to thank Mr. T. Kawabata, who have joined this experimental study and helped lot of parts in the experiment. He is now performing further studies related to this work.

The success of this challenging experiment was deeply owing to the beautiful tuning technique of the proton beam by Prof. K. Hatanaka. I appreciate his great work and the continuous efforts of the RCNP cyclotron staff to get an excellent low-halo and stable beam.

This work was much stimulated from the former work on measuring (p, p') cross sections at $0°$, which was mainly performed by Dr. Y. Sakemi and Dr. H. Akimune. I would like to acknowledge their great work and many suggestions and helps for the present study.

I am thankful to all the collaborators of the RCNP-E96 experiment: Dr. H. Akimune, Dr. I. Daito, Prof. Y. Fujita, Prof. M.Fujiwara, Prof.. K. Hatanaka, Prof. K. Hosono, Mr. F. Ihara, Dr. T. Inomata, Mr. T. Ishikawa, Mr. M. Itoh, Dr. M. Kawabata, Mr. T. Kawabata, Prof. M. Nakamura, Prof. T. Noro, Ms. E. Obayashi, Prof. H. Sakaguchi, Mr. H. Takeda, Ms. T. Taki, Dr. H. Toyokawa, Mr. H.P. Yoshida, Mr. M. Yoshimura, and Prof. M. Yosoi.

I am grateful to Dr. Bachir Kharraja for the comments on this dissertation. I would like to thank the members of the experimental nuclear studies at Kyoto University for lot of helps, advice and supports during my graduate studies. I am grateful to the members of the Research Center for Nuclear Physics for various supports and discussions for my research. I acknowledge the staff and the students of Sakai-group, Ishihara-group and Hayano-group for my study and enjoyable life at the University of Tokyo.

Finally, I would like to express my great thanks to my parents, sister, grandmother, and late grandfather for their continuous supports.

Appendix A

EXPERIMENTAL RESULTS

The experimental results of double differential cross sections, D_{SS}, and D_{LL} in the $^{12}C(p,p')$ reaction at 0° are summarized in a tabular form.

Table A.1:

E_x (MeV)	$d\sigma/d\Omega$ (μb sr^{-1} 0.2 MeV^{-1})	D_{SS}	D_{LL}
5.1	17.55 ± 0.82	——	——
5.3	18.85 ± 0.85	——	——
5.5	19.80 ± 0.87	——	——
5.7	5.11 ± 0.44	——	——
5.9	2.94 ± 0.33	——	——
6.1	1.30 ± 0.22	——	——
6.3	4.31 ± 0.41	——	——
6.5	3.17 ± 0.35	——	——
6.7	3.81 ± 0.38	——	——
6.9	3.66 ± 0.37	——	——
7.1	2.21 ± 0.29	——	——
7.3	2.67 ± 0.32	——	——
7.5	4.50 ± 0.41	0.480 ± 0.341	1.002 ± 0.369
7.7	258.90 ± 3.14	1.003 ± 0.062	1.050 ± 0.069
7.9	68.67 ± 1.62	1.016 ± 0.175	0.763 ± 0.170
8.1	5.57 ± 0.46	-1.764 ± 1.000	1.953 ± 1.044
8.3	9.31 ± 0.60	——	——
8.5	10.22 ± 0.62	——	——
8.7	12.02 ± 0.68	1.737 ± 0.726	-0.205 ± 0.783
8.9	17.62 ± 0.82	0.349 ± 0.527	0.614 ± 0.544
9.1	16.79 ± 0.80	-0.056 ± 0.455	0.705 ± 0.480

E_x (MeV)	$d\sigma/d\Omega$ (μb sr^{-1} 0.2 MeV^{-1})	D_{SS}	D_{LL}
9.3	18.77 ± 0.85	1.431 ± 0.438	1.271 ± 0.456
9.5	24.07 ± 0.96	0.658 ± 0.377	0.877 ± 0.393
9.7	28.54 ± 1.04	1.147 ± 0.310	0.804 ± 0.313
9.9	29.03 ± 1.05	0.105 ± 0.298	0.807 ± 0.308
10.1	29.83 ± 1.07	1.368 ± 0.306	1.132 ± 0.306
10.3	25.90 ± 0.99	1.626 ± 0.310	0.831 ± 0.320
10.5	27.43 ± 1.02	0.441 ± 0.329	1.168 ± 0.329
10.7	25.48 ± 0.99	0.637 ± 0.324	0.863 ± 0.322
10.9	26.25 ± 1.00	1.052 ± 0.331	0.929 ± 0.335
11.1	24.00 ± 0.96	0.422 ± 0.351	1.033 ± 0.353
11.3	19.00 ± 0.85	1.228 ± 0.458	0.783 ± 0.469
11.5	15.49 ± 0.77	0.816 ± 0.663	1.400 ± 0.653
11.7	14.15 ± 0.73	-0.110 ± 0.649	0.267 ± 0.675
11.9	17.47 ± 0.82	0.751 ± 0.620	0.894 ± 0.637
12.1	13.01 ± 0.70	——	——
12.3	11.03 ± 0.65	——	——
12.5	12.40 ± 0.69	——	——
12.7	93.85 ± 1.89	-0.700 ± 0.119	0.820 ± 0.126
12.9	191.50 ± 2.70	-0.572 ± 0.076	0.743 ± 0.087
13.1	18.73 ± 0.85	-0.333 ± 0.347	0.522 ± 0.297
13.3	15.53 ± 0.77	0.455 ± 0.569	0.143 ± 0.564
13.5	11.71 ± 0.67	0.848 ± 0.574	0.464 ± 0.560
13.7	12.86 ± 0.70	0.649 ± 0.563	0.458 ± 0.628
13.9	17.93 ± 0.83	0.811 ± 0.418	0.630 ± 0.432
14.1	33.42 ± 1.13	0.537 ± 0.234	0.525 ± 0.249
14.3	30.10 ± 1.07	0.850 ± 0.226	1.018 ± 0.245
14.5	17.55 ± 0.82	0.960 ± 0.347	1.059 ± 0.366
14.7	16.56 ± 0.79	0.439 ± 0.364	0.097 ± 0.359
14.9	17.21 ± 0.81	0.278 ± 0.358	-0.042 ± 0.214
15.1	1354.00 ± 7.19	-0.287 ± 0.020	-0.554 ± 0.022
15.3	1686.00 ± 8.02	-0.076 ± 0.017	-0.563 ± 0.018
15.5	80.57 ± 1.75	0.129 ± 0.081	-0.477 ± 0.078
15.7	28.69 ± 1.05	0.286 ± 0.198	-0.139 ± 0.182
15.9	23.23 ± 0.94	0.987 ± 0.286	0.190 ± 0.270
16.1	46.43 ± 1.33	0.336 ± 0.163	-0.073 ± 0.170
16.3	44.33 ± 1.30	0.566 ± 0.150	0.051 ± 0.163
16.5	27.20 ± 1.02	0.530 ± 0.283	0.197 ± 0.290
16.7	28.96 ± 1.05	0.427 ± 0.233	0.589 ± 0.250
16.9	27.09 ± 1.02	0.923 ± 0.249	0.820 ± 0.269
17.1	30.25 ± 1.07	0.397 ± 0.238	0.094 ± 0.257
17.3	30.44 ± 1.08	0.537 ± 0.202	0.596 ± 0.224
17.5	41.16 ± 1.25	0.562 ± 0.187	0.258 ± 0.202

E_x (MeV)	$d\sigma/d\Omega$ (μb sr^{-1} 0.2 MeV^{-1})	D_{SS}	D_{LL}
17.7	45.70 ± 1.32	0.752 ± 0.172	0.623 ± 0.182
17.9	50.13 ± 1.38	0.271 ± 0.154	0.862 ± 0.167
18.1	77.90 ± 1.72	-0.309 ± 0.116	0.586 ± 0.123
18.3	117.00 ± 2.11	-0.434 ± 0.088	0.793 ± 0.095
18.5	109.60 ± 2.04	-0.237 ± 0.088	0.678 ± 0.097
18.7	83.32 ± 1.78	0.172 ± 0.113	0.593 ± 0.124
18.9	92.32 ± 1.88	0.333 ± 0.110	0.278 ± 0.119
19.1	140.70 ± 2.32	0.109 ± 0.084	0.089 ± 0.090
19.3	225.20 ± 2.93	0.048 ± 0.060	-0.036 ± 0.065
19.5	270.60 ± 3.21	0.004 ± 0.052	-0.123 ± 0.056
19.7	208.40 ± 2.82	0.074 ± 0.057	-0.101 ± 0.062
19.9	190.20 ± 2.69	0.020 ± 0.062	0.064 ± 0.068
20.1	163.60 ± 2.50	0.343 ± 0.066	0.215 ± 0.074
20.3	144.60 ± 2.35	0.373 ± 0.072	0.521 ± 0.078
20.5	134.90 ± 2.27	0.406 ± 0.075	0.573 ± 0.081
20.7	128.80 ± 2.22	0.409 ± 0.074	0.651 ± 0.081
20.9	127.60 ± 2.21	0.423 ± 0.074	0.472 ± 0.082
21.1	140.80 ± 2.32	0.451 ± 0.070	0.530 ± 0.076
21.3	152.20 ± 2.41	0.617 ± 0.067	0.535 ± 0.073
21.5	170.00 ± 2.55	0.645 ± 0.063	0.453 ± 0.067
21.7	199.80 ± 2.76	0.598 ± 0.056	0.384 ± 0.062
21.9	217.30 ± 2.88	0.486 ± 0.054	0.398 ± 0.058
22.1	222.30 ± 2.91	0.509 ± 0.051	0.376 ± 0.057
22.3	220.30 ± 2.90	0.520 ± 0.052	0.510 ± 0.057
22.5	219.50 ± 2.89	0.459 ± 0.051	0.376 ± 0.057
22.7	222.00 ± 2.91	0.543 ± 0.052	0.405 ± 0.056
22.9	212.00 ± 2.84	0.510 ± 0.051	0.388 ± 0.057
23.1	191.40 ± 2.70	0.597 ± 0.056	0.475 ± 0.061
23.3	172.70 ± 2.57	0.589 ± 0.060	0.548 ± 0.065
23.5	157.80 ± 2.45	0.555 ± 0.061	0.600 ± 0.068
23.7	150.80 ± 2.40	0.572 ± 0.064	0.515 ± 0.070
23.9	141.50 ± 2.32	0.498 ± 0.067	0.591 ± 0.074
24.1	123.50 ± 2.17	0.515 ± 0.071	0.485 ± 0.079
24.3	115.00 ± 2.10	0.476 ± 0.078	0.542 ± 0.085
24.5	98.65 ± 1.94	0.541 ± 0.084	0.408 ± 0.092
24.7	94.76 ± 1.90	0.478 ± 0.088	0.521 ± 0.097
24.9	95.18 ± 1.91	0.478 ± 0.091	0.414 ± 0.096
25.1	106.40 ± 2.01	0.426 ± 0.088	0.589 ± 0.094
25.3	113.10 ± 2.08	0.426 ± 0.082	0.460 ± 0.090
25.5	113.30 ± 2.08	0.409 ± 0.082	0.433 ± 0.090
25.7	108.90 ± 2.04	0.208 ± 0.084	0.347 ± 0.092
25.9	98.84 ± 1.94	0.582 ± 0.087	0.416 ± 0.096

E_x (MeV)	$d\sigma/d\Omega$ (μb sr^{-1} 0.2 MeV^{-1})	D_{SS}	D_{LL}
26.1	93.31 ± 1.89	0.431 ± 0.090	0.406 ± 0.100
26.3	87.28 ± 1.82	0.228 ± 0.094	0.599 ± 0.103
26.5	81.60 ± 1.76	0.614 ± 0.099	0.228 ± 0.107
26.7	78.17 ± 1.73	0.313 ± 0.100	0.375 ± 0.110
26.9	74.28 ± 1.68	0.355 ± 0.104	0.372 ± 0.111
27.1	77.18 ± 1.72	0.355 ± 0.107	0.366 ± 0.116
27.3	67.45 ± 1.60	0.460 ± 0.110	0.185 ± 0.118
27.5	73.70 ± 1.68	0.242 ± 0.113	0.059 ± 0.123
27.7	68.67 ± 1.62	0.274 ± 0.117	0.279 ± 0.125
27.9	72.33 ± 1.66	0.314 ± 0.117	0.509 ± 0.125
28.1	74.50 ± 1.69	0.310 ± 0.119	0.498 ± 0.126
28.3	68.94 ± 1.62	0.134 ± 0.117	0.416 ± 0.126
28.5	68.06 ± 1.61	0.210 ± 0.118	0.317 ± 0.127
28.7	65.81 ± 1.58	0.210 ± 0.118	0.270 ± 0.126
28.9	66.68 ± 1.59	0.467 ± 0.114	0.484 ± 0.129
29.1	63.94 ± 1.56	0.160 ± 0.117	0.195 ± 0.128
29.3	62.68 ± 1.55	0.332 ± 0.115	0.269 ± 0.128
29.5	65.31 ± 1.58	0.283 ± 0.120	0.253 ± 0.130
29.7	57.38 ± 1.48	0.339 ± 0.122	0.072 ± 0.135
29.9	55.54 ± 1.46	0.309 ± 0.126	0.669 ± 0.139
30.1	59.89 ± 1.51	0.281 ± 0.128	0.417 ± 0.139
30.3	58.98 ± 1.50	0.339 ± 0.130	0.608 ± 0.144
30.5	57.95 ± 1.49	0.471 ± 0.134	0.476 ± 0.145
30.7	54.36 ± 1.44	0.417 ± 0.138	0.155 ± 0.150
30.9	54.97 ± 1.45	0.356 ± 0.136	0.482 ± 0.148
31.1	54.44 ± 1.44	0.178 ± 0.135	0.199 ± 0.151
31.3	54.36 ± 1.44	0.202 ± 0.141	0.254 ± 0.152
31.5	50.39 ± 1.39	0.354 ± 0.144	0.270 ± 0.155
31.7	48.68 ± 1.36	0.405 ± 0.142	0.395 ± 0.158
31.9	53.87 ± 1.43	0.453 ± 0.148	0.296 ± 0.161
32.1	46.58 ± 1.33	0.184 ± 0.148	0.050 ± 0.167
32.3	50.85 ± 1.39	0.412 ± 0.157	-0.041 ± 0.170
32.5	50.28 ± 1.39	0.468 ± 0.162	0.144 ± 0.172
32.7	50.47 ± 1.39	0.245 ± 0.161	-0.170 ± 0.175
32.9	45.51 ± 1.32	0.129 ± 0.167	0.400 ± 0.183
33.1	39.87 ± 1.23	0.192 ± 0.175	0.258 ± 0.187
33.3	43.34 ± 1.29	0.410 ± 0.180	-0.003 ± 0.190
33.5	44.60 ± 1.30	0.161 ± 0.183	0.397 ± 0.202
33.7	41.32 ± 1.26	0.376 ± 0.195	0.094 ± 0.247

Appendix B

SPIN PRECESSION IN A MAGNETIC FIELD

B.1 Spin precession in a uniform magnetic field

If the velocity of a proton is perpendicular to a uniform magnetic field, **B**, the time evolution of the polarization vector, **p** of the proton is written according to the equation (11.170) of Ref.[73] as

$$\frac{d\mathbf{p}}{dt} = \frac{e}{M_p c}\mathbf{p} \times (\frac{g_p}{2} - 1 + \frac{1}{\gamma})\mathbf{B}, \tag{B.1}$$

where g_p=5.585 is the gyromagnetic ratio of a proton (Landè g factor), and γ has the usual meaning ($\gamma = \frac{1}{\sqrt{1-\beta^2}}$) in the special theory of relativity. From (B.1), the polarization vector precesses along **B** keeping its magnitude (Thomas precession) with a constant frequency of

$$\omega_p = \frac{e}{M_p c}(\frac{g_p}{2} - 1 + \frac{1}{\gamma})B. \tag{B.2}$$

The equation of motion for the proton is

$$\gamma M_p \frac{d\mathbf{v}}{dt} = \frac{e}{c}\mathbf{v} \times \mathbf{B} \tag{B.3}$$

from the equation (12.37) of Ref. [73], where the protons velocity is denoted by **v**. The magnitude of the velocity is constant, and the direction rotate along the magnetic field with a constant frequency of

$$\omega_v = \frac{e}{\gamma M_p c}B. \tag{B.4}$$

I denote the rotation angle of the perpendicular component of the polarization vector relative to the direction of the velocity by θ_p, and the rotation angle of the velocity vector by θ_v. From (B.2) and (B.4), θ_p can be written by θ_v as

$$\begin{aligned} \theta_p &= (\omega_p - \omega_v)t \\ &= \frac{e}{M_p c}(\frac{g_p}{2} - 1)Bt \\ &= \gamma(\frac{g_p}{2} - 1)\omega_v t \\ &= \gamma(\frac{g_p}{2} - 1)\theta_v. \end{aligned} \tag{B.5}$$

B.2 Simulation of the spin precession in Grand Raiden

To be precise, a simulation of the spin rotation in the Grand Raiden was performed. At first particle trajectory in the Grand Raiden was simulated by using an ion-optical simulation code *RAYTRACE* [74]. Input parameters are taken from [75] and are listed in Table.B.1. Spin rotation matrices is simply calculated from the variation of the momentum vector output by *RAYTRACE*. The spin rotation matrices are fitted by 2nd-order polynomials of the horizontal scattering angle θ_s and the vertical scattering vertical scattering angle ϕ_s as

$$\begin{pmatrix} p''_{S''} \\ p''_{N''} \\ p''_{L''} \end{pmatrix} = R_x(\phi'_s)R_y(\theta'_s) \begin{pmatrix} p''_{x''} \\ p''_{y''} \\ p''_{z''} \end{pmatrix} \tag{B.6}$$

$$= R_x(\phi'_s)R_y(\theta'_s)MR_y(\delta'_b) \begin{pmatrix} p'_x \\ p'_y \\ p'_z \end{pmatrix},$$

$$\begin{aligned} M &= \begin{pmatrix} 1 - 43.87\theta_s^2 & 0 & -8.608\theta_s \\ 0 & 1 & 0 \\ 8.608\theta_s & 0 & 1 - 43.87\theta_s^2 \end{pmatrix} \\ &\times \begin{pmatrix} 1 - 4.200\phi_s^2 & 2.880\phi_s & -1.437\phi_s^2 \\ -2.880\phi_s & 1 - 0.501\phi_s^2 & -1.287\phi_s \\ -2.284\phi_s^2 & 1.284\phi_s & 1 - 0.847\phi_s^2 \end{pmatrix}. \end{aligned} \tag{B.7}$$

By averaging the polarization in the acceptance of the Grand Raiden, such that $-\theta_s^{max} \leq \theta_s \leq \theta_s^{max}$ and $-\phi_s^{max} \leq \phi_s \leq \phi_s^{max}$, where $-\theta_s^{max} = 1.00°$ and $-\theta_s^{max} = 2.9°$, Eq.(B.6)

becomes

$$\begin{pmatrix} \overline{p''_{S''}} \\ \overline{p''_{N''}} \\ \overline{p''_{L''}} \end{pmatrix} = \overline{M'} R_y(\delta'_b) \begin{pmatrix} p'_x \\ p'_y \\ p'_z \end{pmatrix}.$$

$$\overline{M'} \equiv \overline{R_x(\phi'_s) R_y(\theta'_s) M} \sim \begin{pmatrix} 0.9914 & 0 & -0.0013 \\ 0 & 0.9995 & 0 \\ -0.0021 & 0 & 0.9944 \end{pmatrix}. \quad \text{(B.8)}$$

The result is reasonably consistent with the rough estimations by by Eq. (C.19) and (C.20).

Table B.1: Input parameters for ion-optical calculations

	Q1	SX	Q2	D1	MP	D2	DSR
Field	-0.643	7.60	0.080	10.15	0.00	10.15	1.457
	(kG/cm)	(G/cm^2)	(kG/cm)	(kG)		(kG)	(kG)
Length	60 cm	20 cm	30 cm				
Entrance angle				0.0°		40.0°	-7.5°
Exit angle				30.0°		36.7°	11.9°
Bending angle				0.0°		102.0°	1.7°
C1	0.476		0.476	0.3627		0.2662	0.0755
C2	5.98		5.98	1.3670		1.5122	1.9614
C3	-5.61		-5.61	-0.4841		-0.4869	-0.1985
C4	2.2		2.2	0.2197		0.2654	0.4537
C5	0.0		0.0	-0.0086		0.1956	-0.0115
C6	0.0		0.0	-0.0007		0.0014	0.0392
S02				0.0		0.0	0.0
S03				-6.9248		0.0856	0.0
S04				0.0		-0.0604	0.0
S05				0.0		-0.0052	0.0
S06				0.0		0.0	0.0
S12				0.0		0.0	0.0
S13				-1.3047		0.0535	0.0
S14				0.0088		-0.0348	0.0
S15				0.0		-0.0117	0.0
S16				0.0		0.0	0.0
RAP1				0.0		0.0023	0.001
RAP2				0.00083		-0.0013	0.0

Table B.2: Sample results of the ion-optics calculations (1)

Element	Bending angle	x_s (cm)	θ_s (mr)	y_s (cm)	ϕ_s (mr)	spin rotation matrix
Target		0.0	1.750	0.000	0.000	$\begin{pmatrix} 1.0000 & 0.0000 & 0.0000 \\ 0.0000 & 1.0000 & 0.0000 \\ 0.0000 & 0.0000 & 1.0000 \end{pmatrix}$
Q1	0.0					
		0.402	4.435	0.000	0.000	$\begin{pmatrix} 1.0000 & 0.0000 & -0.0068 \\ 0.0000 & 1.0000 & 0.0000 \\ 0.0068 & -0.0000 & 1.0000 \end{pmatrix}$
SX	0.0					
		0.668	4.421	0.000	0.000	$\begin{pmatrix} 1.0000 & 0.0000 & -0.0068 \\ 0.0000 & 1.0000 & 0.0000 \\ 0.0068 & -0.0000 & 1.0000 \end{pmatrix}$
Q2	0.0					
		0.956	3.802	0.000	0.000	$\begin{pmatrix} 1.0000 & 0.0000 & -0.0052 \\ 0.0000 & 1.0000 & 0.0000 \\ 0.0052 & -0.0000 & 1.0000 \end{pmatrix}$
D1	60.0					
		1.604	1.592	0.000	0.000	$\begin{pmatrix} -0.8873 & -0.0000 & 0.4612 \\ 0.0000 & 1.0000 & 0.0000 \\ -0.4612 & 0.0000 & -0.8873 \end{pmatrix}$
MP	0.0					
		1.756	1.592	0.000	0.000	$\begin{pmatrix} -0.8873 & -0.0000 & 0.4612 \\ 0.0000 & 1.0000 & 0.0000 \\ -0.4612 & 0.0000 & -0.8873 \end{pmatrix}$
D2	102.0					
		0.977	-4.183	0.000	0.000	$\begin{pmatrix} 0.6067 & -0.0000 & 0.7949 \\ 0.0000 & 1.0000 & 0.0000 \\ -0.7949 & -0.0000 & 0.6067 \end{pmatrix}$
DSR	1.7					
F.P.		0.059	-4.167	0.000	0.000	$\begin{pmatrix} 0.5443 & -0.0000 & 0.8389 \\ -0.0000 & 1.0000 & 0.0000 \\ -0.8389 & -0.0000 & 0.5443 \end{pmatrix}$

Table B.3: Sample results of the ion-optics calculations (2)

Element	Bending angle	x_s (cm)	θ_s (mr)	y_s (cm)	ϕ_s (mr)	spin rotation matrix
Target		0.0	0.000	0.000	1.750	$\begin{pmatrix} 1.0000 & 0.0000 & 0.0000 \\ 0.0000 & 1.0000 & 0.0000 \\ 0.0000 & 0.0000 & 1.0000 \end{pmatrix}$
Q1	0.0					
		0.000	0.000	0.174	-0.411	$\begin{pmatrix} 1.0000 & 0.0000 & 0.0000 \\ 0.0000 & 1.0000 & -0.0055 \\ -0.0000 & 0.0055 & 1.0000 \end{pmatrix}$
SX	0.0					
		0.000	-0.001	0.150	-0.411	$\begin{pmatrix} 1.0000 & -0.0000 & -0.0000 \\ 0.0000 & 1.0000 & -0.0055 \\ 0.0000 & 0.0055 & 1.0000 \end{pmatrix}$
Q2	0.0					
		-0.000	-0.001	0.124	-0.309	$\begin{pmatrix} 1.0000 & -0.0000 & -0.0000 \\ 0.0000 & 1.0000 & -0.0052 \\ 0.0000 & 0.0052 & 1.0000 \end{pmatrix}$
D1	60.0					
		-0.000	-0.001	0.006	-0.328	$\begin{pmatrix} -0.8871 & 0.0024 & 0.4615 \\ 0.0000 & 1.0000 & -0.0052 \\ -0.4616 & -0.0046 & -0.8871 \end{pmatrix}$
MP	0.0					
		-0.001	-0.001	-0.026	-0.328	$\begin{pmatrix} -0.8871 & 0.0024 & 0.4615 \\ 0.0000 & 1.0000 & -0.0052 \\ -0.4616 & -0.0046 & -0.8871 \end{pmatrix}$
D2	102.0					
		-0.000	0.002	-0.091	0.245	$\begin{pmatrix} 0.6186 & 0.0048 & 0.7857 \\ -0.0009 & 1.0000 & -0.0054 \\ -0.7857 & 0.0027 & 0.6186 \end{pmatrix}$
DSR	1.7					
F.P.		0.000	0.002	-0.037	0.247	$\begin{pmatrix} 0.5568 & 0.0050 & 0.8306 \\ -0.0009 & 1.0000 & -0.0054 \\ -0.8306 & 0.0023 & 0.5568 \end{pmatrix}$

Appendix C

CORRECTION FOR FINITE ANGLE SCATTERING

C.1 Overview

In the case of proton inelastic scattering scattering from a spin-zero target nucleus at 0°, three PT observables, D_{SS}, D_{NN} and D_{LL}, remain no zero. Since D_{SS} equals to D_{NN} from the rotational symmetry, independent PT observables are two: *i.e.* D_{SS} (or D_{NN}) and D_{LL}. In Chap. 3, the two PT observables, D_{SS} and D_{LL}, have been deduced from the beam polarization and the polarization of the scattered particles by using a simple equation (Eq. 3.35) which holds at exact 0°. But in actual, the scattered protons measured by the FPP is not only scattered at 0° but also scattered at small finite angles, since the solid angle of the spectrometer must have a finite acceptance. Hence, the following points should be incorporated properly, in order to compare the experimental results with theoretical predictions.

1. The normal direction of the scattering plane is not always vertical but depends on the azimuthal scattering angle in the acceptance.

2. The spin-precession angle in *Grand Raiden* depends on the the horizontal scattering angle.

3. The measured polarization is an average polarization in the acceptance weighted by the differential cross sections.

In this appendix, the first order contributions from the finite scattering angles are discussed.

The sections proceed as follows.

C.2 Definition of coordinate systems.

C.3 Transformation of the beam polarization from the experimental room coordinate system (p_x, p_y, p_z) to the reaction coordinate system (p_S, p_N, p_L).

C.4 Relation between the beam polarization (p_S, p_N, p_L) and the polarization of scattered protons ($p'_{S'}$, $p'_{N'}$, $p'_{L'}$).

C.5 Transformation of the polarization of the scattered protons from the reaction coordinate system ($p'_{S'}$, $p'_{N'}$, $p'_{L'}$) to the experimental room coordinate system (p'_x, p'_y, p'_z).

C.6 Relation between the polarization of the scattered protons (p'_x, p'_y, p'_z) and the polarization at the focal plane polarimeter ($p''_{S''}$, $p''_{N''}$, $p''_{L''}$) incorporating the spin precession in the spectrometer.

C.7 Summary of the finite angle correction.

The discussions are based on the assumptions:

- Scattering angles are small ($\theta \ll 0.1$).
- The acceptance of the spectrometer is symmetric about the vertical axis ($-\theta_s^{max} \leq \theta_s \leq \theta_s^{max}$) and the horizontal axis ($-\phi_s^{max} \leq \phi_s \leq \phi_s^{max}$).

I note that averaging in the acceptance can be taken at any stage separately, since only the first order contributions are Des-cussed.

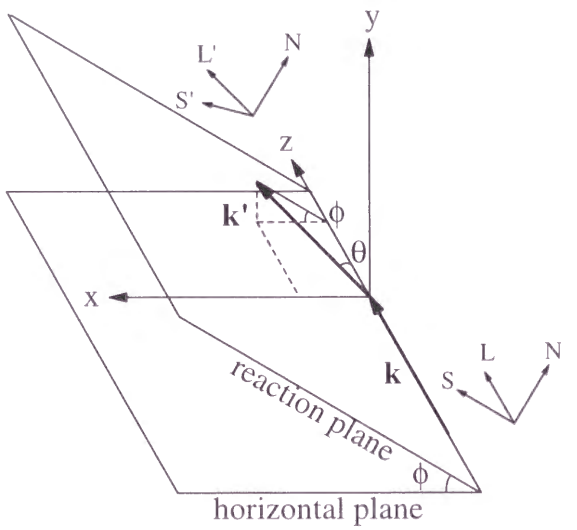

Figure C.1: Coordinate system used in the analysis of the ^{12}C(p,p') reaction in the laboratory frame. **x**, **y**, and **z** are the unit vectors in the coordinate system fixed at the experimental room. **N**(=**N**′) is a unit vector perpendicular to the reaction plane. **L** (**L**′) is a unit vector parallel to the incoming (outgoing) momentum vector **k**(**k**′). **S** (**S**′), **N** (**N**′), and **L** (**L**′) form a right handed coordinate system for incoming (outgoing) protons.

C.2 Coordinate systems

Coordinate systems at the reaction target in the laboratory frame are illustrated in Fig. C.1 **k** (**k**′) denotes the incoming (outgoing) proton momentum. The coordinate system which is fixed to the experimental room is defined as follows.

[Experimental room coordinate system]

- Take **z** along the incoming proton momentum.
- Take **y** along the vertical direction.
- **x** is defined as unit vectors, **x**, **y**, and **z**, form a right-handed cartesian coordinate system.

Two cartesian coordinate systems, which are fixed to the reaction plane, are defined as follows.

[Incoming proton coordinate system]

$$\mathbf{N} = \frac{\mathbf{k} \times \mathbf{k}'}{|\mathbf{k} \times \mathbf{k}'|}, \quad \mathbf{L} = \frac{\mathbf{k}}{|\mathbf{k}|}, \quad \mathbf{S} = \frac{\mathbf{N} \times \mathbf{L}}{|\mathbf{N} \times \mathbf{L}|} \tag{C.1}$$

[Outgoing proton coordinate]

$$\mathbf{N}' = \mathbf{N} = \frac{\mathbf{k} \times \mathbf{k}'}{|\mathbf{k} \times \mathbf{k}'|}, \quad \mathbf{L}' = \frac{\mathbf{k}'}{|\mathbf{k}'|}, \quad \mathbf{S}' = \frac{\mathbf{N}' \times \mathbf{L}'}{|\mathbf{N}' \times \mathbf{L}'|} \tag{C.2}$$

The laboratory scattering angle, θ, is defined as the relative angle between the momenta, $\mathbf{k}$ and $\mathbf{k}'$. The azimuthal angle, ϕ, is measured from the x-axis.

For ion-optical calculations of the *Grand Raiden* spectrometer, the horizontal scattering angle, θ_s, and the vertical scattering angle, ϕ_s, are defined as

$$\begin{aligned} \tan\theta_s &\equiv \frac{-k'_x}{k'_z} = -\tan\theta\cos\phi, \quad (-\frac{\pi}{2} \le \theta_s \le \frac{\pi}{2}), \\ \tan\phi_s &\equiv \frac{k'_y}{k'_z} = \tan\theta\sin\phi \quad (-\frac{\pi}{2} \le \phi_s \le \frac{\pi}{2}). \end{aligned} \tag{C.3}$$

The sign of θ_s is chosen to be consistent with the definition of 'θ' used in the ion-optical calculation codes RAYTRACE [74]. The definition of the ϕ_s is slightly different from the definition in RAYTRACE:

$$\tan\phi_{\text{RAYTRACE}} = \frac{k'_y}{\sqrt{k'^2_x + k'^2_z}} \ . \tag{C.4}$$

The difference can be neglected in the first order calculation on θ_s and ϕ_s.

At the focal plane of the spectrometer, two coordinate systems are defined as

[Focal plane coordinate]

- For each proton momentum, the unit vector, $\mathbf{z}''$, is taken along the momentum of protons scattered at exact 0°.
- $\mathbf{y}''$ is taken along the vertical direction.
- $\mathbf{x}''$ is defined as the unit vectors $\mathbf{x}''$, $\mathbf{y}''$, and $\mathbf{z}''$ form a right-handed cartesian coordinate system.

[Focal plane polarimeter (FPP) coordinate]

- $\mathbf{L}''$ is taken along the momentum $\mathbf{k}''$.
- Determine α and β which satisfy the equation:

$$\mathbf{L}'' = R_{y''}(\alpha)R_{x''}(\beta)\mathbf{z}'' \quad (-\frac{\pi}{2} \leq \alpha \leq \frac{\pi}{2},\ -\frac{\pi}{2} \leq \beta \leq \frac{\pi}{2}). \tag{C.5}$$

  where $R_i(\phi_i)$ is the three-dimensional rotation matrix along the i-axis.

- $\mathbf{S}''$ and $\mathbf{N}''$ are defined by using the rotation matrix which relates $\mathbf{z}''$ to $\mathbf{L}''$ as

$$\begin{aligned} \mathbf{S}'' &= R_{y''}(\alpha)R_{x''}(\beta)\mathbf{x}''. \\ \mathbf{N}'' &= R_{y''}(\alpha)R_{x''}(\beta)\mathbf{y}''. \end{aligned} \tag{C.6}$$

The horizontal angle and the vertical angle from the z''-axis at the focal plane are defined as

$$\begin{aligned} \tan\theta'_s &\equiv \frac{-k''_x}{k''_z}. \\ \tan\phi'_s &\equiv \frac{k''_y}{k''_z}. \end{aligned} \tag{C.7}$$

θ'_s (ϕ'_s) at the focal plane is related to θ_s (ϕ_s) at the reaction target, by the first order ion-optical parameters as

$$\begin{aligned} \theta'_s &= (\theta'|\theta)\,\theta_s = \frac{1}{-0.417}\,\theta_s. \\ \phi'_s &= (\phi'|\phi)\,\phi_s = \frac{1}{5.98}\,\phi_s. \end{aligned} \tag{C.8}$$

C.3 Polarization of the beam in the reaction coordinate system

The polarization of the beam in the coordinate system fixed to the reaction plane is expressed by that in the coordinate system fixed to the experimental room as.

$$\begin{pmatrix} p_S \\ p_N \\ p_L \end{pmatrix} = R_z(-\phi) \begin{pmatrix} p_x \\ p_y \\ p_z \end{pmatrix}$$

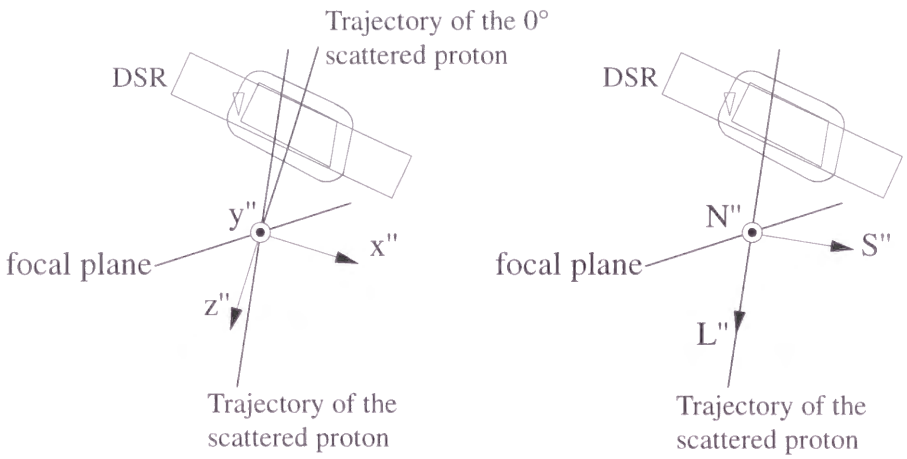

Figure C.2: The focal plane coordinate system (Left) and the focal plane polarimeter coordinate system (Right). In the left panel, $\mathbf{z}''$ is taken to be parallel to the momentum for the 0° scattered protons with the same magnitude of the momentum. $\mathbf{y}''$ is taken in the vertical direction. $\mathbf{x}''$ is defined to form a right handed coordinate system. $\mathbf{z}''$ is taken to be parallel to the momentum In the right panel, $\mathbf{L}''$ is taken along the momentum vector, and in general not in the horizontal plane. $\mathbf{S}''$ ($\mathbf{N}''$) is defined by a rotation of $\mathbf{x}''$ ($\mathbf{y}''$) with the rotation matrix which relates $\mathbf{z}''to\mathbf{L}$".

$$= \begin{pmatrix} \cos\phi & \sin\phi & 0 \\ -\sin\phi & \cos\phi & 0 \\ 0 & 0 & 1 \end{pmatrix} \begin{pmatrix} p_x \\ p_y \\ p_z \end{pmatrix} . \tag{C.9}$$

C.4 Polarization transfer coefficients

Under the parity invariance, the cross sections and the polarizations of proton inelastic scattering from a spin-zero target are written as [57]

$$I \begin{pmatrix} 1 \\ p'_{S'} \\ p'_{N'} \\ p'_{L'} \end{pmatrix} = I_0 \begin{pmatrix} 1 & 0 & A_N & 0 \\ 0 & D_{SS'} & 0 & D_{LS'} \\ P_N & 0 & D_{NN'} & 0 \\ 0 & D_{SL'} & 0 & D_{LL'} \end{pmatrix} \begin{pmatrix} 1 \\ p_S \\ p_N \\ p_L \end{pmatrix} , \tag{C.10}$$

where p_i is the polarization of the incoming protons and p'_i is the polarization of the outgoing protons. $D_{ij'}$'s denote Wolfenstein parameters [76, 57] for the i component of the incoming proton polarization and the j' component of the outgoing proton polarization. P_N (A_N) represents the N component of the induced polarization (analyzing power). I_0

(I) denotes the flux of incoming (outgoing) protons. Eq. C.10 is modified as

$$\begin{pmatrix} p'_{S'} \\ p'_{N'} \\ p'_{L'} \end{pmatrix} = \frac{1}{1 + A_N p_N} \left\{ \begin{pmatrix} D_{SS'} & 0 & D_{LS'} \\ 0 & D_{NN'} & 0 \\ D_{SL'} & 0 & D_{LL'} \end{pmatrix} \begin{pmatrix} p_S \\ p_N \\ p_L \end{pmatrix} + \begin{pmatrix} 0 \\ P_N \\ 0 \end{pmatrix} \right\}. \tag{C.11}$$

C.5 Polarization of the scattered protons in the experimental coordinate system

The components of the outgoing proton polarization in the coordinate system fixed at the experimental room are written as

$$\begin{aligned} \begin{pmatrix} p'_x \\ p'_y \\ p'_z \end{pmatrix} &= R_y(\theta) R_z(\phi) \begin{pmatrix} p'_{S'} \\ p'_{N'} \\ p'_{L'} \end{pmatrix} \\ &= \begin{pmatrix} \cos\theta & 0 & \sin\theta \\ 0 & 1 & 0 \\ -\sin\theta & 0 & \cos\theta \end{pmatrix} \begin{pmatrix} \cos\phi & -\sin\phi & 0 \\ \sin\phi & \cos\phi & 0 \\ 0 & 0 & 1 \end{pmatrix} \begin{pmatrix} p'_{S'} \\ p'_{N'} \\ p'_{L'} \end{pmatrix} \\ &\sim \begin{pmatrix} \cos\phi & -\sin\phi & \sin\theta \\ \sin\phi & \cos\phi & 0 \\ -\sin\theta\cos\phi & \sin\theta\sin\phi & 1 \end{pmatrix} \begin{pmatrix} p'_{S'} \\ p'_{N'} \\ p'_{L'}. \end{pmatrix} \end{aligned} \tag{C.12}$$

In the last equation, $\cos\theta$, is replaced be unity since θ is small.

C.6 Precession of the polarization vector in the spectrometer

By using Eq. B.1 the polarization of the 0° scattered protons measured by the FPP is expressed as

$$\begin{aligned} \begin{pmatrix} p''_{S''} \\ p''_{N''} \\ p''_{L''} \end{pmatrix} &= \begin{pmatrix} p''_{x''} \\ p''_{y''} \\ p''_{z''} \end{pmatrix} = R_y(\delta'_b) \begin{pmatrix} p'_x \\ p'_y \\ p'_z \end{pmatrix} \\ &= \begin{pmatrix} \cos\delta'_b & 0 & \sin\delta'_b \\ 0 & 1 & 0 \\ -\sin\delta'_b & 0 & \cos\delta'_b \end{pmatrix} \begin{pmatrix} p'_x \\ p'_y \\ p'_z \end{pmatrix} \quad (\text{for } \theta_s = \phi_s = 0), \end{aligned} \tag{C.13}$$

$$\delta'_b \equiv \gamma(\frac{g_p}{2} - 1)\delta_b, \tag{C.14}$$

where δ'_b is the spin precession angle and δ_b is the bending angle of the Grand Raiden. δ_b takes a value of 161.7° for the trajectory of the primary beam.

At finite scattering angles, the spin precession angle depends on the scattering angles, θ_s and ϕ_s. The followings described a rough estimate of the order of the correction for the measured polarization arising from the θ_s and ϕ_s dependence. By the horizontal scattering angle θ_s, scattered protons get an additional bending angle, δ_θ, along the y-axis in the spectrometer, where

$$\delta_\theta = -(\theta'_s - \theta_s) = \{1 - (\theta'_s|\theta_s)\}\theta_s. \tag{C.15}$$

$(\theta'_s|\theta_s)$ is defined in Eq. C.8. The matrix for the additional rotation of the polarization in the spectrometer is expressed by

$$\begin{aligned} & R_y(\delta'_\theta + \delta_\theta) \ , \\ & \delta'_\theta \equiv \gamma(\frac{g_p}{2} - 1)\delta_\theta \ . \end{aligned} \tag{C.16}$$

Since $R_y(\delta'_\theta)$ and $R_y(\delta'_b)$ commute with each other, Eq. C.13 is modified as

$$\begin{aligned} \begin{pmatrix} p''_{S''} \\ p''_{N''} \\ p''_{L''} \end{pmatrix} &= R_y(\theta'_s) \begin{pmatrix} p''_{x''} \\ p''_{y''} \\ p''_{z''} \end{pmatrix} \\ &= R_y(\theta'_s) R_y(\delta'_\theta + \delta_\theta) R_y(\delta'_b) \begin{pmatrix} p'_x \\ p'_y \\ p'_z \end{pmatrix} \\ &= \begin{pmatrix} \cos(\delta'_\theta + \theta_s) & 0 & \sin(\delta'_\theta + \theta_s) \\ 0 & 1 & 0 \\ -\sin(\delta'_\theta + \theta_s) & 0 & \cos(\delta'_\theta + \theta_s) \end{pmatrix} R_y(\delta'_b) \begin{pmatrix} p'_x \\ p'_y \\ p'_z \end{pmatrix} \\ & \qquad\qquad (\text{for } \phi_s = 0). \end{aligned} \tag{C.17}$$

The acceptance of the spectrometer is symmetric about θ_s. By taking the average of the polarization in the acceptance and neglecting the angular dependence of the differential cross sections, Eq.(C.17) is written by

$$\begin{aligned} \begin{pmatrix} \overline{p''_{S''}} \\ \overline{p''_{N''}} \\ \overline{p''_{L''}} \end{pmatrix} &= \begin{pmatrix} \overline{\cos(\delta'_\theta + \theta_s)} & 0 & 0 \\ 0 & 1 & 0 \\ 0 & 0 & \overline{\cos(\delta'_\theta + \theta_s)} \end{pmatrix} R_y(\delta'_b) \begin{pmatrix} p'_x \\ p'_y \\ p'_z \end{pmatrix} \\ & \qquad\qquad (\text{for } \phi_s = 0). \end{aligned} \tag{C.18}$$

$$\begin{aligned}\overline{\cos(\delta'_\theta + \theta_s)} &= \frac{1}{2\theta_s^{max}} \int_{-\theta_s^{max}}^{\theta_s^{max}} \cos(\delta'_\theta + \theta_s) d\theta_s \\ &= \frac{\sin\{[\gamma(\frac{g_p}{2} - 1)(1 - (\theta'_s|\theta_s)) + 1]\theta_s^{max}\}}{[\gamma(\frac{g_p}{2} - 1)(1 - (\theta'_s|\theta_s)) + 1]\theta_s^{max}} \\ &\sim 0.996 \quad (\text{for } \theta_s^{\max} = 1.00^\circ). \end{aligned} \tag{C.19}$$

Hence the averaging in the horizontal acceptance, θ_s, has an effect of reducing the x'' and z'' components of the polarization measured by the focal plane polarimeter. The factor is of the order of 0.996 and therefore negligible.

Although the same technique does not apply to the ϕ_s acceptance since the rotation matrix does not commute with $R_y(\theta'_b)$, the order of the correction is roughly estimated in a same way

$$\begin{aligned}\overline{\cos(\delta'_\phi + \phi_s)} &= \frac{1}{2\phi_s^{max}} \int_{-\phi_s^{max}}^{\phi_s^{max}} \cos(\delta'_\phi + \phi_s) d\phi_s \\ &= \frac{\sin\{[\gamma(\frac{g_p}{2} - 1)(1 - (\phi'_s|\phi_s)) + 1]\phi_s^{max}\}}{[\gamma(\frac{g_p}{2} - 1)(1 - (\phi'_s|\phi_s)) + 1]\phi_s^{max}} \\ &\sim 0.996 \quad (\text{for } \phi_s^{\max} = 2.98^\circ). \end{aligned} \tag{C.20}$$

From both the contributions of Eq. C.19 and C.20, we obtain

$$\begin{pmatrix} \overline{p''_{S''}} \\ \overline{p''_{N''}} \\ \overline{p''_{L''}} \end{pmatrix} \sim \begin{pmatrix} 0.99 & 0 & 0 \\ 0 & 1 & 0 \\ 0 & 0 & 0.99 \end{pmatrix} R_y(\delta'_b) \begin{pmatrix} p'_x \\ p'_y \\ p'_z \end{pmatrix} \quad (\text{for } \theta_s^{\max} = 1.00^\circ \text{ and } \phi_s^{\max} = 2.98^\circ) \, . \tag{C.21}$$

The above estimate is consistent with a more realistic calculation ($\overline{M'}$ in Eq. B.8) of the spin rotation angle in the spectrometer, which is described in Appendix B.2.

C.7 Summary of the finite angle correction

From Eq.(C.12), (C.11), and (C.9) we obtain

$$\begin{pmatrix} p'_x \\ p'_y \\ p'_z \end{pmatrix} = \frac{1}{1 + A_N p_N} \begin{pmatrix} \cos\phi & -\sin\phi & \sin\theta \\ \sin\phi & \cos\phi & 0 \\ -\sin\theta\cos\phi & \sin\theta\sin\phi & 1 \end{pmatrix}$$

$$\times \left\{ \begin{pmatrix} D_{SS'} & 0 & D_{LS'} \\ 0 & D_{NN'} & 0 \\ D_{SL'} & 0 & D_{LL'} \end{pmatrix} \begin{pmatrix} \cos\phi & \sin\phi & 0 \\ -\sin\phi & \cos\phi & 0 \\ 0 & 0 & 1 \end{pmatrix} \begin{pmatrix} p_x \\ p_y \\ p_z \end{pmatrix} + \begin{pmatrix} 0 \\ P_N \\ 0 \end{pmatrix} \right\}. \tag{C.22}$$

Since the acceptance of the spectrometer is taken to be symmetric about the $\phi = 0$ (horizontal) plane and the $\phi = \pi/2$ (vertical) plane, it is valid to omit odd-functions of ϕ and to omit the terms which are odd in the substitution of ϕ by $\phi + \pi$. In addition, $(1 + A_N p_N)^{-1}$ is approximated as $1 - A_N p_N$. Then the Eq.(C.22) is modified as

$$\begin{aligned} &\begin{pmatrix} p'_x \\ p'_y \\ p'_z \end{pmatrix} \\ &= \begin{pmatrix} D_{SS'}\cos^2\phi + D_{NN'}\sin^2\phi & 0 & D_{LL'}\sin\theta \\ 0 & D_{SS'}\sin^2\phi + D_{NN'}\cos^2\phi & 0 \\ -(D_{SS'}\cos^2\phi + D_{NN'}\sin^2\phi)\sin\theta & 0 & D_{LL'} \end{pmatrix} \begin{pmatrix} p_x \\ p_y \\ p_z \end{pmatrix} \\ &- A_N p_y \cos\phi \left\{ \begin{pmatrix} D_{SL'}\sin\theta\cos\phi & 0 & D_{LS'}\cos\phi \\ 0 & 0 & 0 \\ D_{SL'}\cos\phi & 0 & -D_{LS'}\sin\theta\cos\theta \end{pmatrix} \begin{pmatrix} p_x \\ p_y \\ p_z \end{pmatrix} + P_N \begin{pmatrix} 0 \\ \cos\phi \\ 0 \end{pmatrix} \right\} \\ &+ A_N p_x \sin\phi \left\{ \begin{pmatrix} 0 & D_{SL'}\sin\theta\sin\phi & 0 \\ 0 & 0 & D_{LS'}\sin\theta \\ 0 & D_{SL'}\sin\theta & 0 \end{pmatrix} \begin{pmatrix} p_x \\ p_y \\ p_z \end{pmatrix} + P_N \begin{pmatrix} -\sin\phi \\ 0 \\ \sin\theta\sin\phi \end{pmatrix} \right\} \end{aligned} \tag{C.23}$$

At small scattering angles, $D_{SL'}$, $D_{LS'}$, A_N, and P_N are of the order of θ. By omitting second and higher order terms of θ, we obtain

$$\begin{aligned} &\begin{pmatrix} p'_x \\ p'_y \\ p'_z \end{pmatrix} \\ &= \begin{pmatrix} D_{SS'}\cos^2\phi + D_{NN'}\sin^2\phi & 0 & D_{LL'}\sin\theta \\ 0 & D_{SS'}\sin^2\phi + D_{NN'}\cos^2\phi & 0 \\ -(D_{SS'}\cos^2\phi + D_{NN'}\sin^2\phi)\sin\theta & 0 & D_{LL'} \end{pmatrix} \begin{pmatrix} p_x \\ p_y \\ p_z \end{pmatrix} \end{aligned} \tag{C.24}$$

Eq.(C.24) becomes a simple diagonal equation at 0° by bringing θ to zero and applying the relation, $D_{SS'}$=$D_{NN'}$, which holds at 0°.

From Eq. C.21 and C.24, the the polarization measured by the FPP ($\overline{p''_{S''}}$), which is the average of $p''_{S''}$ in the acceptance, is written as

$$\overline{p''_{S''}} = D^{\rm cor}_{SS} p_x \cos\delta'_b + D^{\rm cor}_{LL} p_z \sin\delta'_b \ . \tag{C.25}$$

where $D_{SS}^{\rm cor}$ and $D_{LL}^{\rm cor}$ are defined as

$$\begin{aligned} D_{SS}^{\rm cor} &\equiv 0.99 \frac{\int d\Omega \frac{d\sigma}{d\Omega}(\theta)(D_{SS'}\cos^2\phi + D_{NN'}\sin^2\phi)}{\int d\Omega \frac{d\sigma}{d\Omega}(\theta)} . \\ D_{LL}^{\rm cor} &\equiv 0.99 \frac{\int d\Omega \frac{d\sigma}{d\Omega}(\theta) D_{LL'}}{\int d\Omega \frac{d\sigma}{d\Omega}(\theta)} . \end{aligned} \tag{C.26}$$

The suffix 'cor' represents an averaged observable which can be compared with the experimental results. $D_{SS}^{\rm exp}$ or $D_{LL}^{\rm exp}$ presented in Chap. 4. The integrations should be taken in the range, $|\sin\theta\cos\phi| = \theta_s^{\rm max} \leq 1.00°$ and $|\sin\theta\sin\phi| = \phi_s^{\rm max} \leq 2.98°$ for the comparison with the experimental results. The averaged total spin transfers are obtained from $D_{SS}^{\rm corr}$ and $D_{LL}^{\rm corr}$ by

$$\Sigma^{\rm cor} \equiv \frac{3 - (2D_{SS}^{\rm cor} + D_{LL}^{cor})}{4} . \tag{C.27}$$

Appendix D

DATA ACQUISITION SYSTEM

D.1 Introduction

A focal plane polarimeter (FPP) for the *Grand Raiden* spectrometer has been constructed at the Research Center for Nuclear Physics (RCNP), Osaka University. The FPP enables the measurement of the polarization of scattered protons by using the double scattering technique. In experiments using the FPP, the typical data size of an event becomes larger and the number of events required to deduce a physical result becomes larger compared with ordinary experiments of measuring differential cross sections. In addition, a measurement of polarization transfer observables in 0° proton inelastic scattering has been proposed. Since the experiment suffers lots of background events arising from the beam halo, a large number of events must be taken to get physical results. Hence, high requirements have arisen for a high speed data acquisition system which is capable of handling 5 kHz triggers with live time larger than 80%. The typical data size is 160 bytes/events. An overview of the new data acquisition system is illustrated in Fig. D.1.

D.2 Front part

A new data acquisition system has been developed according to the following design.

- Use TDC/ADC modules which provide fast data conversion and readout.

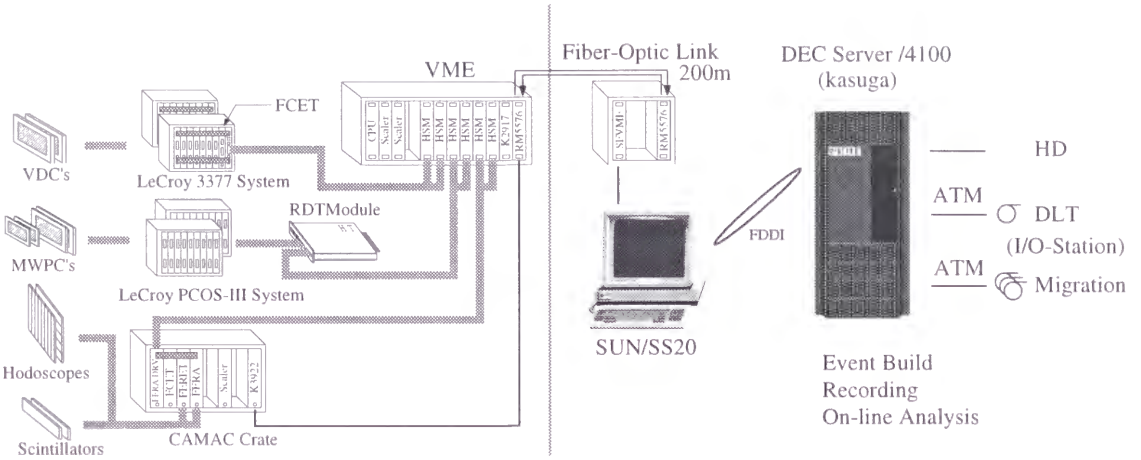

Figure D.1: Overview of the data acquisition system.

- Store events in buffer memories by hardware logic
- Parallel data storing for each counter system
- Apply a double buffer method for each counter system to remove the dead time of data transfer

For the first point, we have replaced all the ADCs and TDCs by LeCroy FERA/FERET fast encoding and readout ADC/TDC system. The conversion time of the LeCroy FERA/FERET modules is 8.5 μsec for 11 bit resolution, which is much faster than that of the previously modules, *e.g.* 60 μ for LeCroy 2249A. We have also replaced LeCroy 4291B drift chamber TDCs by LeCroy 3377 drift chamber TDCs. The conversion time was improved from 35 μsec + 12 μsec per hit channel to 1.8 μsec + 0.1 μsec per hit channel.

For the second and third points, CES 8170 High Speed Memories and LeCroy 1190 Dual Port Memories has been installed on the front-end VME system. The data of the digitizer modules are transfered to the memory modules via ECL bus with no CAMAC functions nor software overhead. Two new modules have been developed for the management of the data transfer: Rapid Data Transfer Module (RDTM) and Flow Controlling Event Tagger (FCET) The RDTM manages the data transfer from a LeCroy 2738 PCOS III system

via LeCroy-bus to a memory modules via ECL-bus. The RDTM appends a header word and an event counter word in front of an event. The header word and the counter word are used in the stage of the event building. The maximum data transfer rate through the RDTM is 4 MBytes/sec. The FCET is a logic module programmed on a FPGA (field programmable gate array) on LeCroy 2366 universal logic module (ULM). The FCET is installed in a FERA bus placed between a LeCroy 4301 FERA driver module and FERA modules. The FCET controls the data flow in the FERA bus according to the decision by the second level trigger system, and appends a header word, an event counter word, and an input register word to each event. The input register word is read out from its the front panel of the FCET. The FCET is also operated with LeCroy 3377 drift chamber TDC's.

For the last point, we assigned a pair of buffer memory modules for each counter systems. One of the pair modules are alternatively set active. When one of the active module comes close to full after the acquisition of an event, all the active buffers are switched to inactive and the paired buffers are set active. Thus, the buffer switching takes place for all the pair modules at once. The buffer switching mechanism is also managed by hardware logics programmed on a ULM. The dead time of the buffer switching is about 30 micro seconds and therefore negligible. About 300 events can be stored in a buffer.

The time spec of the front readout system is plotted in Fig. D.2. The typical dead time for the acquisition of an event is 20 to 30 micro seconds, which depends on the data size.

D.3 Rear part

The data stored in the buffer memory modules on the front-end VME system, which is operated by the OS/9 operating system on an MC68040 based CPU board, are transferred to a SUN sparc 10 work station using VMIC 5576 reflective memory modules via fiber-optic cables. They reflective memory modules are connected to a fiber-optic cable ring.

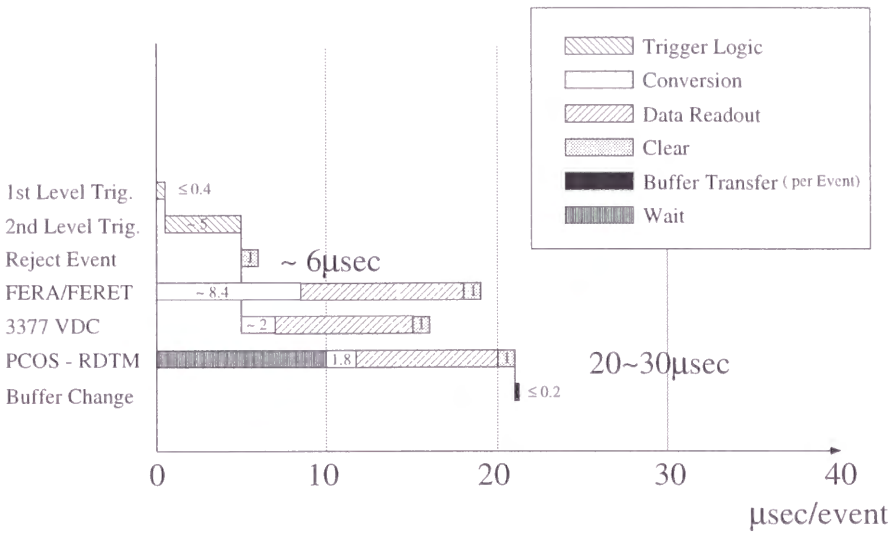

Figure D.2: Time table of an event action.

The memory on the modules can be understood as a shared memory which can be accessed from any node connected to the ring. When data are written in one of the reflective memory modules, it broadcasts the data through to all the other modules resulting in the appearance of the same at the same memory location of the other modules. A data transfer as high as 2 MBytes/sec has been achieved. In the first version of the system, the data transfered to the SUN work station (mari) are stored at the local hard disks. In the present system, the data are re-transfered to a DEC/4100 work station (kasuga) operated by the Digital Unix version 4.0 system via an FDDI network. The data are stored in the hard disks connected to the kasuga work station. The kasuga work station does event building and distributes the built data to analyzers on any hosts using TCP/IP socket communications.

D.4 Performance

The newly developed data acquisition system has been used in many experiments at RCNP since July 1996. In the experiment to measure polarization transfer observables at θ=0 degrees on January 1997. the typical trigger rate from the second level trigger

system was 4 to 6 kHz and the dead time was 10 to 20 %. It corresponds to the data transfer rate of 500 to 1,000 KBytes/sec.

The development of the new data acquisition system was reported in Ref. [48, 49]. The author is grateful to R. Fox for valuable discussions.

Bibliography

[1] G. Waters, I.M. Blair, G.A. Ludgate, N.M. Stewart, C. Amsler, R.C. Brown, D.V. Bugg, J.A. Edgington, C.J. Oram, K. Shakarchi, A.S. Clough, D. Axen, S. Jaccard, and J. Vavra, Nucl. Instrum. and Methods **153**, 401 (1978).

[2] R.D. Ransome, S.J. Green, C.L. Hollas, B.E. Bonner, M. McNaughton, C. Morris, and H. thiessen, Nucl. Instrum. and Methods **201**, 309 (1982).

[3] M. Ieiri, H. Sakaguchi, M. Nakamura, H. Sakamoto, H. Ogawa, M. Yosoi, T. Ichihara, N. Isshiki, Y, Takeuchi, H. Togawa, T. Tsutsumi, S. Hirata, T. Nakano, and S. Kobayashi, Nucl. Instrum. and Methods A **257**, 253 (1987).

[4] H. Ikegami, T. Noro, T. Takayama, M. Nakamura, and S. Kobayashi, RCNP Annual Report 1981; T. Noro *et al.*, J. Phys. Soc. Japan **55** (1986) Suppl. pp. 470.

[5] A. Tamii, H. Akimune, I. Daito, M. Fujiwara, K. Hatanaka, K. Hosono, T. Inomata, M. Nakamura, T. Noro, H. Sakaguchi, S. Toyama, M. Yamagoshi, M. Yoshimura, and M. Yosoi, *AIP Conf. Proc. 339, 8th Int. Symp. on Polarization Phenomena in Nuclear Physics*, ed. E.J. Stephenson and S.E. Vigdor, (AIP, New York, 1995) pp. 395.

[6] W.G. Love, Amir Klein, M.A. Franey, and K. Nakayama, Can. J. Phys. **65**, 536 (1987).

[7] B.C. Clark, R.L. Mercer, and P. Schwandt, Phys. Lett. **B122**, 211 (1983).

[8] J.R. Shepard. J.A. McNeil, and S.J. Wallace. Phys. Rev. Lett. **50**, 1443 (1983).

[9] A. Rahbar, B. Aas, E. Bleszynski, M. Bleszynski. M. Haji-Saeid, G.J. Igo, F. Irom, G. Pauletta, A.T.M. Wang, J.B. McClelland, J.F. Amann, T.A. Caray, W.D. Cornelius, M. Barlett, G.W. Hoffmann, C. Glashausser, S. Nanda, and M.M. Gazzaly, Phys. Rev. Lett. **47**, 1811 (1981).

[10] F.A. Brieva, and J.R. Rook, Nucl. Phys. **A297**, 206 (1978).

[11] T.N. Taddeucci, C.A. Goulding, T.A. Carey, R.C. Byrd, C.D. Goodman, C. Gaarde, J. Larsen, D. Horen, J. Rapaport, and E. Sugarbaker, Nucl. Phys. **A469**, 125 (1987).

[12] C.D. Goodman, C.A. Goulding, M.B. Greenfield, J. Rapaport, D.E. Bainum, C.C. Foster, W.G. Love, and F. Petrovich, Phys. Rev. Lett. **44**, 1755 (1980).

[13] T.N. Taddeucci, J. Rapaport, D.E. Bainum, C.D. Goodman, C.C. Foster, C. Gaarde, J. Larsen, C.A. Goulding, D.J. Horen, T. Masterson, and E. Sugarbaker, Phys. Rev. C. **25**, 1094 (1982).

[14] W.G. Love, K. Nakayama, and M.A. Franey, Phys. Rev. Lett. **28**, 1401 (1987).

[15] C.J. Horowitz, Phys. Lett. **B196**, 285 (1987).

[16] T.N. Taddeucci, T.A. Carey, C. Gaarde, J. Larsen, D.J. Horen, T. Masterson, J. Rapaport, T.P. Welch, and E. Sugarbaker, Phys. Rev. Lett. **52**, 1960 (1984).

[17] T. Wakasa, H. Sakai, H. Okamura, H. Otsu, S. Ishida, N. Sakamoto, T. Uesaka, Y. Satou, M.B. Greenfield, N. Koori, A. Okihana, and K. Hatanaka, Phys. Rev. C **51**, R2871 (1995).

[18] N. Anantaraman, B.A. Brown, G. M. Crawley, A. Galonsky, C. Djalali, N. Marty, M. Morlet, A. Willis, J.-C. Jourdain, and B. H.Wildenthal, Phys. Rev. Lett. **52**, 1409 (1984).

[19] G.M. Crawley, C. Djalali, M. Marty, M. Morlet, A. Willis, N. Anantaraman, B.A. Brown, and A. Galonsky, Phys. Rev. C **39**, 311 (1989).

[20] A. Willis, M. Morlet, N. Marty, C. Djalali, J. Guillot, H. Langevin-Joliot, J. Van de Wiele, A. Mack, B. Bonin, R. Fergerson, E. Tomasi-Gustafsson, J.C. Lugol, J.C.Duchazeaubeneix, and H. Sakaguchi, Phys. Rev. C **43**, 2177 (1991).

[21] Y. Sakemi, H. Sakaguchi, M. Yosoi, H. Akimune, T. Takahashi, A. Yamagoshi, A. Tamii, M. Fujiwara, K. Hatanaka, K. Hosono, T. Noro, H. Togawa, I. Daito, Y. Fujita, and T. Inomata, Phys. Rev. C **51**, 3162 (1995).

[22] D.J. Mercer, G.M. Crawley, S. Danczyk, A. Galonsky, J. Wang, A. Bacher, G.P.A. Berg, A.C. Betker, W. Schmidtt, and E.J. Stephenson, IUCF Annual Report 1994, pp. 20.

[23] Y. Fujita, private communication.

[24] S.J. Seestrom-Moriss, J.M. Moss, J.B. McClelland, W.D. Cornelius, T.A. Carey, N.M. Hintz, M. Gazzaly, M.A. Franey, S. Nanda, and B. Aas, Phys. Rev. C **26**, 2131 (1982).

[25] A.K. Kerman, H. McManus and R.M. Thaler, Ann. of Phys. **8**, 551 (1959).

[26] J.M. Moss, Phys. Rev. C **26**, 727 (1982);

[27] J.M. Moss, *Proc. Int. Symp. on Spin Excitations in Nuclei*, ed. F. Petrovich *et al.* (Plenum, New York, 1983) pp. 355.

[28] W.G. Love and M.A. Franey, Phys. Rev. C **24**, 1073 (1981).

[29] J.R. Comfort, G.L. Moake, C.C. Foster, P. Schwant, and W.G. Love, Phys. Rev. C **26**, 1800 (1982), and references therein.

[30] For example, see T. Wakasa, H. Sakai, K. Hatanaka, H. Okamura, H. Otsu, S. Fujita, T. Nonaka, T. Uesaka, Y. Satou, T. Ohnishi, G. Yokoyama, S. Ishida, N. Sakamoto, M.B. Greenfield, M. Ichimura, and K. Kawahigashi, Phys. Rev. C **59**, 3177 (1999).

[31] H. Ueno, Y. Fujita, H. Fujita, T. Shinada, Y. Kanzaki, M. Yosoi, A. Tamii, K. Takahisa, F. Ihara, H. Kohri, T. Yamagata, and K. Katori, submitted to Phys. Lett. B.

[32] For example, see A. Akimune, I. Daito, Y. Fujita, M. Fujiwara, M.B. Greenfield, M.N. Harakeh, T. Inomata, J. Jänecke, K. Katori, S. Nakayama, H. Sakai, Y. Sakemi, M. Tanaka, and M. Yosoi, Phys. Rev. C **52**, 604 (1995).

[33] For example, see H. Okamura, S. Fujita, Y. Hara, K. Hatanaka, T. Ichihara, S. Ishida, K. Katoh, T. Niizeki, H. Ohnuma, H. Otsu, H. Sakai, N. Sakamoto, Y. Satou, T. Uesaka, T. Wakasa, and T. Yamashita, Phys. Lett. B **345**, 1 (1995).

[34] I. Daito, H. Akimune, Sam M. Austin, D. Bazin, G.P.A. Berg, J.A. Brown, B.S. Davids, Y. Fujita, H. Fujimura, M. Fujiwara, R. Hazama, T. Inomata, K. Ishibashi, J. Jänecke, S. Nakayama, K. Pham, D.A. Roberts, B.M. Sherrill, M. Steiner, A. Tamii, M. Tanaka, H. Toyokawa, and M. Yosoi, Phys. Lett. B **418**, 27 (1998).

[35] S. Nakayama, H. Akimune, I. Daito, H. Fujimura, Y. Fujita, M. Fujiwara, K. Fushimi, T. Inomata, K. Ishibashi, H. Kohri, N. Koori, K. Takahisa, A. Tamii, M. Tanaka, H. Toyokawa, and T. Yamagata, Nucl. Instrum. Methods A **402**, 367 (1998), and references therein.

[36] S. Cohen, D. Kurath, Nucl. Phys. **73** 1, (1965).

[37] K.W. Jones, C. Glashausser, R. de Swiniarski, S. Nanda, T.A. Carey, W.Cornelius, J.M. Moss, J.B. McClelland, J.R. Comfort, J.-L. Escudie, M. Gazzaly, N. Hints, G. Igo, M. Haji-Saeid, and C.A. Whitten, Jr., Phys. Rev. C **33**, 17 (1986).

[38] H. Sakai, in proceedings of *International Symposium on New Facet of Spin Giant Resonances in Nuclei*, (World Scientific, Singapore 1998) pp. 29.

[39] T. Suzuki, Nucl. Phys. **A577**, 167c (1994).

[40] M.A. Franey, W.G. Love, Phys. Rev. C **31**, 488 (1985).

[41] W.G. Love, Amir Klein, M.A. Franey, and K. Nakayama, Can. J. Phys. **65**.536 (1987).

[42] M. Fujiwara, H. Akimune, I. Daito, H. Fujimura, Y. Fujita, K. Hatanaka, H. Ikegami, I. Katayama, K. Nagayama, N. Matsuoka, S. Morinobu, T. Noro, M. Yoshimura, H. Sakaguchi, Y. Sakemi, A. Tamii, M. Yosoi, Nucl. Instrum. Meth. A **422**, 484 (1999).

[43] M. Yosoi, H. Akimune, I. Daito, M. Fujiwara, S. Hirata, T. Inomata, O. Kamigaito, M. Kawabata, T. Noro, Y. Sakemi, T. Takahashi, A. Tamii, S. Toyama, A. Yamagoshi, M. Yoshimura, and H. Sakaguchi, *AIP Conf. Proc. 343, 11th Int. Symp. on High Energy Spin Physics*, ed. K.J. Heller and S.L. Smith (AIP, New York, 1995) pp. 157.

[44] K. Hatanaka, K. Takahisa, H. Tamura, M. Sato and I. Miura, Nucl. Instrum. and Methods **A384**, 575 (1997).

[45] T. Noro, M. Fujiwara, O. Kamigaito, S. Hirata, Y. Fujita, A. Yamagoshi, T. Takahashi, H. Akimune, Y. Sakemi, M. Yosoi, H. Sakaguchi, and J. Tanaka, RCNP Annual Report 1991.

[46] H. Yoshida, T. Baba, T. Noro, M. Kawabata, H. Akimune, H. Sakaguchi, A. Tamii, H. Takeda, and T. Kawabata, RCNP Annual Report 1996.

[47] M. Yosoi, H. Akimune, I. Daito, T. Inomata, T. Ishikawa, M. Itoh, T. Kawabata, M. Nakamura, T. Noro, E. Obayashi, H. Sakaguchi, A. Tamii, H. Takeda, T. Taki, H. Yoshida, and M. Yoshimura, RCNP Annual Report 1997.

[48] A. Tamii, H. Sakaguchi, H. Takeda, M. Yosoi, H. Akimune, M. Fujiwara, H. Ogata, M. Tanaka, and H. Togawa, IEEE Trans. on Nucl. Sci. **43**, 2488 (1996).

[49] A. Tamii, M. Itoh, T. Kawabata, H. Sakaguchi, H. Takeda, T. Taki, H. Torii, M. Yosoi, H. Akimune, T. Baba, M. Fujiwara, Y. Kawabata, T. Noro, and H. Yoshida, *Proc. 2nd Int. Data Acquisition Workshop on Networked Data Acquisition System*, ed. M. Nomachi and S. Ajimura (World Scientific, Singapore, 1997) pp. 238.

[50] T. Kawabata, H. Sakaguchi, A. Tamii, H. Takeda, T. Taki, and H. Yoshida, RCNP Annual Report 1996.

[51] H. Takeda, H. Sakaguchi, A. Tamii, H. Akimune, M. Kawabata, and M. Tanaka, *Proc. 1995 IEEE Conf. on Real-Time Computer Applications in Nuclear Particle and Plasma Physics*, pp. 210; H. Takeda, H. Sakaguchi, A. Tamii, M. Tanaka, and H. Akimune, RCNP Annual Report 1995.

[52] A. Tamii, program code DRED, unpublished.

[53] Program Library HBOOK, CERN Program Library entry Y250.

[54] Program Code PAW, CERN Program Library entry Q121.

[55] S. Kato, K. Okada, M. Kondo, A. Shimizu, K. Hosono, T. Saito, N. Matsuoka, S. Nagamachi, K. Nisimura, N. Tamura, K. Imai, K. Egawa, M. Nakamura, T. Noro, H. Shimizu, K. Ogino, and Y. Kadota Nucl. Instrum. and Methods A **169**, 589 (1980).

[56] For example, see W.R. Leo, *Techniques for Nuclear and Particle Physics Experiments*, (Springer-Verlag, Berlin, 1987).

[57] G.G. Ohlsen, Rep. Prog. Phys. **35**, 717 (1972).

[58] M.W. McNaughton, B.E. Bonner, H. Ohnuma, O.B. van dijk, Sun Tsu-Hsun, C.L. Hollas, D.J. Cremans, K.H.McNaughton, P.J. Rikey, R.F. Rodebaugh, Shen-Wu Xu, S.E. Turpin, B. Aas, and G.S.Weston, Nucl. Instrum. Methods A **241**, 435 (1985).

[59] *Stopping Powers for Electrons and Positrons*, ICRU Report No.37 (1987); A web site is available from http://physics.nist.gov/PhysRefData/XrayMassCoef/tab1.html.

[60] E. Uegaki, Y. Abe, S. Okabe, and H. Tanaka, Prog. Theor. Phys. **59**, 1031 (1978);

[61] M. Kamimura, Nucl. Phys. **A351**, 456 (1981).

[62] P. Descouvemont and D. Baye, Phys. Rev. C **36**, 54 (1987).

[63] F. Ajzenberg-Selove, Nucl. Phys. **A506**, 1 (1990).

[64] *Table of Isotopes Eighth Edition 1998 Update*, edited by Rechard B. Firestone, (Wiley, New York, 1998).

[65] J. Raynal, program code DWBA91, Service de Physique Theorique, CEA-Saclay (1991), unpublished.

[66] K.W. Jones, C. Glashausser, R. de Swiniarski, F.T. Baker, T.A. Carey, J.R. Comfort, W. Cornelius, J.L. Escudié, M. Gazzaly, A. Green, M. Haji-Saeid, N. Hintz, G. Igo, J.B. McClelland, J.M. Moss, S. Nanda, and C.A. Whitten, Phys. Rev. C **50**, 1982 (1994).

[67] H.V. von Geramb, in *The Interaction between Medium Energy Nucleons with Nuclei*, AIP Conf. Proc. No. 97, ed. H.O. Meyer (AIP, New York, 1982), p. 44.

[68] M. Lacombe, B. Loiseau, J.M. Richard, R. vinh Mau, J. Côté, P. Pirès, and R. de Tourreil, Phys. Rev. C **21**, 861 (1980).

[69] K.W. Jones, C. Glashausser, S. Nanda, R. de Swiniarski, T.A. Carey, W. Cornelius, J.M. Moss, J.B. McClelland, S.J. Seestrom-Morris, J.R. Comfort, J.-L. Escudié, M. Gazzaly, N. Hintz, G. Igo, M. Haji-Saeid, and C.A. Whitten, Phys. Lett. B **128**, 281 (1983).

[70] B.D. Anderson, L.A.C. Garcia, D.J. Millener, D.M. Manley, A.R. Baldwin, A. Fazely, R. Madey, N. Tamimi, J.W. Watson, and C.C. Foster, Phys. Rev. C **54**, 237 (1996).

[71] T. Inomata, H. Akimune, I. daito, H. Ejiri, H. Fujimura, Y. Fujita, M. Fujiwara, M.N. Harakeh, K. Ishibashi, H. Kohri, N. Matsuoka, S. Nakayama, A. Tamii, N. Tanaka, H. Toyokawa, M. Yoshimura, and M. Yosoi, Phys. Rev. C **57**, 3153 (1998).

[72] B.N. Johnson, M. Morlet, C. Djalali, F.T. Baker, L. Bimbot, C. Glashausser, J. Guillot, H. Langevin-Joliot, N. Marty, L. Rosier, E. Tomasi-Gustafsson, J. Van de Wiele, and A. Willis, Phys. Rev. C **51**. 1726 (1995).

[73] J.D. Jackson. *Classical Electrodynamics* (WILEY, New York, 1975).

[74] Program code RAYTRACE. S. Kowalski and H.A. Enge. Nucl. Instrum. and Methods A **258**, 407 (1987).

[75] M. Fujiwara. *Proc. of the 5th French-Japanese Symposium*, pp. 348.

[76] L. Wolfenstein. Ann. Rev. Nucl. Sci. **6**, 43 (1956).